Sidestepping mechanism of yeast kinesin-8, Kip3

DISSERTATION

submitted for the degree of

Doctor rerum naturalium
(Dr. rer. nat.)

Fakultät für Mathematik und Naturwissenschaften
Technische Universität Dresden

by

Aniruddha Mitra
born on September 25^{th}, 1987 in Kolkata, India

submitted on October 13^{th}, 2017

List of reviewers:

Prof. Dr. Stefan Diez

B CUBE - Center for Molecular Bioengineering, Technische Universität Dresden, Arnoldstraße 18, 01307 Dresden

Prof. Dr. Michael Schlierf

B CUBE - Center for Molecular Bioengineering, Technische Universität Dresden, Arnoldstraße 18, 01307 Dresden

Thesis Defense: December 18^{th}, 2017

CBG
Max Planck Institute
of Molecular Cell Biology
and Genetics

TECHNISCHE
UNIVERSITÄT
DRESDEN

The work described in this thesis was performed at the B CUBE - Center for Molecular Bioengineering, Technische Universität Dresden, Arnoldstraße 18, and the Max Planck Institute of Molecular Cell Biology and Genetics, Pfotenhauerstraße 108, both in 01307 Dresden, Germany

Erklärung entsprechend §5.5 der Promotionsordnung

Hiermit versichere ich, dass ich die vorliegende Arbeit ohne unzulässige Hilfe Dritter und ohne Benutzung anderer als der angegebenen Hilfsmittel angefertigt habe; die aus fremden Quellen direkt oder indirekt übernommenen Gedanken sind als solche kenntlich gemacht. Die Arbeit wurde bisher weder im Inland noch im Ausland in gleicher oder ähnlicher Form einer anderen Prüfungsbehörde vorgelegt.

Die Dissertation wurde im Zeitraum vom 15th January 2012 bis 13th October 2017 verfasst und von Prof. Dr. Stefan Diez am B CUBE - Center for Molecular Bioengineering der Technische Universität Dresden betreut.

Meine Person betreffend erkläre ich hiermit, dass keine früheren erfolglosen Promotionsverfahren stattgefunden haben.

Ich erkenne die Promotionsordnung der Fakultät für Mathematik und Naturwissen- schaften, Technische Universität Dresden an.

.....

Aniruddha Mitra

Dresden, 13^{th} October, 2017

Abstract

Kinesin-8 motors regulate the lengths of microtubules in cells. In previous studies, these motors have been shown to utilize their highly processive plus-end directed motility to reach microtubule plus-ends where they act as a microtubule depolymerase. The superprocessive motility importantly allows Kip3 motors to depolymerize microtubules in a length-dependent manner, the underlying mechanism of which has been described by an antenna model. During such long runs, motors *in vivo* are expected to frequently encounter roadblocks, such as microtubule-associated proteins. The adaptions in the stepping mechanism that allow kinesin-8 motors to navigate around roadblocks to reach microtubule ends is not well understood. In this work, *in vitro* techniques were utilized to understand the navigation strategy of yeast kinesin-8, Kip3.

Three-dimensional stepping motility of Kip3 on the surface of microtubules can be inferred (i) indirectly from rotational motion of microtubules gliding along a surface coated with Kip3 and (ii) directly by three dimensional tracking of Kip3 on freely suspended microtubules. Firstly, an impact-free method to detect rotations of gliding microtubules was established based on fluorescent speckles within the microtubule structure in combination with fluorescent interference contrast microscopy. Secondly, a suspended microtubule assay was established to obtain three dimensional trajectories of single Kip3 motors, using Parallax, a dual-focus imaging technique.

The motility assays performed in this work revealed that Kip3 motors undergo left-handed helical motion around the microtubule lattice. This indicates that Kip3 employs a directed sidestepping strategy which is attributed to the motor having a flexible neck and/or a long neck linker. Interestingly, further analysis of the rotational motion revealed that the sidestepping of Kip3 is not directly coupled to the forward stepping. Based on these observations, it is hypothesized that the motor can transition from a two-head-bound conformation to a one-head-bound conformation while waiting for ATP. Whereas the motor can step forward from both states, sidestepping is strongly favored from the one-head-bound conformation. This hypothesis was confirmed through experiments as well as numerical simulations where the transition from the two-head-bound conformation to the one-head-bound conformation was enhanced by either prolonging the ATP waiting time or increasing

the transition rate (by reducing the motor-microtubule interaction).

Finally, Kip3 based motility assays were performed using microtubules decorated with rigor binding kinesin-1 motors acting as roadblocks. While gliding assays using roadblock-decorated microtubules indicated a left-biased sidestepping strategy for Kip3, stepping assays revealed an additional diffusive component in the stepping motility of Kip3, along with the leftward bias. Taken together, it is hypothesized that Kip3 has a dual-mode roadblock circumnavigation strategy. Upon encountering a roadblock, the motor circumnavigates it (i) by shifting to the adjacent left microtubule protofilament using the biased sidestepping mechanism or (ii) by shifting microtubule protofilaments in an unbiased diffusive manner upon switching out of the step cycle. Therefore, the biophysical properties of Kip3 are fine-tuned to ensure that the motor reaches the microtubule plus-end to perform its depolymerase activity.

"Would you tell me, please, which way I ought to go from here?"
"That depends a good deal on where you want to get to," said the cat.
"I don't much care where -" said Alice.
"Then it doesn't matter which way you go," said the cat.
"- so long as I get SOMEWHERE," Alice added as an explanation.
"Oh, you're sure to do that," said the cat, "if you only walk long enough."

– Lewis Caroll's Alice's Adventures in Wonderland

Table of Contents

List of Figures

List of Tables

Table **Page**

CHAPTER 1

Introduction

Eukaryotic cells are like bustling cities with construction, remodeling and active intracellular transport of the densely-packed elements constituting it. While Brownian diffusion is sufficient for short range transport (micrometer), active motility is essential for performing long range directed transport of proteins, genetic material, lipids and other molecules, for communication between cell compartments (organelles) and with extracellular environments. Further, active motility is necessary to build, maintain and enable functioning of vital cellular apparatus such as the mitotic and meiotic spindle, cilia and flagella. To carry out the motility processes, the cells are equipped with dynamic filaments (actins, intermediate filaments and microtubules (MTs)), which constitute the motile cellular architecture referred to as the cytoskeleton. Moreover, these filaments act as busy rail-road networks along which various proteins travel large distances, performing various functions. While certain proteins undergo passive one-dimensional (1D) diffusion along the filaments, others (motor proteins) convert chemical energy generated from hydrolysis of *adenosine triphosphate* (ATP) into mechanical work, to move along filaments in a directed manner.

In recent years, developments in biophysical techniques such as fluorescence, electron and atomic force microscopy, X-ray crystallography, magnetic and optical tweezers along with advances in biochemical analysis, bioinformatics and genetic

engineering have revealed structural and functional understanding of the cytoskeletal filaments and the constituent motor proteins. The relevant building blocks of the cytoskeleton can now be reconstituted outside cells in *in vitro* 'minimal systems' [1]. This allows us to study the various complex biological machines in a tunable cell-free environment.

In this work, the focus is specifically on the motility strategies employed by motor proteins from the kinesin superfamily on MTs. The 1D motion of kinesins along MTs has been studied in great detail in *in vitro* motility assays. One salient feature often overlooked is that MTs are three-dimensional (3D) structures and the motor trajectory may not be linear along the MT lattice. Further, in cells, a plethora of motor proteins and MT associated proteins (MAPs) are interacting with the MT lattice simultaneously, thereby crowding the path for individual motors. Here, two new approaches were developed to study the motility of kinesins in 3D. The developed techniques were employed to study the 3D motility of yeast kinesin-8, Kip3 and dissect the structural elements essential for the observed motility features. Finally, the response of Kip3 motors on encountering roadblocks (RBs) along the MT lattice was explored.

The followings sections will discuss the structure and function of MTs and kinesin motors (1.1), introduce *in vitro* studies on kinesin motility with specific attention on kinesin-1 mechanochemical cycle, 3D motility assays and RB studies (1.2). Finally, *in vivo* and *in vitro* studies on kinesin-8 will be discussed (1.3) in order to provide the relevant questions addressed in this study (1.4).

1.1 Microtubules (MTs) and the kinesin superfamily

MTs, structure and function

MTs are rigid hollow filaments which are essential for a variety of functions within a cell in addition to providing structural support. In most eukaryotic cells, they are nucleated by the MT organizing centers (MTOCs), such as centrioles and basal bodies, which organize them in a radial manner bridging the space between centrosome and the cell periphery (Figure 1.1A). MTs are highly dynamic, capable of growing and shrinking on a time scale of seconds to minutes, a process that is

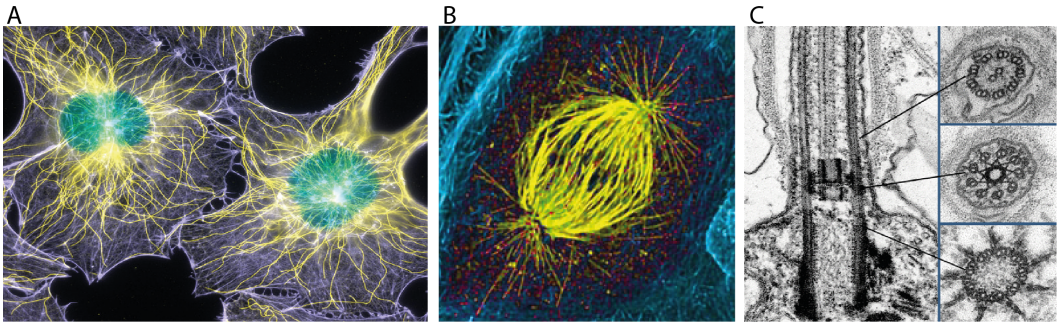

Figure 1.1: MT organization within eukaryotic cells. (A) Fluorescence image of a MT network (in yellow) organized radially outwards from the center to the cell periphery in mice fibroblast cells (photo credits: Dr. Torsten Wittmann, 2003 Nikon Photomicrography competition). **(B)** Confocal image of a mitotic spindle comprising of an organized network of MTs (in yellow) in a dividing human cell (photo credits: Dr. Ptricia Wadsworth, 2007 Olympus BioScapes Digital Imaging Competition). **(C)** Transmission electron micrographs of a Chlamydomonas cell. A longitudinal section of a centriole, transition zone and cilium aligned with the transverse sections through the corresponding regions. The complex architecture is built up of MT doublets and/or triplets [4].

regulated by a variety of microtubule associated proteins (MAPs) which thereby modulate cell shape [2]. They also provide tracks for motor proteins, like kinesin and dynein, to perform intracellular transport. The mitotic spindle, an intracellular apparatus which orchestrates the segregation of chromosomes during cell division, is made up of a highly-organized network of MTs (Figure 1.1B) [3]. The structure and dynamics of MTs in the mitotic spindle are controlled by a variety of motor proteins and other MAPs. MTs are also essential components of structures like cilia and flagella which are important for the motility of the cell (Figure 1.1C).

As illustrated in Figure 1.2A, MTs are self-assembled polymers made out of heterodimeric tubulin dimers. These heterodimers consist of two closely related 55 kDa globular proteins, α-tubulin and β-tubulin, tightly bound together. The tubulin dimers align in head-to-tail manner to form a protofilament. Several protofilaments bind laterally to form a sheet that closes up to form a hollow cylinder, the MT, with an outer and inner diameter of about 25 nm and 15 nm, respectively [2]. Therefore, the tubulin heterodimer has two types of protein-protein interactions; the longitudinal interaction of a β-tubulin in a heterodimer with the α-tubulin of another heterodimer within the same protofilament and lateral interaction between the heterodimers of neighboring protofilaments. As a result, MTs are stiff with a persistence length of several millimeters [5]. Since the tubulin

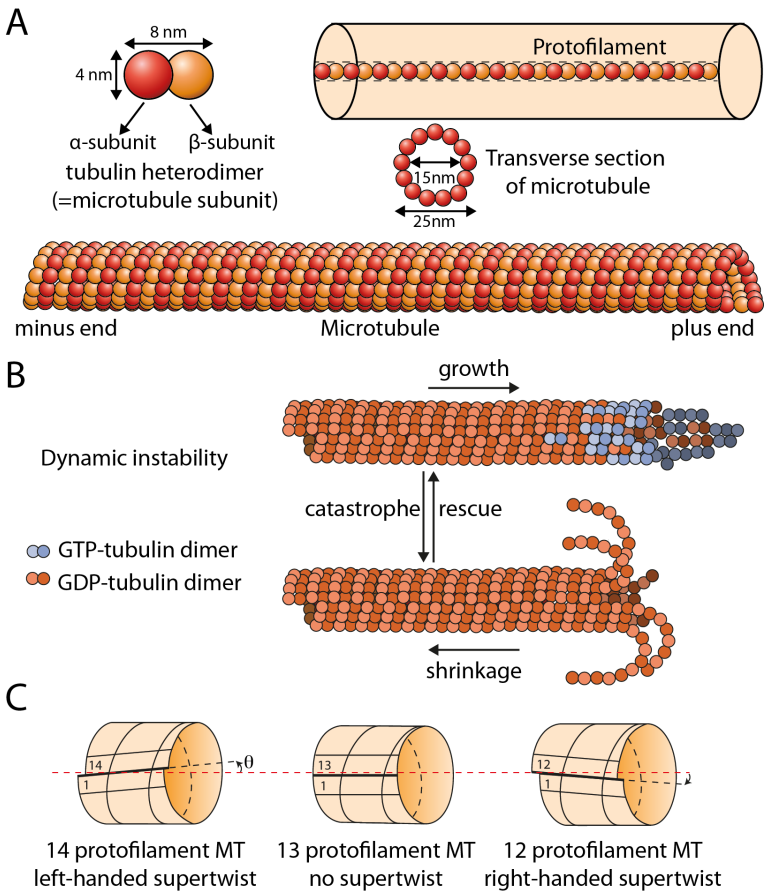

Figure 1.2: MT structure, dynamics and superstructure (A) MTs are composed of α/β tubulin heterodimers (8 nm long and 4 nm wide). Tubulin dimers align in head-to-tail manner to form a protofilament. The heterogeneity provides polarity to the MT, with the β-tubulin exposed side referred to as the plus end. 13 protofilaments associate laterally to form a hollow cylindrical MT of diameter 25 nm thick. **(B)** Dynamic instability of MT assembly. GTP-tubulin dimers attach to the growing plus end of the MTs and hydrolyze the GTP bound in the β-tubulin. When addition of new tubulin dimers is faster than GTP hydrolysis a GTP-cap is formed. Once the GTP-cap is lost, the MT tip becomes unstable, which can then lead to a catastrophe where the MT tip curls up and shrinks. Shrinking can be stopped (rescue) by addition of GTP-tubulin dimers. (image adapted from [6]) **(C)** In a 13 protofilament MT surface lattice the 'seam' between protofilaments 1 and 13 are aligned ensuring that the protofilament axis is parallel to the longitudinal axis of the MT. However, in case of 14 protofilament MTs, when an extra protofilament is added to the lattice, the seam is no longer aligned and the lattice needs to twist by an angle θ for alignment. This makes the protofilament axis left-handed supertwisted. Similarly, in case of a 12 protofilament MT, the absence of a protofilament makes the MT right-handed supertwisted. (image adapted from [7])

dimers are heterogeneous and the protofilaments are associated parallel to each other, the MT is a polar structure. The end of the MT with the β-tubulin exposed grows faster and is called the plus end and the other end is called the minus end.

In a tubulin subunit, both α and β-tubulin monomers have a *guanosine triphos-*

phate (GTP) binding site. The GTP molecule bound to α tubulin is non hydrolysable and is an integral part of the heterodimer. A β-tubulin may have a bound molecule of GTP or guanosine triphosphate (GDP), and it is exchangeable. Upon attachment of the heterodimer to a protofilament, the GTP bound to the β-subunit undergoes delayed hydrolysis. The free energy released from the hydrolysis causes a conformational change in the heterodimer which generates strain between neighboring tubulin subunits [8]. This leads to rapid depolymerization of the MT, referred to as catastrophe. However, if a GTP bound heterodimer attaches to the MT faster than the hydrolysis of the previous heterodimer, it prevents the shrinking process and growth occurs. So, a GTP-cap is necessary for stable growth of the MT [9, 10]. However, since this is a stochastic process, MTs show dynamic instability, with alternate phases of slow growth and rapid shrinking (Figure 1.2B)[11]. The dynamic instability enables rapid restructuring of the MT cytoskeleton inside the cell, which facilitates critical functions such as remodeling cell shape in response to external environment and segregation of chromosomes [12].

In vivo, MTs are typically formed by 13 protofilaments. But, when grown *in vitro* the number of protofilaments in a MT has been seen to vary from 8 to 19 [13, 14]. In MTs with 13 protofilaments, the protofilament axis and the longitudinal axis of the MT are parallel. However, for MTs with higher or lower protofilament number, in order that the protofilament sheet closes to form a MT, it twists such that the protofilaments are not parallel to the MT axis anymore [14, 15]. Thus, other than the 13 protofilament MTs, all MT types have a supertwisted alignment of their protofilaments, leading helically along the MT long axis. A 12 protofilament MT has a 2-3 µm right-handed supertwist and a 14 protofilament MT has a 7-8 µm left-handed supertwist (Figure 1.2C).

Since MTs show dynamic instability, for *in vitro* experiments they need to be stabilized. One such stabilizing drug is Paclitaxel, commonly known as Taxol, first isolated from the bark of the pacific yew tree, *Taxus brevifolia* [16]. Taxol binds specifically to the β-subunit of the tubulin dimer producing a conformational change which modifies the curvature between protofilaments, thus stabilizing the MT [8]. Another MT stabilizing method is using *guanylyl (a,b)methylenediphposphonate* (GMP-CPP) instead of GTP to polymerize MT. GMP-CPP is hydrolyzed very slowly and does not move out from the GTP binding site of the β-tubulin easily. Since GMP-CPP hydrolysis occurs at a very slow rate, the effective 'GTP cap'

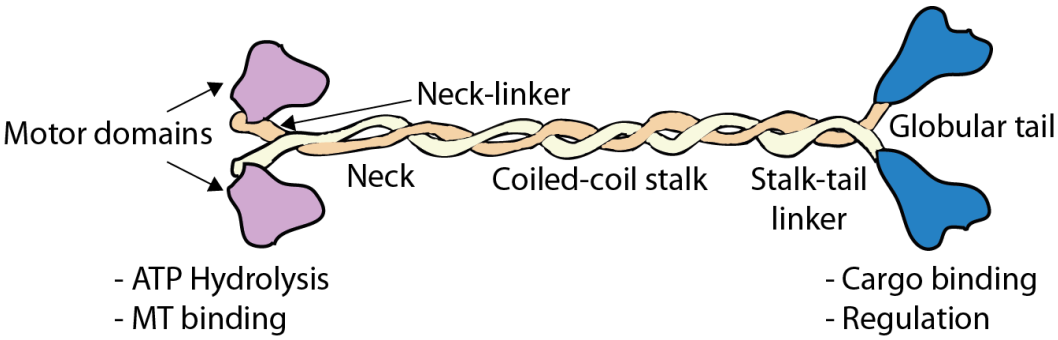

Figure 1.3: Kinesin-1 structure. Kinesin-1 is a homodimer with each monomer possessing an N-terminal motor domain (a p-loop ATPase that can associate with the MT lattice) connected to a neck via a flexible neck-linker. The neck extends to a C-terminal globular tail (essential for cargo binding) domain via a coiled-coil stalk which ensures the motor dimerization. Image adapted from Vale et al. [21].

lasts for a very long time, hence stabilizing the MTs. 96 % of the GMP-CPP grown MTs have 14 protofilaments [17] and have a much higher bending stiffness and persistence length as compared to MTs grown with GTP [18].

Kinesin superfamily

Kinesins are MT based molecular motors that have an evolutionary conserved motor domain capable of generating force. In Figure 1.3, the basic structure of kinesin-1 (the most well characterized kinesin) is illustrated. Kinesin-1 is a homodimer consisting of two motor domains at the N-terminal end of the sequence which are connected via a short neck linker to the coiled-coil domains (referred to as the stalk) followed by two globular tail domains at the C-terminal end. The motor domains (also referred to as motor heads) are phosphate-binding loop ATPases and their interaction with tubulin dimers on the MT lattice is coupled to ATP binding and hydrolysis. The flexible neck-linkers are also linked to the motor head ATPase cycle and undergo conformational changes which co-ordinate the motion of the two motor heads along a MT protofilament enabling them to 'walk' in the direction of the plus-end of MTs. The coiled-coil region of the stalk keep the motor in a dimeric state. The tail functions as a cargo binding site as well as an auto-inhibitor for ATP binding in the motor domains (when not bound to cargo) [19, 20]. The motor is finely tuned for MT plus-end directed transport of cargoes by regulatory proteins and post-translational modifications on the tail as well as the MT lattice.

In the last 30 years, more than 600 kinesins have been discovered across different species [22, 23] which have been classified into 15 families (termed kinesin-1 to kinesin-14B) [24] based on structure and function. The superfamily can be broadly grouped in numerous ways: (i) Based on the position of the motor domain in the amino acid sequence. Most kinesins have the motor domain at the N-terminal region (N-kinesins), kinesin-13 have the motor domain in the middle of the sequence (M-kinesins) while kinesin-14 have the motor domain at the C-terminal end (C-kinesins) [25]. N-kinesins and M-kinesins generate force and/or motion along the plus-end of MTs while C-kinesins are minus-end directed. (ii) Based on the oligomerization of the kinesin. While most kinesins are homodimers, few kinesins can be monomers (members of the kinesin-3 family) [26] or homotetrameric (kinesin-5) [27]. Further there are some heterodimeric or heterotrimeric kinesins (members of the kinesin-2 family) [28, 29] that have a non motor binding partner. (iii) Based on their processivity along the MT lattice. Processivity refer to the number of steps the kinesin can take during the coordinated unidirectional motion of the two motor domains along the MT lattice. Some motors are non processive (kinesin-13, kinesin-14) [30, 31] while others are processive to different extent; weakly processive (few steps; members of the kinesin-5, kinesin-2 family) [32, 33], relatively processive (>100 steps; most kinesins) and super-processive (>1000 steps; kinesin-8) [34]. (iv) Based on the functions they perform. Loosely we can group them as kinesins involved in intracellular transport (reviewed in [24]) or kinesins linked with the mitotic spindle (reviewed in [35]). While the role of kinesins in intracellular transport is intuitively understood, the role of kinesins in the self organization of the spindle apparatus is relatively less understood. The spindle contains multiple motor-driven sub-systems involved in diverse roles such as slide and crosslink MT bundles (kinesin-5, kinesin-14, kinesin-8, kinesin-12), manipulate MT dynamics (kinesin-13, kinesin-8), chromosome capture and congression (kinesin–4, kinesin-7, kinesin-8).

1.2 *In vitro* studies on kinesin motility

Conventional *in vitro assays*

Progress in the field of microscopy, development of fluorescent markers, invention and development of highly sensitive charge-coupled devide (CCD) cameras along with advancement of cell biology techniques has enabled us to reconstitute

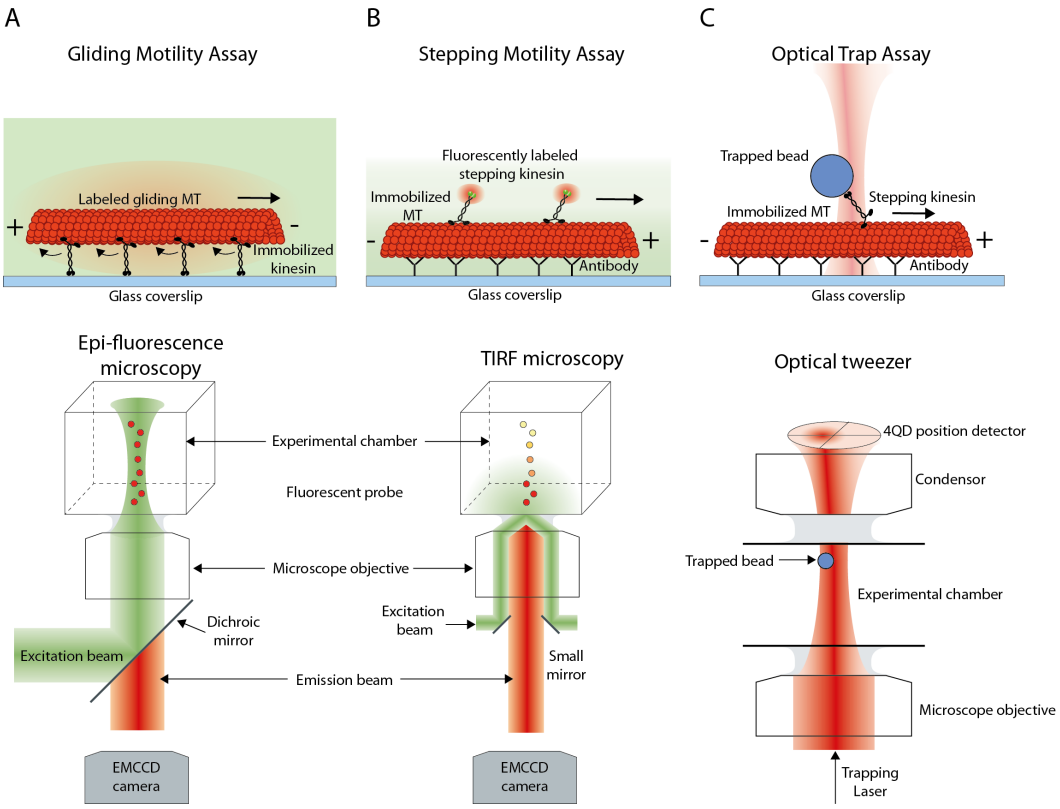

Figure 1.4: *In vitro* motility assays. (A) Conventional gliding motility assay, where motors immobilized to a glass surface glide MTs. Fluorescently labeled MTs are imaged via simple epi-fluorescence microscopy. **(B)** Conventional stepping motility assays, where single fluorescently labeled motors move along MTs are immobilized on a glass surface. The motors are imaged using total internal fluorescence (TIRF) microscopy to remove background fluorescence due to motors in solution. **(C)** Optical tweezer assays, where motors coated on a glass bead move along MTs are immobilized on a glass surface. The bead is trapped in the focus of a laser beam and pN forces can be applied (or measured) when the bead is moved (or moves) away from the laser focus. Microscopy schemes are adapted from Veigel et al. [37].

cytoskeletal motility processes in *in vitro* systems [1, 36, 37]. Such a bottom-up approach has allowed us to understand the molecular mechanism of motor proteins with detailed insight into their biophysical properties at a molecular scale. In the recent past, two different *in vitro* assays have been developed to study the motility of kinesins on MTs: (i) gliding motility assays, where MTs glide along immobilized kinesins and (ii) stepping motility assays, where kinesins step along immobilized MTs.

In gliding motility assays kinesin motors are immobilized in an inverted geometry (bound via the stalk or tail domain) on a glass substrate (by adsorption or via antibodies) which allows them to 'glide' MTs along the surface. Labeling the

tubulin incorporated in MTs with fluorescent dyes makes it possible to image the gliding MTs using standard epi-fluorescence microscopy (Figure1.4A). Gliding motility assays have been employed to investigate various motor properties, for instance, gliding velocities of MTs driven by kinesin motors [38–40], directionality of motors [41], dependence of kinesins at different nucleotide states [19, 42], the impact of viscosity of the fluid environment on motility [43], collective motor behavior [44, 45], impact of RBs on motility [46, 47], indirect measurement of motor flexibility [48], force [49] and step-size [50].

In stepping motility assays MTs are immobilized on a glass substrate via antibodies and fluorescently labeled kinesin motors stepping along the MT lattice are imaged. Since the observation of single fluorescent kinesins with standard epi-illumination is difficult due to the high background fluorescence of fluorescent motors in solution, total internal fluorescence (TIRF) microscopy is used (Figure 1.4B) [51]. In TIRF microscopy, an evanescent field is generated by the total internal reflection of laser light at the interface between a glass surface and an aqueous solution. Only fluorescent molecules within this thin evanescent field are excited and can be imaged, eliminating all the background fluorescence. Stepping motility assays have been employed to determine kinesin motility parameters [52, 53] such as single motor velocity, MT interaction time, distance travelled along the MT (runlength) as well as explore other properties such as step-size and stepping mechanism [54, 55], impact of fluid viscosity [56] and RBs on motility [46, 57, 58]. Furthermore, force response of kinesins (conjugated to polystyrene beads) in the stepping geometry can be studies in an optical tweezer assay where the beads are trapped near the laser beam focus owing to the interaction between the laser light and the bead [59] (Figure 1.4C). The motor experiences force proportional to the distance moved by the bead away from the trap, which allows the trap to apply (or measure) forces in the range of few tens of fN to 100 pN . Thus, the tweezer assay can be used to investigate the force generated by the motor per step cycle and the response of the motor motility towards assisting and resisting loads (review in Capitanio et al. and Spudich et al.[60, 61]).

Motility mechanism for kinesin-1

The working mechanism of various kinesin motors have been explored using the discussed *in vitro* motility assays. Since kinesin-1 is often taken as a model system

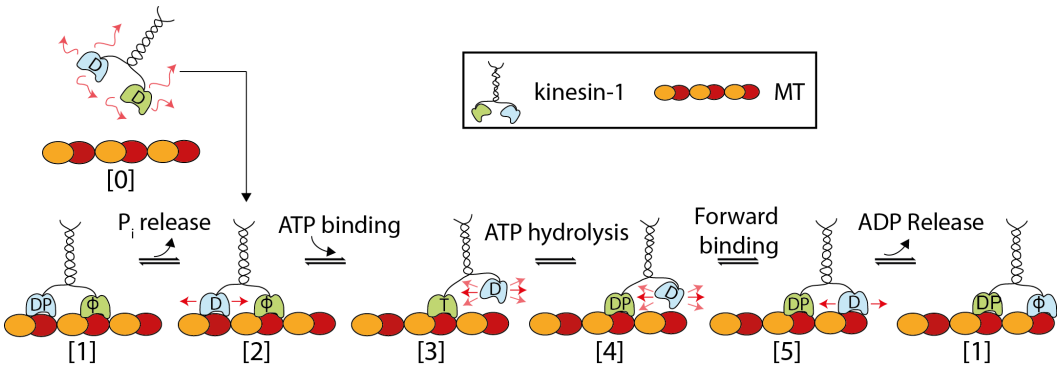

Figure 1.5: Current consensus model for the mechanochemical cycle of kinesin-1. Kinesin-1 motor heads are ADP bound in solution (state[0]). Interaction of one of the heads (leading head) with a tubulin binding site on a MT lattice triggers ADP release and the motor head tightly binds in a nucleotide-free state (state[2]). ATP binding in the leading head partially docks the neck-linker, propelling the trailing head forward (state[3]). ATP hydrolysis in the leading head fully docks the neck linker moving the trailing head to an optimal space to diffusively search for the forward tubulin-binding site (state[4]). Trailing head tightly binds the forward tubulin binding site by releasing ADP (state[5,1]) thereby completing a forward step. Leading head (now the trailing head) releases P_i and the motor returns to the beginning of the cycle (state[2]). Here leading head is labeled green, trailing head is labeled blue, T denotes ATP, D denotes ADP, DP denotes ADP plus P_i, and ϕ denotes no nucleotide.

to understand the mechanism for less studied motors, its biophysical properties are discussed here in more detail. Kinesin-1 move along the MT lattice in a processive manner which requires coordinated motion of the two motor domains [39, 62]. It steps towards the plus-end of a MT with an asymmetric hand-over-hand mechanism taking discrete 8.3 nm steps corresponding to the distance between adjacent tubulin subunits on a MT protofilament [54, 55, 63–65]. The motor interacts with the MT lattice for ~1 s taking ~100 steps [62, 66], hydrolyzing one ATP per step [19, 67, 68], before detaching from the MT lattice. The ATPase activity follows Michaelis-Menten kinetics with a K_M of ~25 µM ATP [39, 69]and a speed of ~800 nm/s at saturating ATP [19]. The ATPase cycle is tightly coupled to the motor head conformational change and the affinity to the MT lattice [70–72]. Further, a gating mechanism ensures that the ATPase activity in the two motor heads is highly coordinated ensuring processive hand-over-hand motility [54, 73–76]. Under resisting loads the motor motility slows down and comes to a stall at ~6 pN [49, 77–79] while under assisting loads the motor becomes faster but becomes highly susceptible to detach from the MT lattice [80].

The current consensus mechochemical cycle of a kinesin-1 step is illustrated in

Figure 1.5 (reviewed in Hancock et al. [81]). In solution the kinesin motor heads (ADP bound) are diffusing rapidly with a very low ADP release rate (state[0]). On interaction with the MT lattice, ADP release is triggered in one of the heads and the head (referred to as the leading head) becomes tightly bound to a tubulin binding-site in the no nucleotide state (state[2]) with the other ADP bound head (referred to as the trailing head) diffusively interacting with the MT lattice. ATP binding in the leading head steers the necklinker to transition to a partially docked conformation inducing internal strain between the two heads which propels the trailing head forward (state[3]). ATP hydrolysis then drives full neck-linker docking directing the unbound head into an optimum energy landscape to diffusively search for the next tubulin-binding site (state[4]). Upon finding the next tubulin-binding site, the trailing head (now leading head) binds tightly due to triggered ADP release (state[5,1]) and the motor makes a forward step. The ADP.P_i bound leading head (now the trailing head) release phosphate (P_i) and the motor goes back to state[2] completing the mechanochemical step cycle. Recent studies indicate that there are two rate-limiting steps in the cycle [68, 82–84]: (i) P_i release from the trailing head that gates ATP binding in the forward head (state[1]→ state[2]) [80] and (ii) forward binding after ATP hydrolysis (state[4]→ state[1]) [85]. The vulnerable state in the cycle is state[4], where P_i release from the leading head before forward binding of the trailing head would lead to the detachment of the motor from the MT lattice.

To conclude, the understanding of the step cycle allows us to explain the mechanism underlying the distinct biophysical properties of kinesin-1 and provides a template to speculate the stepping mechansim for other processive kinesins that have a slightly different mechanochemical tuning of the motor head.

3D information in *in vitro* motility assays

Since MTs are 3D structures consisting of about 13 adjacent protofilaments providing a parallel array of tracks, kinesins can have various possible trajectories during their walk: (i) they could walk straight along a single protofilament, (ii) take stochastic off axis steps to have a random trajectory or (iii) take stochastic off axis steps in one direction to have a helical trajectory. However, the aforementioned *in vitro* assays limit the investigation of motor motility only along the longitudinal axis

of the motor. Nevertheless, over the years different strategies have been employed to extend the *in vitro* assays for obtaining the 3D trajectory of motors.

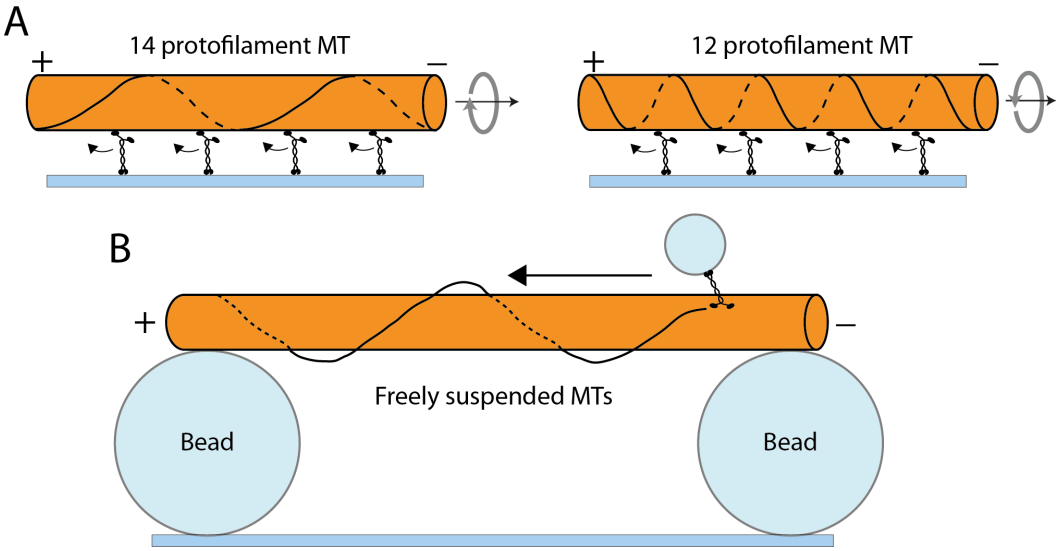

Figure 1.6: 3D motion of kinesin motors explored in *in vitro* motility assays (A) In a conventional gliding motility assay only the 2D motion of gliding MTs is imaged. However, *in vitro* MTs are mostly supertwisted and motors following a single MT protofilament would rotate the gliding MTs. For instance, 14 protofilament MTs would make left-handed rotations with 8 µm pitch and 12 protofilament MTs would make right-handed rotations with 2-3 µm pitch. Measuring the rotations of gliding MTs would therefore provide an indirect means of exploring motor trajectory on MT lattice. **(B)** In conventional stepping motility assays, we obtain the 1D trajectory of motors along the MT length. However, motors may not have a linear trajectory on MTs. To investigate the 3D trajectory of motors they should ideally be conjugated to large optical reporters and the MTs must be freely suspended to allow the motors access to the entire MT lattice. This can be achieved, for instance, by immobilizing large beads (1-3 µm) on a glass surface and immobizing the MT ends on top of them. Further, 3D imaging techniques should be developed to image the motors.

In gliding motility assays, it is possible that the gliding MTs have a torsional component to their forward motion which would be undetected in a conventional 2D-microscopy set-up. Since, *in vitro* grown MTs have protofilaments supercoiled around the longitudinal axis of the MT (other than the fraction of MTs with 13 protofilaments), a motor walking along a single MT protofilament would potentially rotate gliding MTs with rotational pitches similar to the supertwist of the MT (left-handed 8 µm rotations for 14 protofilament MTs and right-handed 2-3 µm rotations for 12 protofilament MTs; Figure 1.6A). In 1993, S Ray et al. [13] employed a crude but efficient method to look at rotational motion of gliding MTs. They grew MTs with artificial kinks which acted as sufficient markers for

rotation, since they show periodic sideways deflection with respect to the rest of the MT when the MT rotates. Using this approach, they showed that kinesin-1 motors walk along a single MT protofilament. Since then, other similar approaches based on filament supercoiling have been used for optical detection of rotations [41, 86–88]. These methods are efficient to make qualitative observations about the rotations but have limited accuracy when it comes to quantification of the rotational periodicities since the kinks have a negative impact on gliding and rotation of MTs. For quantitative investigation of MT rotations with high accuracy, in recent studies MTs were conjugated with quantum dots (QDots) which were then used as optical reporters for rotation. The 3D helical path of the QDots were tracked using three-dimensional tracking techniques based on dual-focus imaging [89, 90] or fluorescence interference contrast (FLIC) microscopy [91–93].

In stepping motility assays, the kinesin motors are normally labeled with synthetic fluorophores (fluorescein, rhodamine, alexa-dyes, etc.) or fused in their sequence with fluorescent proteins (green fluorescent protein [GFP], yellow fluorescent protein [YFP], etc.). The localization precision (the uncertainty in localizing an object) of such fluorescent markers are in the range of 10-100 nm [57]. Further, the fluorescent marker is often on the flexible C-terminal tail which further reduces the localization precision. Since MTs are only 25 nm wide, conventional stepping motility assays can only be employed to look at motion of kinesin along the longitudinal axis of the MT with no relevant axial information. To overcome this limitation in resolution some studies have conjugated kinesin (and dynein) motor domains with significantly larger optical probes (QDots, gold nanoparticles) imaged using conventional fluorescence microscopy or scattering approaches (dark-field or interferometric scattering microscopy) in order to resolve the 2D motion of kinesins along the MT lattice [84, 94, 95]. However, one fundamental problem with obtaining 3D information in the stepping motility assay geometry is that MTs are immoblized on the surface which does not allow motors access to the entire lattice of MTs. In order to overcome this problem, the MT needs to be suspended freely (as seen in Figure 1.6B). Three different approaches have been used in previous studies to freely suspend MTs by immobilizing their ends (i) on parallel relief structures (≥2 µm high) patterned on glass [96], (ii) on large beads (≥2 µm high) immobilized on glass [97] or (iii) on large beads (≥2 µm high) held in solution via optical tweezers [98]. In all these studies, the desired motor protein was coated

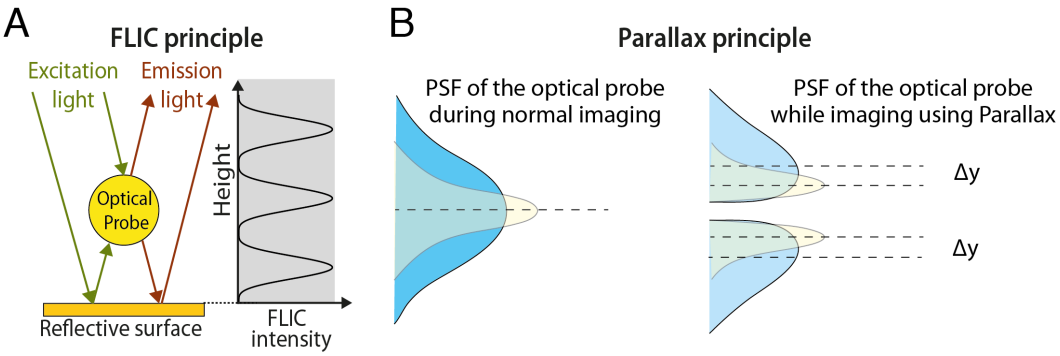

Figure 1.7: Principle of 3D imaging techniques, FLIC and Parallax. (A) Illustration of the principle of FLIC microscopy on a reflective surface. An optical probe is excited simultaneously by direct and reflected light. Similarly, the fluorescent emission also has a direct and a reflected component. Interference between the direct and reflected components of light leads to a periodic modulation of the detected fluorescence as a function of height above the reflective surface. **(B)** Illustration of the principle of Parallax. In case of a normal point spread function (PSF) for an optical probe in focus (yellow in left image) a shift in z spreads the PSF (blue in left image) but does not change the central position. In Parallax, the PSF is split along the y-axis (or x-axis) into two asymmetric PSFs (yellow in right image). A shift along the z-axis in such a system leads to a relative shift in y between the central positions of the two split PSFs (blue in right image). Therefore, a relative shift Δy between the two split PSFs provide z information of the imaged object.

on large glass beads (~500 nm) and the motility was imaged using bright-field microscopy which only provides qualitative z-information. Further developments in designing such 3D stepping motility assays are necessary to obtain precise 3D trajectories for single kinesin motors.

In order to obtain 3D motility information of kinesin motors on MTs, 3D tracking microscopy approaches have to be developed. In recent years a number of different strategies have been developed for 3D tracking by optical microscopy based on FLIC microscopy [99], confocal imaging [100, 101], light-sheet microscopy [102], and manipulation of the beam path of the image (reviewed in Deschout et al. [103]). In this study, two such approaches, FLIC and Parallax, have been utilized. Therefore, the working principle of these techniques are described briefly below:

- **FLIC microscopy:** FLIC occurs when fluorescent objects are in the vicinity of a reflective surface. The principle of FLIC is illustrated in Figure 1.7A. Briefly, excitation light excites a optical probe either directly or via the reflective surface. A similar light path exists for the light emitted by the excited optical probe. The resulting interference between the direct and reflected light generates standing waves that have a sinusoidal amplitude

distribution with respect to the height of the probe above the reflective surface. This leads to a $\sin^4$ modulation of the intensity of the optical probe as a function of the height above the surface, with the first maximum of the FLIC intensity curve appearing at 100-150 nm above the reflecting surface [99, 104]. Therefore, FLIC microscopy can be used to measure the relative change in height of a fluorescent probe with nanometer precision by measuring the change in intensity of the probe. In our laboratory, FLIC microscopy has been utilized to study the 3D motility of QDot conjugated MTs gliding on reflective silicon wafers coated with kinesin motors [91, 92].

- **Parallax:** Parallax is a dual focus imaging technique in which the image beam path is split at the Fourier plane (a plane conjugate to the objective back focal plane). The basic principle is illustrated in Figure 1.7B. When the beam path is split along the y-axis (or x-axis) in the Fourier plane, the point spread function (PSF) corresponding to each optical probe at the image plane is split into half creating two antagonistic PSFs asymmetric along the y-axis. For a regular PSF of an image in focus, any motion out of focus in z direction results in the spreading of the PSF. However, the central position determined from the peak of the Gaussian fitted to the PSF does not change and we obtain no information regarding the z direction. In case of Parallax the two asymmetric PSFs corresponding to an image in focus also spread with movement of the image out of focus in the z direction. However, since the PSFs are asymmetric along the y axis, the central position of the PSFs shift in y direction and the relative change in y (Δy) between the two PSFs is proportional to the shift of the image in z. Sun et al. utilized this technique to study the 3D motility of single Myosin X motors stepping on freely suspended actin filaments [105].

Kinesin motility in the presence of roadblocks

In vivo a variety of MAPs simultaneously interact with a MT lattice. These include kinesins, non-motor MT stabilizing, destabilizing and crosslinking factors, passenger proteins and MT end-tracking proteins [106]. These MAPs interact stochastically with the MT lattice in a directed, diffusive or static manner thereby acting as RBs which obstruct the path of kinesin motors. Several *in vitro* studies have probed the response of kinesins (mostly kinesin-1 and kinesin-2) on encountering

various kinds of RBs such as purified MAPs (like tau) [58, 96, 107–110], cell extracts [111], motor proteins in crowding conditions [112, 113], or artificial RBs like streptavidin, QDots [46] and dead kinesins [57, 111, 113–115]. It was observed that RBs generally retard motility parameters such as velocity, runlength, MT interaction time and the landing rate of kinesins, with the motor either detaching, pausing or sidestepping during a RB encounter. Based on these observations different motor strategies to circumnavigate RBs have been hypothesized which are briefly discussed below.

- The motor could detach from a MT immediately on encountering a RB [46, 57, 111]. However, immediate rebinding (in the millisecond timescale) to a different tubulin binding site on the MT lattice is possible [57] and would depend on the 3D diffusion constant of the motor. In cells, motors like kinesin-1 and kinesin-2 are loaded with large cargoes which would have a very low diffusion constant (in comparison to an unloaded motor) allowing them to utilize such a strategy to circumnavigate a RB.

- The motor could pause on encountering a RB [46, 57, 111]. Since, physiological RBs are often diffusive and/or can detach from the MT lattice with a stochastic probability which might be accelerated when a motor bumps into them, pausing in a waiting phase for removal of RB may indeed be a strategy to circumnavigate RBs. Indeed, in studies on kinesin-1 with neuronal MAPs used as roadblocks only a marginal effect is seen on motor velocity, run length and MT interaction time [58, 96, 107–111] in contrast to studies using static artificial RBs where kinesins motors mostly paused and detached.

- The motor could side-step on encountering RBs. This hypothesis has gained significant relevance over the years. While kinesin-1 has been shown to follow a single MT protofilament [13, 91], recent 3D rotation studies on other kinesins indicate that most other kinesins (and dynein) are likely to side-step stochastically [89, 92, 93, 97, 98]. The structural adaptation speculated to be essential for providing motors the capacity to switch protofilament is a longer neck-linker and/or a flexible neck [58, 92]. Details of the side-stepping mechanism still remain unexplored and there are several unanswered questions like: (i) Is side-stepping incoporated within the step cycle? (ii) Is it diffusive

or directed? (iii) Is the side-stepping behavior enhanced upon encountering RBs or is it an intrinsic property?

1.3 Kip3, a member of the kinesin-8 family

In vivo studies on kinesin-8

Members of the kinesin-8 family studied in literature include human Kif18A, Kif18b, Kif19A, budding yeast Kip3, fission yeast Klp5, Klp6 and fruit fly Klp67A. During mitosis, most of these proteins localize to the plus end of kinetochore MTs indicating an evolutionarily conserved function. Suppressing its expression or deleting these motors using established genetic engineering protocols increases the length of mitotic spindle and induces late onset of chromosome segregation [116–122]. During early mitosis, chromosomes normally undergo coordinated oscillations in order to align properly. Deletion of kinesin-8 motors increase the amplitude of such nuclear oscillations eventually causing improper alignment of chromosomes at the intersection of the spindle, referred to as the metaphase plate [121]. As a consequence, chromosomes are often mis-segregated during mitosis [117, 123–125]. In further studies, it has been shown that motors from the kinesin-8 family promote MT catastrophes and slow down the rate of MT growth as well as slow down the MT shrinkage rate and increase the frequency of MT rescues [126–128]. The functions of kinesin-8 motors are not just restricted to mitosis. In fission yeast, kinesin-8 motors are essential in positioning the nucleus at the cell-center and maintain cell polarity by regulating the dynamics of MT bundles nucleated from the MTOCs [129–131]. Further, human Kif19A was observed to accumulate at cilia tips and control the length of cilia [132]. This ensemble of evidence indicate that kinesin-8 motors are essential regulators of MT dynamics in the cell.

In vitro studies on Kip3

Several groups have performed *in vitro* studies on kinesin-8 motors (specifically budding yeast Kip3) and discovered two biophysical properties essential for their biological role: (i) super-processive motility to the MT plus-end and (ii) MT depolymerase activity at the plus-end.

Illustration of the protein sequence of Kip3 can be seen in Figure 1.8A. *In vitro* studies on Kip3 reveal that the homodimeric motors are plus-end directed,

slow (motor velocity is ~50 nm/s in comparison to ~800 nm/s for kinesin-1) and super-processive (runlength >11 µm in comparison to ~1 µm for kinesin-1, Figure 1.8B) [34, 95]. The runlength of these motors are significantly longer than the cellular length of MTs as a consequence of which once the motors land on the MT lattice they reach the MT plus-ends. Apart from the regular motor head interaction with the MT, kinesin-8 motors have other structural elements (conserved loop structures in the motor heads and certain domains in the tail region) that associate with the MT lattice which possibly contribute to its super-processivity [133–136]. Optical tweezer studies on single Kip3 motors have shown that Kip3 is a 'slippery' low force (stall force ~1 pN) motor and can switch out of the mechanochemical cycle to a diffusive slip state on applying force, allowing it to move back and forth [137].

In vitro studies showed the Kip3 promote catastrophes in dynamic MTs [138] and actively depolymerize MTs stabilized with Taxol or GMP-CPP [34, 95, 127]. Further, it was observed that while double-stabilized MTs (stabilized by both GMP-CPP and Taxol) resist Kip3 mediated depolymerization, Kip3 motors remain strongly associated with MT ends (with end-residence time >75 s at low Kip3 concentrations) [95]. A recent study reveals that Kip3 switches its mode of interaction at the plus end by a strong, preferential binding to curved tubulin (which also suppress its ATPase activity) [134]. Further, the Kip3 tail domain promotes MT plus-end binding possibly due to interactions with the tubulin surface accessible only at MT ends [136]. This strong interaction at the plus-end allow incoming Kip3 motors to rip off end residing tubulin dimers in stabilized MTs and initiate catastrophes in dynamic MTs. Another interesting observation made in a study was that the Kip3 tail domain reduces the shrinking rate of dynamic MTs which would explain why kinesin-8 suppress the overall MT dynamics in cells (and not just the MT growth) [136].

Kip3 motors undergo a significantly high energetic cost to depolymerize MT since they take hundreds of steps (hydrolyzing that many molecules of ATP) in order to depolymerize one (or a few) tubulin dimers. In comparison, all other known MT dynamics regulators (like kinesin-13 [30], Dis1/XMap215 family [139], EB1 [140]) either undergo 1D diffusion along the MT lattice or shuttle along MT based motors to find the MT ends. The key advantage gained by Kip3 motors in combining processive motility with MT end regulation is that it can depolymerize

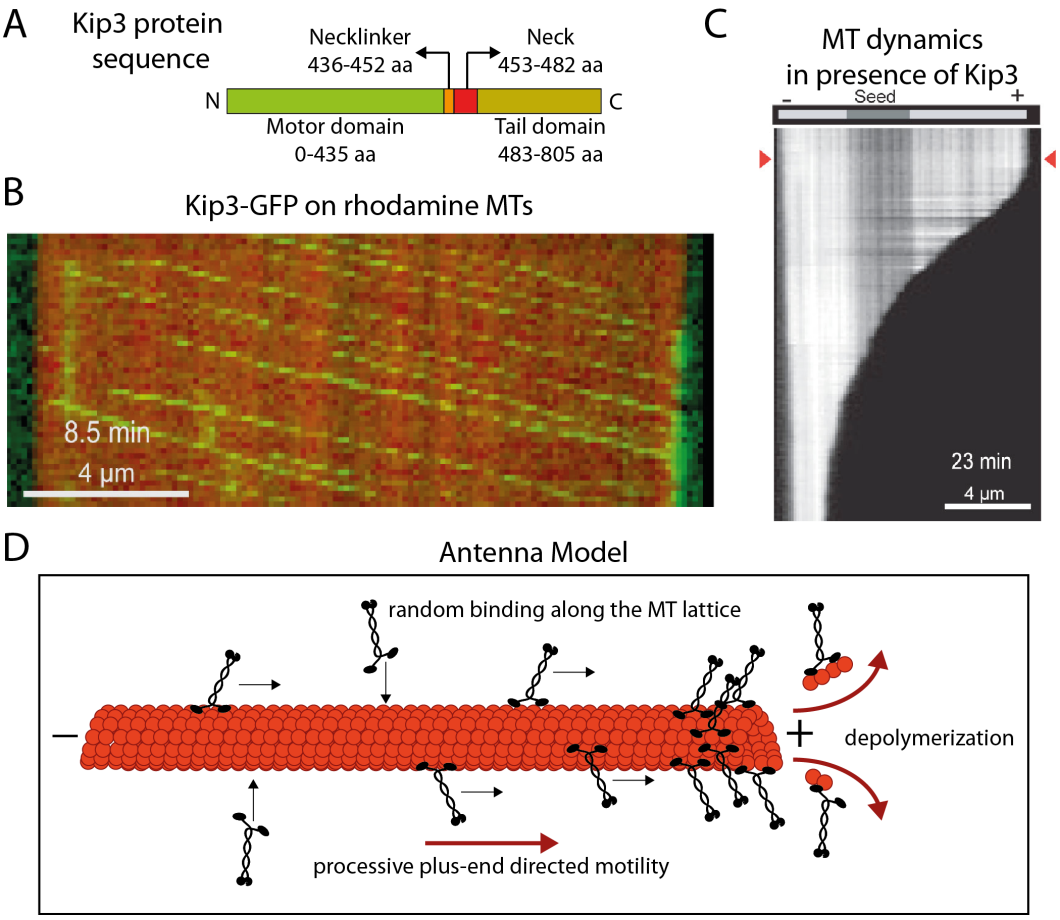

Figure 1.8: Kip3 steps processively to MT plus-ends to depolymerize them. (A) Illustration of the protein sequence of Kip3. The motor domain is 435 amino acid (aa) long followed by a 17aa long necklinker. The motor dimerizes due to the short coiled-coil neck which is followed by the tail domain. **(B)** Kymograph (space-time intensity plot) of GFP labeled Kip3 motors (green) moving along a rhodamine labeled double stabilized MT (red). The motors land along the ~18 µm long MT lattice and walk processively to the MT plus end where they associate strongly. **(C)** Kymograph of a MT being depolymerized by Kip3 motors. Red arrowheads indicate addition of 7 nM Kip3. The rate of depolymerization scales with the length of the MT with fast depolymerization when the MT is long. **(D)** Illustration of the antenna model. Motors randomly bind along the MT lattice and the number of landings within a time interval is proportional to the length of the MT. Super-processivity ensures that the motors reach the MT plus end where they cause depolymerization. This leads to faster depolymerization of longer MTs. Data was taken from the thesis of Vladimir Varga and the antenna model was adapted from Varga et al. [34, 95].

MTs in a length-dependent manner (see example kymograph in Figure 1.8C). Since motors bind along the entire lengths of MTs and subsequently walk to the plus-ends where they bind tightly in order to rip off tubulin dimers, they act like antennas which enables the MT to 'sense' its length (Figure 1.8D) [34, 95]. Ultimately, this

leads to a length regulation mechanism for MTs where the rate of depolymerization is dependent on the length of the MT [141, 142].

1.4 Questions addressed in this study

The unique biophysical properties of Kip3 enable it to regulate the micrometer scale lengths of MTs. In order for the length regulation to be effective, it is essential that individual Kip3 motors reach the MT end. However, in cells, MTs are likely to be crowded with other MAPs that obstruct the path of individual Kip3 motors. Further, Kip3 itself creates traffic jams near the MT plus-ends due to its biophysical properties. Has the motor evolved a strategy to avoid RBs and navigate through traffic jams to reach its ultimate goal, the MT plus-end? If so, how does it circumnavigate obstacles? Does it side-step? Is the side-stepping diffusive and unbiased or is it directed? Is the sidestepping linked within the mechanochemical cycle or does the motor switch out of the cycle into a different mode? Is the motor side-stepping in response to RBs or is it an intrinsic motility characteristics? These are the questions addressed in this study.

The next two chapters describe the development of two novel approaches to study the 3D motility of Kip3 motors, one in the gliding motility assay geometry (Chapter 2) and the other in the stepping motility assay geometry (Chapter 3). In Chapter 4, the stepping mechanism for Kip3 is examined and a new mechanochemical cycle for is proposed in order to account for the motors side-stepping behavior. Finally, in Chapter 5, the response of Kip3 motors to static RBs is explored and a comprehensive stepping mechanism for Kip3 is proposed. The material and methods as well as supplementary figures are presented at the end of the thesis.

CHAPTER 2

Rotational motion of MTs gliding on Kip3

Knowledge about the 3D stepping of kinesins on the surface of MTs can be inferred indirectly from longitudinal MT rotations in gliding motility assays. Here, fluorescence interference contrast (FLIC) microscopy is utilized to probe the motion of QDots conjugated to MTs gliding on Kip3 motors, as described in Nitzsche et al. [91]. However, it is observed that QDots can hinder free rotation of MTs, specifically if the torque generated by the motor is low. To avoid artifacts due to bulky external optical probes, a FLIC gliding motility assay using rhodamine speckled MTs is established, where the speckles incorporated within the MT lattice are used as the optical reporters. This novel technique is used to probe the rotational motion of MTs gliding on Kip3, revealing that Kip3 motors rotate gliding MTs with short left-handed pitches of ~1-1.5 µm. *These rotations indicate that Kip3 switches protofilaments with a bias towards the left.*

The results presented in this chapter have partly been published in Bormuth et al. [92] and Mitra et al. [93]

2.1 Gliding motility assay on Kip3 motors was established

In order to obtain 3D motion of MTs gliding on Kip3 motors, it was necessary to establish gliding motility assays that are reproducible. A Kip3 construct with an eGFP (enhanced GFP) tag and a 6x His tag, both at the C-terminal tail (hereafter referred to as Kip3-eGFP or Kip3) was expressed in insect cells and purified using His affinity chromatography. The general schematics of the optimized gliding motility assay geometry (illustrated in Figure 2.1A) are as follows: (i) Fab fragments (from Anti-mouse IgG [Fc specific) antibody) were adsorbed on a hydrophobic surface and (ii) the remaining surface was blocked by pluronic F-127 (an amphiphilic block copolymer). (iii) The Fc region of GFP antibodies (developed in mice) bound specifically to the Fab fragments, such that the GFP binding domains of the antibodies faces away from the surface. (iv) Kip3-eGFP motors bound specifically to the GFP antibodies via their eGFP tag on their tail domain. (v) MTs introduced in the presence of ATP moved robustly along the surface coated with Kip3-eGFP motors.

MT gliding was uniform and robust at high or intermediate surface densities of Kip3 motors (concentration of Fab fragments determine the motor density) while at low motor densities gliding was poor with high translocation fluctuations. The gliding velocity was found to be significantly lower than the single molecule velocity for Kip3 (~50 nm/s [34, 95]). However, on systematically lowering the motor surface densities, it was observed that the gliding velocity increased, approaching single molecule velocity at very low motor densities (Figure 2.1B). Further, the gliding velocity also increased over time in individual experiments, presumably caused by a progressive reduction of the motor density due to partial motor unbinding from the surface and/or motor inactivation as also indicated by a concurrent decrease in the number of gliding MTs per field of view (Figure 2.1C). Therefore, a large variation in Kip3 driven MT gliding velocity (20-50 nm/s) was observed which is dependent on the surface density of motors possibly due to collective motor effects.

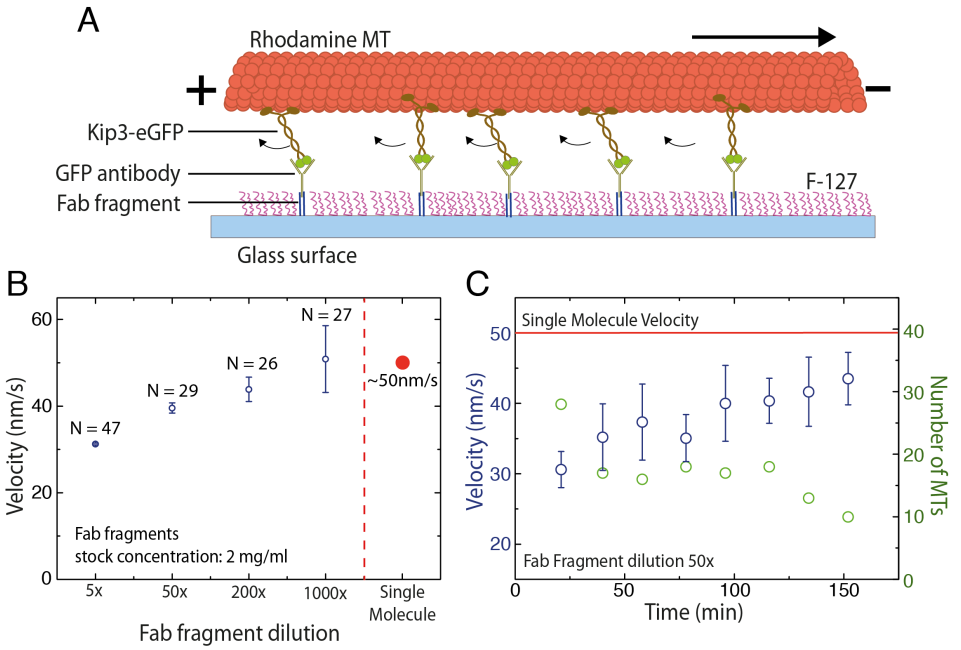

Figure 2.1: MT gliding velocity depends on the surface density of Kip3 motors. (A) Schematic representation of MTs gliding on a surface coated with Kip3-eGFP motors via GFP antibodies (attached specifically to the surface via secondary Fab fragments after the surface is blocked for unspecific interactions by pluronic F-127). **(B)** MT gliding velocity for different Fab fragment dilutions (31.2 ± 1.0 nm/s at 5x, 39.6 ± 1.0 nm/s at 50x, 43.8 ± 3.0 nm/s at 200x and 51.0 ± 8.0 nm/s at 1000x dilution; Fab fragment stock concentration- 2 mg/ml). The Fab fragment concentration determines the Kip3 motor density on the surface. The gliding velocity increases on reducing number of motors on the surface with almost single molecule velocity (measured in stepping assays; velocity ~50 nm/s [34, 95]) at 1000x dilution. **(C)** Gliding velocity plotted over time for Kip3 gliding motility assay at 50x Fab fragment dilution. The gliding velocity is much lower than the single molecule velocity but increases over time. The decrease in the number of gliding MTs per field of view (green points) indicates a reduction in the effective density of motors with time.

2.2 QDots provide qualitative rotational information of MTs gliding on Kip3

In order to observe the rotational motion of MTs gliding on Kip3 motors, 3D motion of QDots conjugated to gliding MTs was probed using FLIC microscopy, as established previously for MTs gliding on kinesin-1 [91] and kinesin-14 [143].

In Nitzsche et al. [91], QDot conjugated MTs gliding on a reflective silicon wafer coated with kinesin-1 motors were imaged using FLIC microscopy. The streptavidin coated QDots (QDot655 conjugate having 5-10 streptavidin molecules per QDot) were conjugated to MTs sparsely labeled with biotin (ratio of unlabeled to biotin labeled tubulin was 1:50) via biotin-streptavidin interaction. The MTs

were grown with GMP-CPP (and further stabilized with Taxol) which provided a homogenous population of 14 protofilament MTs (~95 % [17, 144]) that have an intrinsic left-handed supertwist of ~8 µm [17, 91]. 3D motion of the QDots linked to gliding MTs was determined by combining the height information (obtained from FLIC intensity modulation) with 2D nanometer tracking (using FIESTA, a fluoresecent image evaluation software for tracking and analysis developed in MATLAB [145]). It was observed that MTs gliding on kinesin-1 rotated with a constant rotational pitch of ~7.9 µm confirming previous results which suggest that kinesin-1 moves along the same MT protofilament [13].

The same approach was utilized (as illustrated in Figure 2.2A) to measure the 3D motion of MTs gliding on Kip3-eGFP motors. The intensity profile of QDots linked to gliding MTs revealed periodic modulation of ~1 µm, as can be seen in the maximum projection for an example QDot event (Figure 2.2B). Combining the sideways information (obtained from tracking) and the FLIC intensity information (see Figure 2.2C), it was observed that the rotations were left-handed. This result is in stark contrast to MT gliding on kinesin-1 and suggests that Kip3 motors do not follow a single MT protofilament but makes directed side-steps to the left.

Limitations of using QDots as optical reporters

While preliminary results revealed that Kip3 motors rotate gliding MTs with short left-handed periods, comprehensive quantitative characterization of the 3D motion of MTs using this approach was not performed due to a number of limitations in the technique. These limitations are discussed below.

- The QDots are bulky probes, ellipsoidal in shape with dimensions of 18 nm (minor axis diameter) and 24 nm (major axis diameter) excluding the streptavidin molecules (with streptavidin the size is 28-34 nm since the diameter of streptavidin is ~5 nm [146]). Since the motors hold MTs at a height in the range of 15-30 nm [99] the QDot would force the gliding MTs to detach partially whenever they are between the MT and the surface, thereby providing friction to the MT motion. Indeed, numerous events were observed where the QDots would momentarily get stuck while moving under the MT. Further, MT gliding was effected significantly due to QDots, specifically in assays under limiting ATP conditions. These is discussed in more detail later in this chapter.

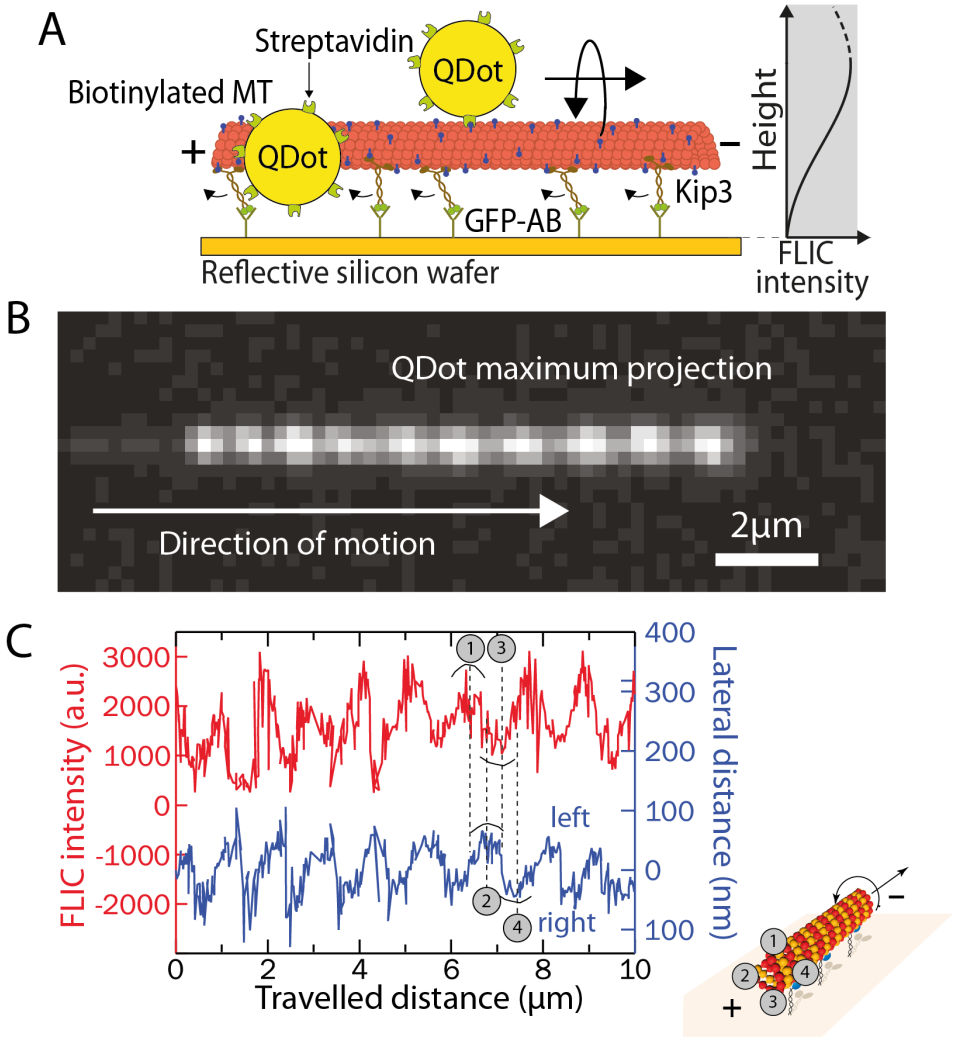

Figure 2.2: FLIC microscopy on QDot-coated MTs gliding on Kip3 reveal short left-handed rotational pitches. (A) Principle of FLIC microscopy on a reflective surface. An optical probe is excited simultaneously by direct and reflected light. Similarly, the fluorescent emission also has a direct and a reflected component. Interference between the direct and reflected components of light leads to a periodic modulation of the detected fluorescence as a function of height above the reflective surface. **(B)** Illustration of FLIC microscopy on QDot labeled MTs gliding on a reflective silicon surface coated with Kip3 motors. Due to fluorescence interference contrast microscopy (FLIC) the recorded intensities of the QDots increase as a function of height above the substrate. Rotational information of gliding speckled MTs is interpreted from the variation in the recorded intensity of the QDots. **(C)** Typical maximum projection for a QDot attached to a MT gliding over Kip3 motors. **(D)** FLIC intensity (red) and lateral distance from the MT path (blue) of the QDot shown in **(C)** vs. traveled distance along the MT path. The periodic FLIC signal is indicative of repeated up and down motion. The example QDot has a rotational pitch of ~1.1 µm and the rotational direction is left-handed (illustration) as derived from the temporal sequence of the 3D positions relative to the MT

- The conjugation chemistry of the streptavidin coated QDots to biotinylated MTs was not reliable. The optimum conjugation ratio, in order to obtain enough relevant events but avoid QDot clustering, had to be varied between experiments. Further, QDots often bound unspecifically to the assay surface (possibly due to issues related to F-127 blocking) making the evaluation of relevant data difficult.

- It is possible that some streptavidin molecules get off the QDot surface and the free streptavidin compete with the QDot binding interactions. This leads to frequent unbinding of QDots from the MT lattice. Since Kip3 driven MT gliding is slow (20-50 nm/s), QDots often detach prematurely before long duration events (>1 min) can be acquired.

- QDots undergo fluorescence intermittency and are susceptible to chemical quenching. Further, these properties get more significant over time and the same batch of QDots cannot be used for more than a few months.

2.3 Speckled MTs (S-MTs) can be used to quantitatively characterize rotations of gliding MTs

In order to avoid the limitaions of using QDots as optical reporters, MTs were reconstituted by inhomogeneous copolymerization of unlabeled tubulin with rhodamine-labeled tubulin such that the MTs were decorated with bright rhodamine speckles, which acted as optical probes. To establish the analysis method for obtaining rotational information, gliding motility assays using speckled MTs in combination with FLIC microscopy (referred to as speckle FLIC gliding assays) were firstly performed on kinesin-1 and the obtained rotational data was compared with previous studies.

Speckle analysis provides the rotational pitch of gliding MTs

Speckled MTs (S-MTs) gliding on kinesin-1 coated surfaces (see illustration in Figure 2.3A) were imaged and for every S-MT without a crossing event a kymograph was generated (typical example kymograph in Figure 2.3B). To extract the periodicity of the individual speckles, which exhibit periodic intensity variations over

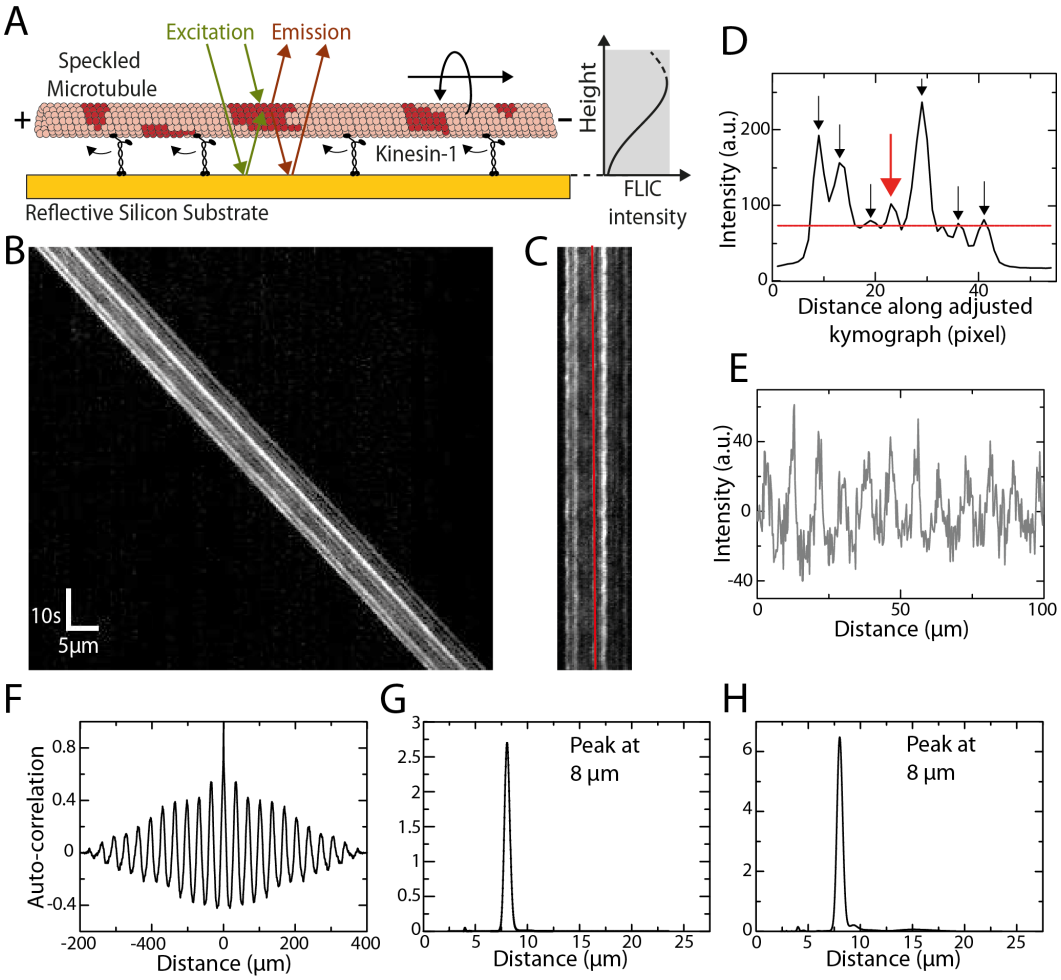

Figure 2.3: Strategy to analyze the rotational pitch of gliding S-MTs. (A) Rhodamine speckled MTs glide on a reflective silicon substrate coated with kinesin-1 motor proteins. Here the speckles act as optical reporters and the periodic variations in the intensity of each speckle due to FLIC provides information regarding the rotational pitch of gliding S-MT. **(B)** Typical kymograph (space-time intensity plot) of a S-MT gliding on kinesin-1. Each individual speckle shows a periodic intensity variation. **(C)** After background correction, the kymograph is straightened by shifting every time frame by the distance the S-MT moved. **(D)** Averaged intensity profile along the straightened kymograph from (C). The red line shows the mean intensity and only speckles with peaks above this line (indicated by the arrows) are analyzed. **(E)** Relative intensity profile (centered around zero) over travelled distance for the speckle along the red line in (C) and indicated by the red arrow in (D). This profile is obtained by translating the intensity profile over time to distance in order to account for velocity variations of the gliding S-MT. **(F)** Auto-correlation for the intensity plot in (E). **(G)** Power spectrum of the auto-correlation data in Fig (F), with peak at about 8μm. **(H)** Combined power spectral density (PSD) curve for the seven speckles selected in (D) (see Supplementary Figure 1 for details on the other speckles), with peak at about 8μm.

time, the following procedure was used: (i) Background correction was performed by subtracting the minimum pixel intensity along the kymograph column from all pixel intensity values in the respective column. For MTs moving significantly larger distances than the MT length over a rather inhomogeneous background the average intensity of each kymograph column (instead of the minimum) was subtracted. (ii) The kymograph was 'straightened' by taking the intensity of the first horizontal line of the kymograph (which refers to the first time-frame) as a reference and cross-correlating it with the remaining lines in order to find how many pixels each time-frame needs to be shifted (Figure 2.3C). This pixel shift information for each time-frame also yields the instantaneous velocity. (iii) Speckles on the 'straightened' kymograph were chosen by averaging the intensity along the MT over time and selecting the peaks from the averaged intensity profile (Figure 2.3D). In order to avoid noisy data, extremely dim speckles were ignored by selecting only peaks that were above the mean value of the averaged intensity profile. (iv) For each selected speckle, the intensity profile (averaged over a width of three pixels to overcome any inaccuracy due to pixelation of the 'straightened' kymograph) over time was interpolated to an intensity profile over distance using the instantaneous velocity information (especially important for MTs gliding with variable velocities). The resulting intensity profiles of the speckles showed a periodic variation in the intensity (Figure 2.3E and Supp. Figure A1). (v) Performing an auto-correlation on the intensity profile for individual speckles (Figure 2.3F and Figure A1) and subsequently obtaining the power spectral density (PSD) (using the smoothed periodogram method with a Hamming window) of the autocorrelation data yields the peaks corresponding to the spatial frequencies in the intensity signal for the speckles. For the example gliding event in Figure 2.3, the highest peak in the PSD curve for each speckle was approximately at 8 µm (Figure 2.3G and Supp. Figure A1) indicating that each speckle completed one rotation approximately every 8 µm. This strategy is preferred over directly obtaining the PSD of the intensity profile of the speckles since the latter would give significance to bright speckles rather than to speckles with a pronounced periodicity. Use of the PSD of the auto-correlation removes the contribution of the intensity of the speckle and emphasizes only the periodicity of the intensity variation. (vi) The pitch of rotation of the gliding S-MT under investigation is then obtained by summation of the PSD curves for all individual speckles. The highest peak in the combined PSD curve (Figure 2.4G)

yields the average rotational pitch of the specific S-MT.

Often, as in the case of the example kymograph (3rd and 4th speckle; see Figure 2.3E and Supp. Figure A1), the intensity variations of dimmer speckles were more pronounced than the variations of brighter speckles, which were most likely a combination of two or more speckles in close proximity. In fact, if two speckles approximately 90° apart on the MT lattice are in close proximity they are detected as one speckle, but will also exhibit a pitch roughly half of the rotational pitch of the MT. The PSD for that particular speckle would include two peaks, one for the true rotational pitch and one at roughly half of the true pitch, due to the superimposition of the intensity from both of the speckles. In a large number of kymographs, a small peak was observed at half the pitch of rotation in the combined PSD curve (see kymograph 2,4 in Supp. Figure A2), however, the half peak was almost never significantly large since the rotational pitch is obtained by averaging over a number of speckles.

The peaks in the PSD curve have a characteristic height and width. The peaks are higher for an auto-correlation with pronounced side peaks, implying that all the periods in the intensity profile look very similar. If the periods in the intensity profile have large internal variations due to uneven background noise, uneven illumination, bleaching or clusters of speckles, the peaks in the PSD curve will be small. The height of the peak is therefore just an indication of the quality of the kymograph. The width of the peaks in the PSD curve depends on a number of factors: (i) the spectral window chosen for fitting the raw spectral data with the smoothed periodogram, which gives an inherent width to the peaks in the PSD curve, (ii) the number of periods in the signal, with the width being smaller with larger number of periods, and (iii) the number of frequencies close to one another, due to changes in the rotational pitch of the MT while it moves.

Kinesin-1 driven MT rotation data

A total of 107 kymographs of S-MTs gliding on kinesin-1 motors were analyzed (typical kymograph examples in addition to the one presented in Figure 2.3 are provided in Supp. Figure A2). Only six kymographs needed to be rejected either because 'straightening' the kymographs was inaccurate and/or the combined PSD curve had too many significant side peaks (the same rejection criteria being applied for all following measurements). The pitch of rotation was found to be $8.4 \pm 0.4\,\mu m$

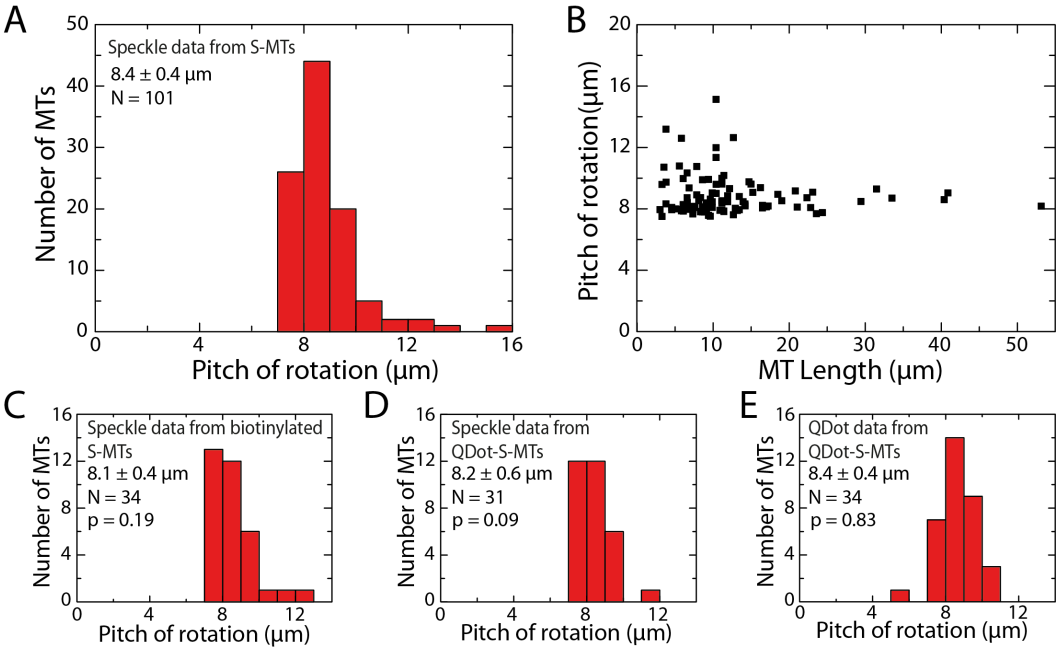

Figure 2.4: Rotational pitch of S-MTs gliding on kinesin-1. (A) Histogram of the rotational pitches of S-MTs. Pitch of rotation is 8.4 ± 0.4 µm (N = 101, where N is the number of MTs), which is in agreement with the supertwist pitch of GMP-CPP MTs. **(B)** Variation in rotational pitch with respect to S-MT length. **(C)** Histogram of rotational pitches of biotinylated S-MTs. Pitch of rotation is 8.1 ± 0.4 µm (N = 34; p = 0.19 with respect to S-MTs, Mann-Whitney U test). **(D)** Histogram of rotational pitches obtained from the speckle signal of QDot labeled S-MTs. Pitch of rotation is 8.2 ± 0.6 µm (N = 31; p = 0.09; p' = 0.56 with respect to biotinylated S-MTs). **(E)** Histogram of rotational pitches obtained from tracking the QDots attached to QDot-S-MTs. Pitch of rotation is 8.5 ± 0.6 µm (N = 34, where N is the number of QDots; p = 0.83).

(N = 101; Figure 2.4A). This value (i) matches previous electron microscopy data which suggested that about 95 % of MTs grown in the presence of GMP-CPP are composed of 14 protofilaments with an inherent left-handed supertwist [17] and (ii) confirms earlier studies that kinesin-1 walks along single MT protofilaments [13, 91]. However, the distribution of the rotational pitches was slightly skewed towards longer pitches. When plotting the rotational pitches of the individual MTs as function of MT length, the longer pitches (>10 µm) could be attributed to short MTs (<12 µm) exclusively (Figure 2.4B). While there was substantial variation in rotational pitches of S-MTs (7-16 µm), the variation in rotational pitch for individual speckles on the same S-MT was always less than 0.2 µm (see Table 2.1). The observations related to rotational pitch distribution are discussed in detail, in the last section in this chapter.

MT Number	Pitch obtained from combined PSD (µm)	Weighted mean of pitches obtained from individual speckles (µm)	Weighted S.D. of pitches obtained from individual speckles (µm)	Number of speckles
1	8.01	8.02	0.07	7(7)
2	8.12	8.13	0.16	7(8)
3	8.08	8.09	0.16	6(6)
4	7.94	7.92	0.01	2(2)
5	7.69	7.68	0.09	7(9)
6	8.01	8.02	0.08	4(5)
7	7.76	7.78	0.13	9(13)
8	8.06	8.04	0.07	7(9)
9	8.08	8.07	0.06	(5)
10	8.16	8.17	0.04	4(4)

Table 2.1: Comparison of results from combined power spectra and individual speckles for ten S-MTs gliding on kinesin-1. Rotational pitch obtained from the combined power spectra does not differ from the weighted mean of the rotational pitches from the individual speckles (weighted by the heights of their peaks obtained in the PSD). The variation of the rotational pitch for individual speckles is less then 0.2 µm, which is much smaller than the variation of the kinesin-1 rotational pitch distribution (~7-15 µm). The last column specifies the number of speckles that showed clear periodicities and the total number of speckles (in brackets).

In order to cross-check our speckle-based approach to the method based on FLIC microscopy on QDot conjugated MTs, biotinylated S-MTs were generated to be conjugated to streptavidin-coated QDots. The rotational pitch of the uncoupled biotinylated S-MTs was found to be 8.1 ± 0.4 µm (N = 34 out of 37 imaged biotinylated S-MTs, Figure 2.4C), not significantly different from the rotational pitch of S-MTs ($p = 0.19$, Mann-Whitney U test). Likewise, the rotational pitches of QDot-S-MTs obtained by speckle analysis (8.2 ± 0.6 µm; N = 31 out of 35 total events; $p = 0.09$ with respect to S-MTs; Figure 2.4D) and QDot tracking (8.5 ± 0.6 µm; n = 34 out of 58, where n is the number of QDots tracked; $p = 0.83$ with respect to S-MTs; Figure 2.4E) did not show any significant differences. These results indicate that QDots have negligible impact on the torsional motion of MTs gliding on kinesin-1 coated surfaces.

2.4 Kip3 motors rotate gliding MTs with short left-handed pitches

To obtain rotational information from S-MT gliding on Kip3-eGFP motors (assay illustrated in Figure 2.5A) the established speckle FLIC approach was used. A total of 86 kymographs were analyzed and 10 were rejected using the same selection criteria used for kymographs of kinesin-1 driven S-MTs. The rotational pitch was significantly shorter than the rotational pitch on kinesin-1 coated surfaces consistent with the earlier results obtained by tracking QDot conjugated MTs (typical example kymograph and evaluation in Figure 2.5B and 2.5C, Supp. Figure A3). The pitch of rotation was found to be $1.4 \pm 0.1\,\mu m$ (Figure 2.5D). Again, when comparing rotation data from uncoupled biotinylated S-MTs with rotation data obtained from QDot-S-MTs negligible differences in the rotational pitches were observed (Figure 2.5E and 2.5F). This indicates that under these experimental conditions there is no advantage of using speckled MTs over QDot conjugated MTs to quantitatively characterize MT rotations.

However, when plotting the QDot intensity as function of traveled distance about 40 % of the intensity peaks exhibited asymmetric profiles (in contrast to the peaks obtained from tracking the speckles, Figure 2.6A). This observation hints towards a hindered motion of the QDots, due to surface interactions (i.e. torsional friction). In particular, the peaks in the QDot intensity profiles show shoulders (indicated by small arrows, Fig 2.6A) that could imply that the QDots get pressed against the surface and that the buildup of sufficient torque is necessary to snap the QDots to the other side of the MTs. At reduced ATP concentration ($10\,\mu M$ instead of $1\,mM$), torsional friction of the QDots appeared to become dominant. Whereas uncoupled biotinylated S-MTs rotated smoothly (see typical kymograph in Fig 2.6B) with a median pitch of $1.0 \pm 0.2\,\mu m$ ($N = 35$ out of 44 imaged B-S-MTs; Fig 2.6C) the QDots obstructed the torsional motion of the QDot conjugated S-MTs with only a few MTs rotating periodically at all. In contrast to the smooth, symmetric and periodic rotations of the biotinylated S-MTs, the intensity profiles of the few QDot-S-MTs that rotated showed variable, often hindered and asymmetric rotations (QDot tracks 1-3 in Fig 2.6D) without any significant reduction in the gliding velocities (gliding velocity of biotinylated S-MTs: $13.6 \pm 4.1\,nm/s$; $N = 41$ and gliding velocity of QDot-S-MTs: $13.2 \pm 1.8\,nm/s$; $N = 21$; $p = 0.85$). These

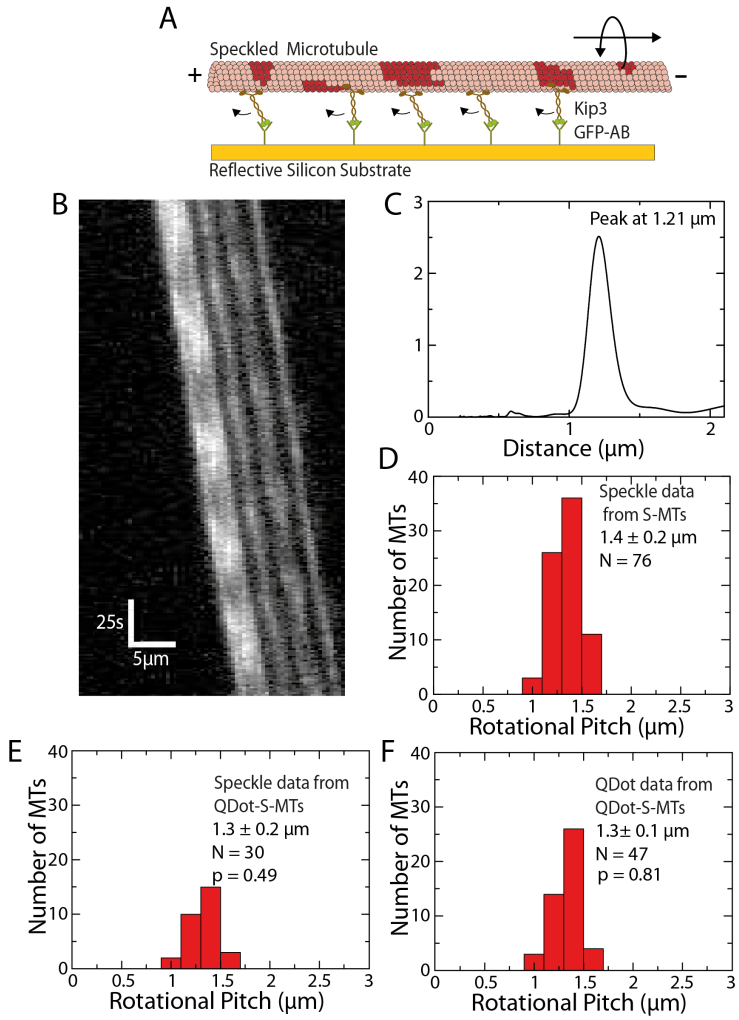

Figure 2.5: Kinesin-8 driven MT rotations. (A) Illustration of S-MTs gliding on a surface coated with Kip3. **(B)** Typical kymograph of a S-MT glding on Kip3. **(C)** Combined PSD curve obtained from five speckles, with peak at about 1.2 μm(data from (B)). **(D)** Histogram of the rotational pitches. Pitch of rotation is 1.4 ± 0.1 μm (N = 76, where N is the number of MTs). **(E)** Histogram of the rotational pitches obtained from the speckle signal of QDot-S-MTs. Pitch of rotation is 1.3 ± 0.1 μm (N = 30; p = 0.49 with respect to S-MTs). (F) Histogram of the rotational pitches obtained from tracking the QDots attached to QDot-S-MTs. Pitch of rotation is 1.4 ± 0.1 μm (N = 48, where N is the number of QDots; p = 0.81).

observations suggest that at low ATP concentrations QDots hinder MT motion in the axial direction and it is beneficial to utilize the impact-free approach provided by speckled MTs.

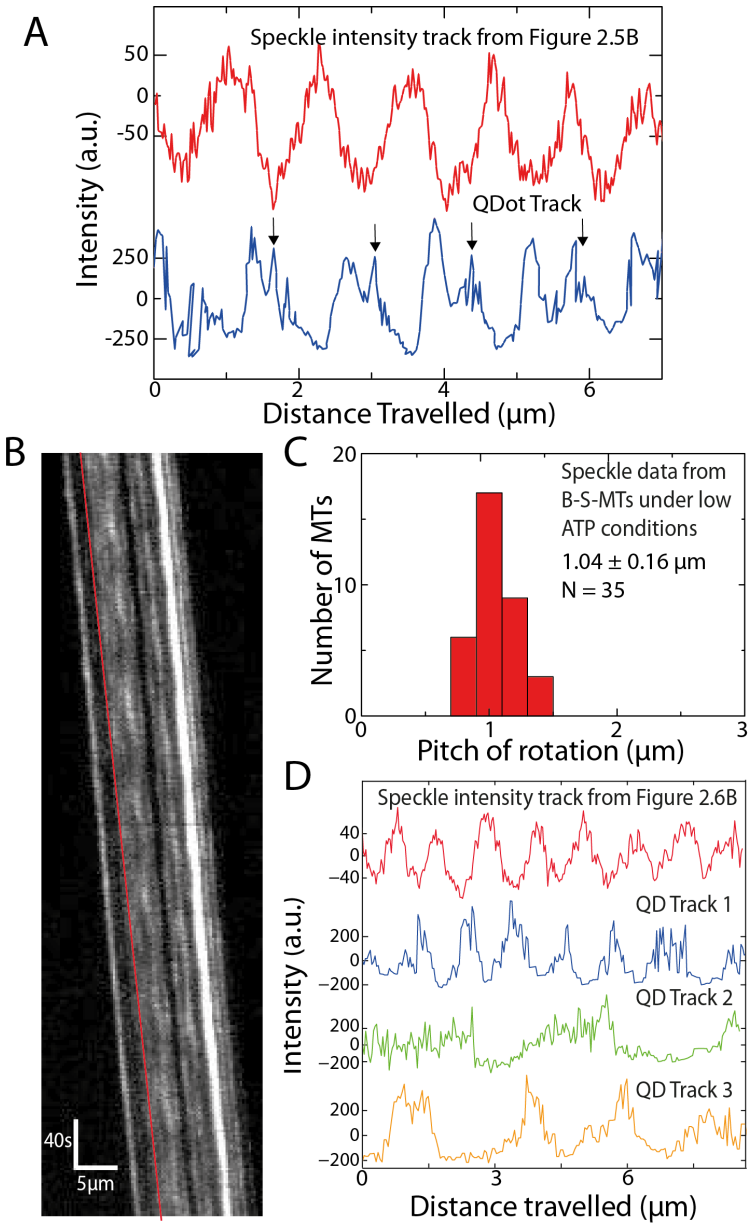

Figure 2.6: S-MTs are superior to QDot-coated MTs in probing rotations of gliding MTs. **(A)** Comparison of a speckle intensity profile from the S-MT shown in Figure 2.5B (red) and the intensity profile of a QDot on a QDot-S-MT (blue). In the speckle intensities of the S-MT, the rotational periods are symmetric and regular, in contrast to the QDot signal, which is asymmetric with regular shoulders (indicated with black arrows), suggesting that the QDot interacts with the glass substrate when it passes between the MT and the surface. **(B)** Typical kymograph of a biotinylated S-MT gliding on Kip3-eGFP in low (10 µM) ATP conditions. **(C)** Histogram of the rotational pitches of biotinylated S-MTs gliding on Kip3-eGFP in 10 µM ATP. Pitch of rotation is 1.0 ± 0.2 µm (N = 35, where N is the number of MTs). **(D)** Intensity profile of the speckle on a biotinylated S-MT indicated by the red line in the kymograph in (B) and three example QDot intensity tracks obtained from QDot-S-MTs gliding on Kip3-eGFP at 10 µM. The FLIC intensity data indicates that the speckle on the uncoupled biotinylated S-MT rotates with a pitch of about 1 µm while the QDots rotate differently: Track 1 (blue) ~1.1 µm, Track 2 (green) ~3 µm, Track 3 (orange) ~ 2.3 µm

2.5 Discussion

In this chapter, an impact-free FLIC-based method was established to analyze the rotational motion of MTs gliding on surfaces coated with kinesins. This method uses non-homogenously distributed fluorescence speckles as optical probes incorporated in the MT lattice. This way, the previous necessity of external, often bulky probes is circumvented and an analysis method with negligible rotational friction on MT rotations is provided. While this method cannot readily be used to determine the handedness of the rotational motion (as it only reports on the height but not the sideward motion of the speckles), this qualitative information can be obtained by performing complementary FLIC microscopy on QDot conjugated MTs. Using this method, the rotational motion of MTs gliding on kinesin-1 and Kip3 motors was probed.

Rotational motion of speckled MTs gliding on kinesin-1

To benchmark the speckle-FLIC method, kinesin-1 driven speckle FLIC gliding assays were performed. In these experiments, a rotational pitch of 8.4 µm was observed (Fig 2.4A), which was higher than the rotational pitch of 14 protofilament GDP-taxol MTs observed in previous works [13, 98]. This implies that 14 protofilament GMP-CPP MTs have a supertwist higher than the supertwist of 14 protofilament GDP-taxol MTs (~6 µm), which has been already suggested in an earlier electron microscopy study of MT lattice structures [17].

Unlike Nitzsche et al. [91] MTs with rotational pitches of about 4 µm (about half the average pitch) were not observed. While occasionally individual speckles with a peak at half of the rotational pitch (presumably due to the collection of two or more speckles in close proximity) were identified, these rare clusters did not significantly influence the combined PSD obtained from multiple speckles per S-MT and thus did not impact the rotational pitch of the S-MT. On the other hand, QDot clusters may yield similar peaks at half the rotational pitch but due to the sparse QDot labeling of the MTs would have a much stronger impact on the measurement.

In Figure 2.4B it can be observed that short MTs (<12 µm) have a higher variation in the measured rotational pitches (up to more than 10 µm for individual S-MTs) than longer ones (Figure 2.4B). This variation may originate from the lower measuring accuracy since only few speckles are available for analysis on short

S-MTs. An additional contribution could come from lattice defects, which may lead to the generation of S-MTs with varying protofilament numbers and reduced growth rates. However, even though one could identify variations in the rotational pitches of different S-MTs, no significant differences in the rotational pitches of different parts of the same S-MT (i.e. no differences in the peak values for different speckles) were observed (Table 2.1). These observations indicate that (i) there was no build-up of torsional tension in the MT lattice and (ii) even if MT lattice defects lead to a different supertwist in small regions of the MT kinesin-1 motors are forced to follow the dominant supertwist of the lattice.

To investigate if the rotational motion of MTs conjugated with QDots is influenced by interactions of the QDots with the surface, rotational data was compared for biotinylated S-MTs gliding on kinesin-1 with or without QDots conjugated to them. No statistically significant difference ($p = 0.56$) in the rotational pitches was observed, suggesting that kinesin-1 motors allow easy passage of QDots between the surface and the MT without significant hindrance of motion. For kinesin-1 gliding motility assays it was measured that the distance between the surface and the MT lattice is about 17 nm [20]. Because the diameter of QDots (~28-34 nm) is larger than this value, to allow the QDots to pass, kinesin-1 motors may stretch (note that kinesin-1 has two hinge domains, which can readily uncoil in gliding motility assays [44]) or detach (note that obstacles trigger the detachment of kinesin-1 motors from the MT [57]).

Rotational motion of speckled MTs gliding on Kip3

In order to explore the rotational motion of MTs gliding on Kip3, gliding motility assay was established for Kip3-eGFP motors. While the gliding motility of MTs was robust, a substantial variation was observed in the gliding velocity (20-50 nm/s, which was strongly correlated to the motor density on the assay surface (Figure 2.1). A possible explanation for this observation is that Kip3 motors, unlike kinesin-1, are not optimized for multi-motor cooperation and individual motor generate frictional force (in an additive manner) to the forward motion of gliding MTs [44, 147].

FLIC microscopy on MTs gliding on Kip3 motors revealed left-handed rotational pitches much shorter than the supertwist of the employed S-MTs (~1-1.5 µm; Figure 2.2 and 2.5). Considering the geometry of the assay, the left-handed rotations correspond to the motor stochastically switching to the leftward protofilament

during forward motion. The structural determinants that enable Kip3 to perform directed left-handed sidesteps is discussed in detail in the next Chapter (see Discussion in Chapter 3).

In contrast to kinesin-1, coupling QDots to MTs gliding on Kip3 influenced their rotational pitch (Figure 2.6). In particular, the QDots appeared to have difficulties to pass between the surface and the MT, often getting momentarily stuck as suggested by the shoulders in Figure 2.6A. This implies, QDots can presumably only pass between the surface and the MT, if sufficient torsional force is generated to force the Kip3 motors to detach. Then, the QDots will snap from one side of the MT to the other, resulting in the asymmetric intensity variations seen in Fig 2.6A. Moreover, at low ATP concentration the QDots coupled to the MT lattice partially suppressed the rotation of the QDot-S-MTs, whereas S-MTs rotated smoothly under the same conditions. This may imply that at low ATP conditions, most Kip3 motors are inactive while the few active motors that drive the MT forward do not generate sufficient torque to overcome the QDot torsional friction due to the inactive motors. Taken together, these results show that the speckle method is superior in quantitatively detecting weak torsional motions of gliding MTs, thereby allowing the exploration of collective properties of molecular motors with a weak and/or stochastic side-stepping behavior.

In summary, the novel speckle-FLIC technique, established in this chapter, is ideal for quantitative characterization of the rotational motion of MTs gliding on Kip3 motors under various experimental conditions. Using this technique revealed that Kip3 motors rotate gliding MTs with short left-handed pitches of ~1-1.5 µm, which would suggest that Kip3 switches protofilaments with a bias towards the left. However, there are some caveats of using multi-motor gliding motility assays to interpret single molecule properties specifically for motors such as Kip3 that are likely not optimized for multi-motor cooperation in cells. It is possible that the observed short left-handed rotations of MTs gliding on Kip3 is just an artifact of the gliding geometry. It is therefore imperative to obtain 3D information of single Kip3 motors directly in stepping assays to confirm and consolidate the observations made in speckle FLIC assays. In the next chapter, a technique to investigate the 3D motion of single motors was established.

Acknowledgements

Kip3 driven MT gliding motility assay protocol was optimized with Dr. Bert Nitzsche and Dr. Felix Ruhnow. The initial Kip3 gliding motility assay experiments using QDot conjugated MTs were performed with Dr. Bert Nitzsche. The MATLAB script to analyze the rotational data from speckled MTs was written by Dr. Felix Ruhnow.

CHAPTER 3

3D motility of single Kip3 motors

Knowledge about the 3D stepping of kinesins on the surface of MTs can be inferred by directly imaging them on freely suspended MTs. In this chapter, an in vitro stepping assay is established where it is possible to perform 3D tracking of single Kip3 motors, coupled to QDots, moving along MTs freely suspended on a polymer patterned glass surface. 3D tracking microscopy is performed using Parallax [148], a dual-focus imaging technique. 3D trajectories of single Kip3 motors reveals that the motors have a helical trajectory around the MT lattice with a pitch of ~2 µm. This indicates that during forward motion Kip3 motors switch stochastically in a biased manner to the leftward protofilament. It is hypothesized that the protofilament switching may be due to Kip3 having (i) a flexible neck and (ii) a necklinker longer than kinesin-1.

The model presented in this chapter has been published in Bormuth et al. [92]

Multi-motor gliding rotation assays provided indirect proof regarding the trajectory of single Kip3 motors (see Chapter 2). To confirm the observations made in gliding assays it is essential to obtain 3D trajectories of single Kip3 motors. However, there is a number of challenges in performing 3D stepping assays with Kip3.

- The Kip3 motors are labeled with eGFP tags, which have a localization precision of ~30 nm for 100 ms acquisition time even at good imaging conditions, using TIRF microscopy, at relatively high laser power [149]. This suggest that though the eGFP tag enable observation of linear motility of Kip3 motors along the MT, they are not bright enough to study the 2D motion along the MT lattice having a width of 25 nm. Further, eGFP fluorescence lifetime is relatively short (in the order of seconds) which makes it impossible to obtain long traces of individual motors. Therefore, one would need an efficient strategy to conjugate single motors to brighter photo-stable probes in order to obtain 2D (or 3D) information of motors stepping along MTs.
- In conventional stepping assays, MTs are immobilized on the surface. This allows Kip3 motors access to only a part of the MT lattice, which is not in contact with the surface. Also, Kip3 motors would interact with the surface, which may hinder their motility (depends strongly on the surface preparation). Therefore, one would need a strategy to suspend the MTs in order to allow the stepping Kip3 motors free access to the entire MT lattice.
- 3-D imaging with a reasonably good z-resolution is another issue to be considered. In gliding assays, FLIC microscopy was used to obtain z-information along with 2D imaging. However, it is not possible to perform TIRF imaging, necessary to minimize background in single molecule assays, using FLIC microscopy. Therefore, one would need to develop an alternative strategy for 3D imaging where TIRF microscopy is a possibility.

The issues were resolved by (i) coupling Kip3 motors with QDots; (ii) patterning the glass substrate with transparent polymer ridges and immobilizing the MT ends to the ridges; (iii) using parallax [148], a dual-focus imaging technique that provides nanometer information in z-direction, in conjunction with 2D tracking of the QDot-Kip3 conjugates. The basic experimental strategy is illustrated in Figure 3.1. In the following sections the details of the setup are explained.

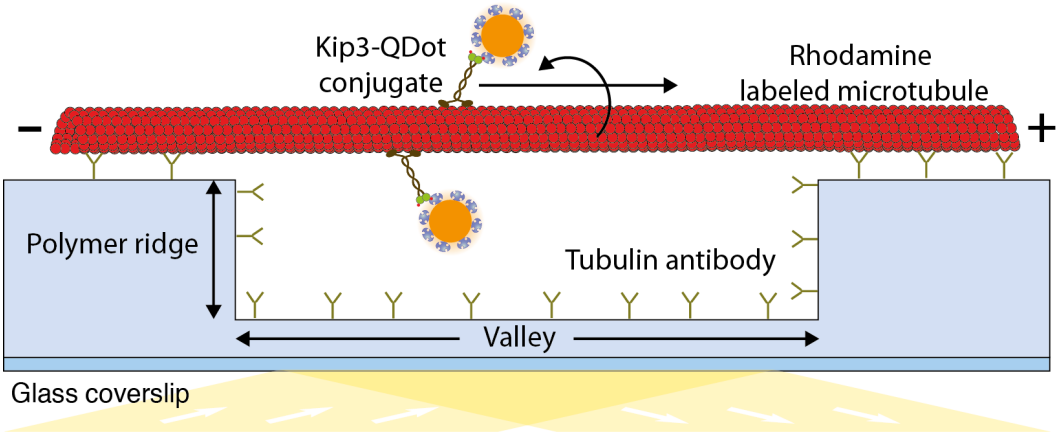

Figure 3.1: Schematics of a 3D stepping motility assay. Freely hanging MTs are attached to the surface via their ends by anti-β tubulin antibodies. The Kip3 motors, linked with QDots, are capable of accessing the entire 3D lattice of the MT at the valley between two parallel ridges.

3.1 Conjugation of QDots to Kip3 motors

As explained earlier, the eGFP tags on Kip3 are insufficiently bright and have a relatively short fluorescence lifetime. It is therefore necessary to conjugate Kip3 motors to probes with better photochemical properties. For this purpose, a Kip3 construct was prepared, that was labeled with a multifunctional GFP tag (hereafter referred to as Kip3-mfGFP or Kip3) which comprised of a streptavidin binding peptide (SBP) inserted within the GFP sequence [150], as illustrated in Figure 3.1. The SBP tag protrudes out of the barrel shaped GFP structure near the C-terminal end (further away from the Kip3 tail) and binds specifically to streptavidin. Any optical probe coated with streptavidin molecules can thus be conjugated to Kip3 motors. The Kip3-mfGFP construct was expressed in insect cells and purified using His-affinity chromatography.

In order to confirm whether the Kip3-mfGFP construct was functional and the addition of the mfGFP tag at the C-terminal of the full-length Kip3 motor does not alter motor function conventional *in vitro* stepping assays were performed (Figure 3.2B). The interaction of single Kip3-mfGFP motors with MTs immobilized to the surface via anti-β-tubulin antibodies was observed using TIRF microscopy, as shown in the kymograph (Figure 3.2B). The Kip3 motors were motile and moved with a velocity of 49.1 ± 1.0 nm/s (N = 344), similar to velocities observed in previous works [34, 95]. Also, the Kip3 motors depolymerized GMP-CPP MTs

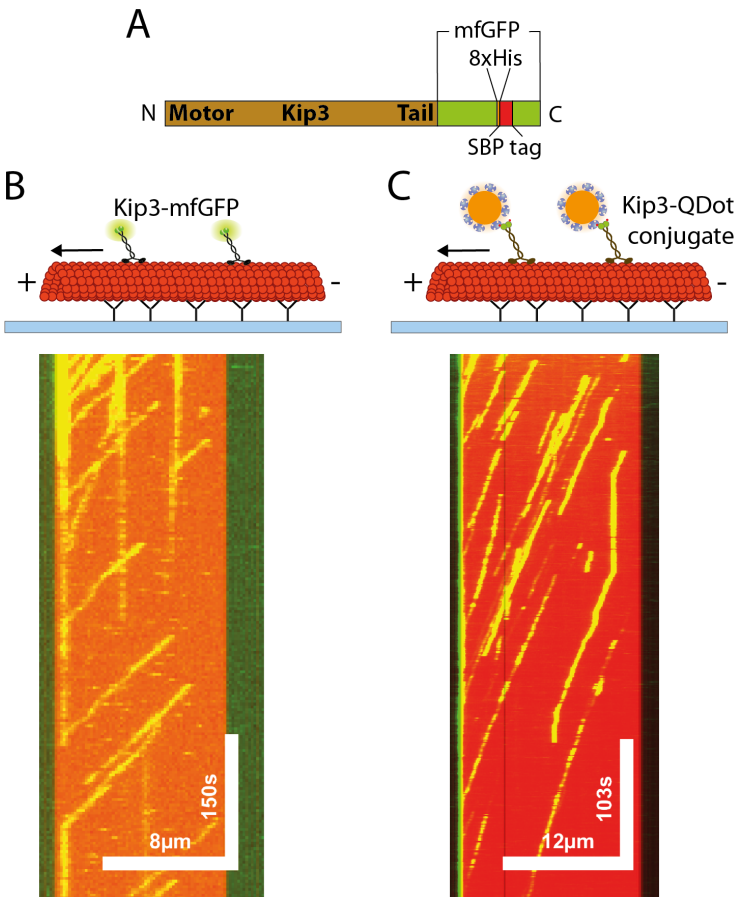

Figure 3.2: Kip3-mfGFP motors are functional and can be conjugated to QDots. **(A)** Illustration of the protein sequence for Kip3-mfGFP with the 8xHis tag and the streptavidin binding peptide (SBP) tag inserted in the multifunctional GFP (mfGFP). **(B)** A typical kymograph of single Kip3-mfGFP motors (in green) moving along a MT (in red). Similar to literature, the stepping velocity of Kip3 motors was 49.1 ± 1.0 nm/s (N=344). **(C)** A typical kymograph of Kip3-mfGFP motors conjugated to QDots (in green) moving along a MT (in red). The stepping velocity of Kip3-QDot conjugates was 49.1 ± 3.0 nm/s (N = 80)

(data not shown) as shown in previous literature [34, 95, 127] suggesting that the motors are fully functional.

QDots (same as the QDot655 streptavidin conjugate used in gliding rotation assays) were utilized as probes for better imaging. As discussed in the previous chapter, QDots as not ideal optical probes as they blink and are susceptible to chemical quenching. The blinking and the chemical quenching depend significantly upon the amount of free radicals in the used media (it is imperative to have DTT or BME in the buffer) and vary from probe to probe leading every QDot probe to have a slightly different fluorescence signature. Despite the above-mentioned limitations, the high fluorescence lifetime (three orders of magnitude higher than GFP) and high extinction coefficients (one to two orders of magnitude higher than for GFP) make QDots good optical probes for 3-D imaging for long durations with reasonably high resolution.

Kip3-mfGFP motors were conjugated to the QDots via their SBP tags. SBP

binds to homotetrameric streptavidin molecules by simultaneously interacting with biotin-binding pockets from two separate streptavidin subunits [151]. The dissociation constant for the SBP-streptavidin interaction is in the nanomolar range (K_d is ~2.5 nM [152]) which indicates reasonably high affinity interaction but still much weaker than the biotin-streptavidin interaction (K_d is in the femtomolar range). However, since the QDots are coated with 5 to 10 streptavidin molecules and the Kip3-mfGFP motors are dimers, if the two SBP tags on a single Kip3-mfGFP motor binds to two of the streptavidin molecules coated on the same QDot molecule, the dissociation constant of the Kip3-Qdot interaction would be in the 10^{-17} M range which indicates extremely high affinity binding.

For coupling Kip3-mfGFP motors with the QDots, Kip3 motors were incubated with QDots in 1:10 stoichiometric ratio. Conventional *in vitro* stepping assays were performed and the QDot signal from the Kip3-QDot conjugates was observed, as shown in the example kymograph (Figure 3.2C). The observed velocity obtained after tracking the QDot signal was 49.1 ± 3.0 nm/s ($N = 80$).

Single molecule conditions was obtained for the Kip3-QDot conjugates

In single molecule studies that involve attaching motors to artificial cargoes like QDots, gold nanoparticles or glass beads, it is essential to prove that only one motor is attached to the probe. Here, one Kip3 motor per QDot was confirmed by: (i) considering the incubation stoichiometry of the motors and the cargo; (ii) direct observation of the number of motors attached to the cargo; (iii) comparing the motility parameters of the cargo linked motor with single motors.

- It has been shown previously that binding of motors to cargoes follow Poisson statistics [62]. For the Kip3-QDot interactions to follow Poisson statistics certain criterions are assumed: (i) Kip3 motors (and QDots) function independently and there are no motor clusters (and QDot clusters). (ii) There is no free streptavidin in the solution and all the Kip3 motors bind to the QDots. The probability that a QDot carries no Kip3 motors ($P_0 = e^{-x}$; x is the average number of Kip3 motors), one Kip3 motor ($P_1 = xe^{-x}$) or two (or more) Kip3 motors (P_2 or more = 1 - e^{-x} - xe^{-x}) with respect to the stoichiometric ratio of the number of Kip3 motors per QDot is plotted in Figure 4.3A. In the experiments performed in this study, Kip3 motors were incubated with QDots at approximately 1:10 stoichiometric ratio (region

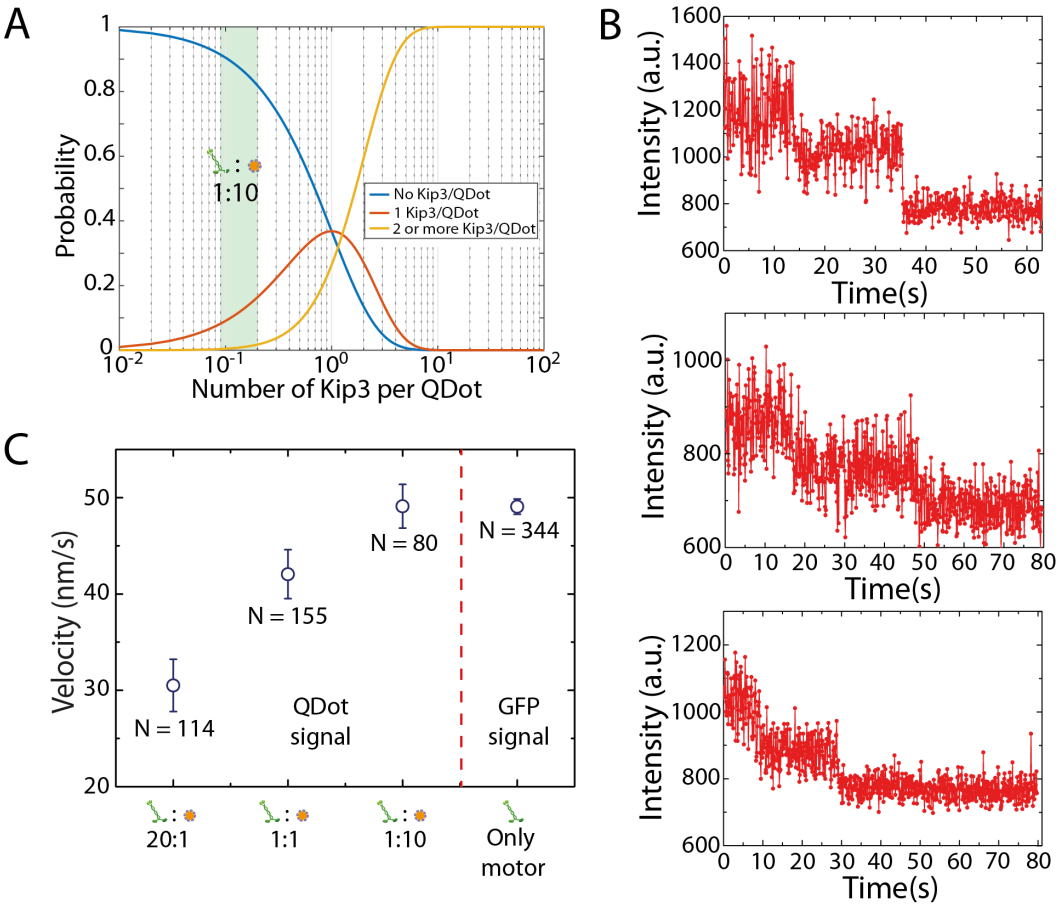

Figure 3.3: Single molecule conditions obtained for the Kip3-QDot conjugates. (A) The probability of Qdots to be coupled to no Kip3, one Kip3 and two (or more) Kip3 according to Poisson statistics is plotted versus the stoichiometric ratio at which the Kip3 motors were incubated with QDots. ~95 % of the Kip3-QDot conjugates have only one Kip3 motor at 1:10 Kip3:QDot stoichiometric ratio (shaded in green). **(B)** The Kip3-QDot conjugates were bound stationarily to MTs using AMP-PNP (non hydrolysable analog of ATP) in stepping assays. The GFP signals corresponding to majority of the Kip3-QDot conjugates (~96 %; N=45) showed 2-step photobleaching (or less) characteristic of a single Kip3 dimer as shown in the three examples. **(C)** Stepping velocity of Kip3-QDot conjugates at 20:1 (30.5 ± 3.0 nm/s; N=115), 1:1 (42.1 ± 3.0 nm/s; N=155) Kip3:QDot stoichiometric ratio is much lower than single molecule velocity (49.1 ± 1.0 nm/s; N=344). However at 1:10 (49.1 ± 3.0 nm/s; N=80) Kip3:QDot stoichiometric ratio the Kip3-QDot velocity is not significantly different from single molecule velocity (p=0.9, Mann-Whitney U test).

marked in green in Figure 4.3A). If the assumptions hold true, all the Kip3 are bound to QDots and there is a 90-97 % certainty that there is only one Kip3 per QDot-Kip3 conjugate.

- For direct observation of the number of Kip3 attached to individual QDots the GFP signal of Kip3-QDot conjugates was observed in stepping assays performed in *adenylyl-imidodiphosphate* (AMP-PNP). 45 events were observed and the GFP signal corresponding to 96 % (see examples in Figure 4.3B) of the Kip3-QDot conjugates showed 2-step (or less) photobleaching while only 4 % (2 events) showed 3-step (or more) photobleaching.

- The velocity of non-conjugated Kip3 motors (49.1 ± 1.0 nm/s; N=344) was compared with Kip3-QDot conjugates incubated at 20:1 Kip3:QDot stoichiometric ratio (30.5 ± 3.0 nm/s; N=115) and 1:1 Kip3:QDot stoichiometric ratio (42.1 ± 3.0 nm/s; N=155) and it was observed that the Kip-QDots are significantly slower (possibly due to multi-motor effects). However, at 1:10 Kip3:QDot stoichiometric ratio the Kip3-QDot velocities (49.1 ± 3.0 nm/s; N=80; p=0.9, Mann-Whitney U test) were similar to the velocities of non-conjugated motors (Figure 3.3C). This confirms that incubation at Kip3:QDot stoichiometric ratio of 1:10 most Kip3-QDot conjugates have single Kip3 motor attached to them.

3.2 MTs can be freely suspended on polymer ridges structured on glass

In conventional *in vitro* stepping assays, the MTs are rigidly bound to the surface. The kinesin motors can access only a part of the MT lattice. Further, the motors are likely to encounter hindering surface interactions that alter the normal trajectory of the motor. This can be avoided by immobilizing the distal parts of the MTs on an elevated surface such that the proximal part of the MT is freely suspended and has no surface interaction. In two previous studies, such geometries are achieved by fixing the ends of the MTs to large beads (coated with anti-tubulin antibodies) either bound to the surface [97] or held in solution by optical traps [98]. In other studies the surface was structured with elevated parallel ridges such that filaments bound to the ridges were freely hanging in the valleys in between the ridges

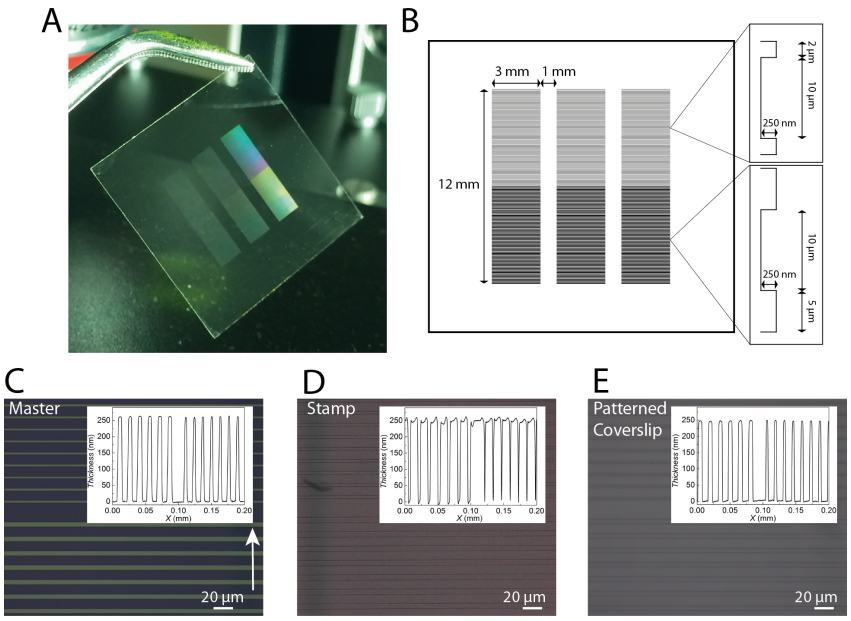

Figure 3.4: Polymer ridges structured on glass using UV Nanoimprint Lithography (UV-NIL). (A, B) Glass coverslips were patterned with polymer resin using UV Nanoimprint lithograghy (UV-NIL) as described in the Experimental Methods. As seen in the illustration **(A)** and picture **(B)**, the pattern imprinted on the glass coverslips had two different regions characterized by relief lines (that form the ridges) with a height of about 250 nm and a width respectively of 2 µm and 5 µm, separated by 10 µm (the valleys between the ridges). The ridges on the patterned coverslip **(E)** reproduce the initial master structure (**C**; intermediate stamp profile in **D**) and have a smooth, blunt profile as seen in the profilometer height analysis (**E** inset). Insets: Step height analysis obtained from profilometer measurement (X scan direction).

[96, 105]. Such an assay provides us greater throughput than the bead assays and is much less complicated than the optical trap held bead assay.

Here, glass coverslips were patterned with a transparent polymer using UV Nanoimprint lithography (UV-NIL). As seen in picture (Figure 3.4A) and the illustration (Figure 3.4B), the pattern imprinted on the glass coverslips had two different regions characterized by relief lines (that form the ridges) with a height of about 250 nm and a width respectively of 2.5 µm and 5 µm, separated by 10 µm (the valleys between the ridges). The ridges reproduce the intial master structure (Figure 3.4C; intermediate stamp profile in Figure 3.4D) and have a smooth, blunt profile as seen in the profilometer height analysis (Figure 3.4E). Due to the blunt profile, MTs were often not suspended in a taut manner, but slacked in the middle. It is therefore necessary to have 250 nm high ridges (100 nm ridges were found to be too shallow with majority of the MTs touching the valley surface) for double stabilized MTs so that the MTs do not interact with the valley surface (the

height needs to be even more for GTP grown Taxol stabilized MTs which have a persistence length 3 times less than the double stabilized MTs [153]). Further, the slacking of MTs in the middle was even more significant for MTs not bound rigidly to the ridges. Therefore, the ridges were 2.5 µm (5 µm) wide and excess of anti-tubulin antibodies were applied (in comparison to the amount used in conventional stepping assay) to ensure ample attachment points for MTs. The polymer patterned on the coverslips has a refractive index similar to glass (ideally it should be close to the refractive index of water) and has some autofluorescence signal that was bleached before imaging the QDot signal in order to minimize the background noise. Therefore, taking the above considerations into account, it was possible to freely suspend MTs on the polymer structured glass surface.

3.3 3D tracking of QDots using Parallax microscopy

In order to perform 3D tracking microscopy on Kip3-QDots stepping along suspended MTs, a dual-focus imaging technique, Parallax, was established. In the Parallax set up (adapted from Sun et al. [148]), the beam path was split at the Fourier plane (a plane conjugate to the objective back focal plane) and both the split images were acquired simultaneously. A schematic illustration of the Parallax set-up can be seen in Figure 3.5A. Here, a commercially available D-shaped mirror was used to split the image beam path. A lens (f = 150 mm; L1) was placed one focal length away from the image plane, which collimates the beam flux coming from the image. The beam flux was then split using a sharp-edged D-shaped mirror (D1) that was positioned such that half the beam could pass through while the other half gets reflected. Both the beams were guided to the camera chip (referred to as new image plane) using mirrors (R1, R2 and D2) and focusing lens (L2 and L3; f = 200 mm) to form the two split images. The two split images were recorded simultaneously on the upper and lower halves of the camera chip. In this set-up, when an optical probe moves only in the xy plane, both the acquired split images move the same amount in the x and y directions. However, when the probe moves out of focus in the z-direction, the acquired split images move towards or away from each other in the y direction (as seen for an example 100 nm Tetraspeck bead in Figure 3.5B).

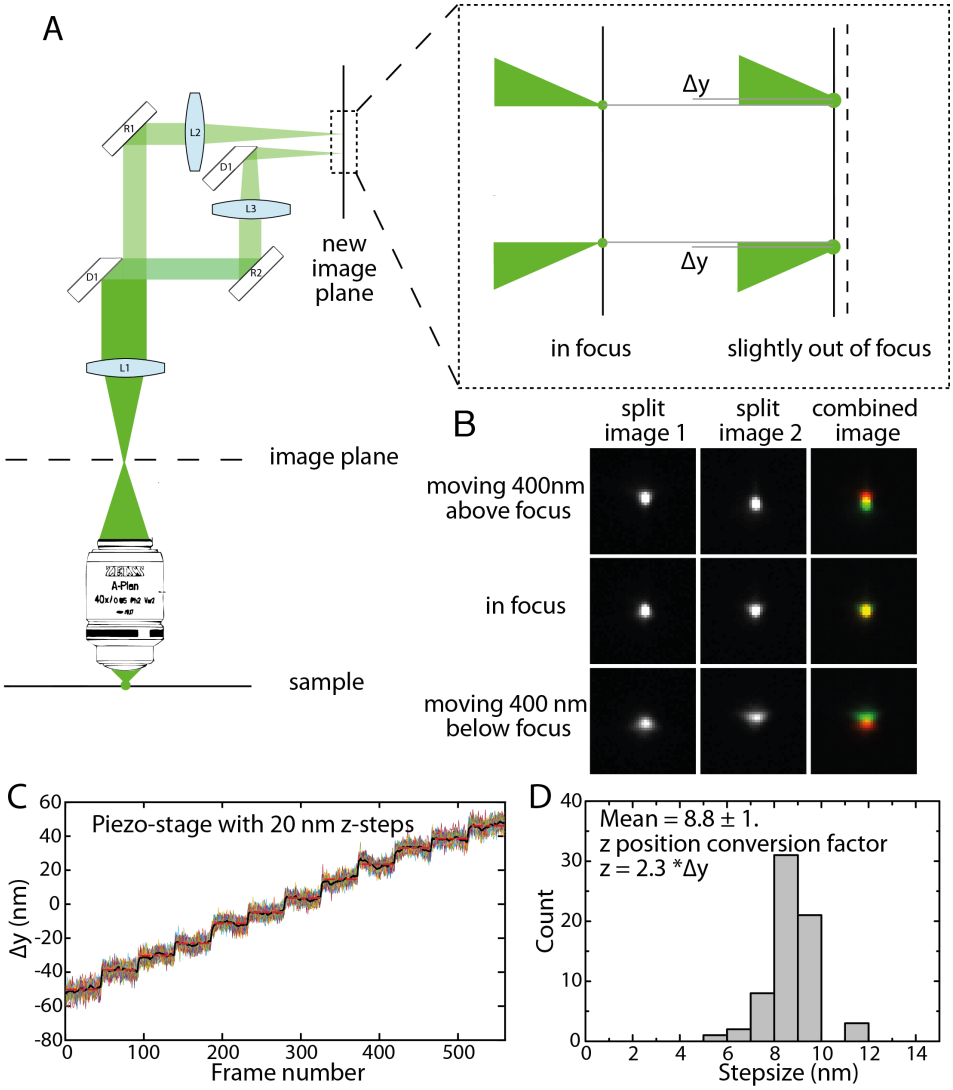

Figure 3.5: Details of the Parallax setup. (A) A schematic illustration of the Parallax setup. A lens L1 placed one focal length away from the image collimates the emission signal from sample. This collimated beam is split by a D-shaped mirror D1 placed at the back focal plane. The two split beams are directed by reflectors R1, R2 and D1 and focused onto different parts of the same camera chip using image focusing lens L2 and L3. When sample moves slightly out of focus, the split images shift relative to each other (inset). **(B)** A 100 nm Tetraspeck bead imaged using Parallax. When the bead is in focus the two split images overlay on each other, as seen in the combined image. On moving the bead 400 nm above (below focus), the split images move towards (away) each other. **(C)** Tetraspeck beads immobilized to a glass coverslip were imaged at 10 fps using Parallax while moving the stage along the z-axis by 20 nm steps every 5 s. The Δy for 49 bead tracks in plotted with respect to image frame number. The mean Δy of all the tracks is plotted in black and the average of the mean Δy over 50 frames (corresponding to one z-step) is indicated in red. **(D)** Probability histogram plotted for the Δy stepsize. The mean Δy step-size is 8.8 ± 2.0 nm (mean $\pm$ S.D.). Assuming a linear response of Δy to z shift, the z position conversion factor is 2.3.

In order to obtain the 3D co-ordinates of the optical probes, acquired image streams were analyzed using FIESTA [145] where every frame was split laterally into two halves (corresponding to the two split images created by the Parallax setup) to create separate image channels. The track co-ordinates for each optical probe was obtained in the two split channels. The x and y coordinates for the final 3D track corresponding to an optical probe was calculated by averaging the x and y co-ordinates (absolute) of the track in the two split channels while the z coordinates was obtained from the relative difference in the y coordinates (Δy) multiplied by a certain z position conversion factor. To calculate the conversion factor, Tetraspeck beads (attached unspecifically to a glass surface; N = 49) were imaged using Parallax at 10 fps over a Piezo-stage (Mad City Labs Inc., Madison, USA) moved in the z direction by 20nm steps every 5 s (see tracked data in Figure 3.5C). Assuming a linear response of Δy to z-shift, a mean step-size of 8.8 ± 2.0 nm corresponding to the 20 nm steps provided a z position conversion factor of 2.3 (Figure 3.5D). Therefore, the Parallax set-up was established for 3D tracking microscopy experiments.

3.4 Single Kip3 motors have a left-handed helical path around freely suspended MTs

Having resolved the issues regarding (i) coupling Kip3 motors with QDots, (ii) freely suspending MTs and (iii) 3D imaging, it was possible to obtain 3D trajectories for single Kip3 motors. In the following section, first, the localization error in tracking Kip3-QDots in the established set-up has been determined. Second, the imaging acquisition and analysis approach has been described. Finally, the results obtained from tracking Kip3-QDot motility events have been discussed.

Localization error of the experimental setup

The localization error was quantified by determining the standard deviation of the central position of the QDots (imaged over 1000 frames and tracked using FIESTA) that were coupled with Kip3 motors stationarily bound (using AMP-PNP) to MTs suspended on polymer-patterned coverslips. The calculated localization error of the set-up was ~10-15 nm (x error = 13 ± 8 nm; y error = 10 ± 14 nm; z error = 13 ± 18 nm; N = 73). Considering the distance between adjacent protofilaments

is ~6 nm [92] the localization error is rather high to observe individual sidesteps in Kip3 motility tracks. The high localization error in the 3D stepping assays is due to a number of reasons. (i) In Parallax, the image beam is split into half and there are additional reflectors the beams pass through (a percentage of photons get absorbed). The total number of photons collected eventually at the camera chip is considerably lower (less than half) than for a conventional set-up. (ii) The polymer patterned on the glass coverslip absorbs some photons. Further, auto-fluorescence signal from the polymer reduce the SNR. (iii) Since the ridges are 250 nm high HILO (highly inclined thin illumination [154]) imaging was performed instead of TIRF which led to increased background signal due to the free QDots in solution. (iv) The QDots are conjugated to the tails of Kip3 motors with linkage having some compliance. Indeed, in Varga et al. [95] the localization error of QDots attached to Kip3 motor heads (lower positional fluctuations than QDots attached to Kip3 tails) imaged on normal glass, using TIRF microscopy, was found to be only marginally better (~10 nm). This indicates that the positional fluctuation of the QDot linked to Kip3 tail is the main contribution to the high localization error. Further, the high error for the calculated localization errors indicate that there is high variance between individual QDots and QDot probes with very low photon count were ignored while analyzing Kip3-QDot events. Considering the dimensions, the width of a MT is ~25 nm, the diameter of a QDot is 31 ± 3 nm and the estimated height of a Kip3 motor stepping along a MT, attached to a QDot via its tail, is in the 0-20 nm range. This implies that the axial distance traversed by the QDot center when a Kip3-QDot conjugate moves from extreme left to extreme right of a MT is 55-95 nm (Figure 3.6). This is the lower limit of localization accuracy essential to detect full rotations of single Kip3-QDot conjugates around the MT longitudinal axis. The localization error of the set-up is sufficiently low (~10-15 nm) to detect significant motion of Kip3-QDots along the transverse axis of MTs.

Criteria for image acquisition and analysis of Kip3-QDot motility events

The 3-D stepping assays for Kip3-QDot conjugates were performed as described in the Methods section (page 104). MTs and reference beads (200 nm Tetraspeck beads) were immobilized on the polymer-patterned coverslips and the split images were observed simultaneously on two halves of the same camera chip. A field of view

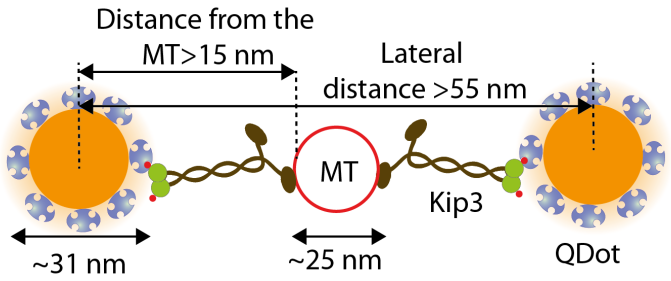

Figure 3.6: Axial dimensions of the path traversed by Kip3-QDot around a MT. The diameter for the helical path traversed by the Kip3-QDot (QDot centre localized by tracking the QDot signal) around the MT is greater than 55 nm.

was selected when there were 3 (or more) reference beads bound to the surface and numerous MTs suspended between ridges. The MTs were imaged for 100 frames (5 fps) in order to eliminate evaluation of Kip3-QDot events on swiveling MTs or MTs touching the valley surface (interpreted qualitatively from the difference in the MT profile in the two split images). The region was then exposed to 488 nm laser light (excitation light used later for imaging the QDots) for 1-2 min to bleach the background autofluorescence signal from the polymer-pattern. Afterwards, the Kip3-QDot mixture was flushed in and image acquisition (3-5 fps) was started after 1 min in order to record Kip3-QDot motility events.

The acquired image stream of the Kip3-QDot stepping assay was analyzed using FIESTA [145] where every frame was split laterally into two halves (corresponding to the two split images created by the Parallax setup) to create separate image channels. Since the split beam paths cannot be projected exactly onto the two halves of the camera chip (due to limitations in the alignment of the optical elements), a translational and rotational offset between the two channels is obtained by the reference beads (minimum 3 reference points necessary). Stage drift during imaging was corrected with the averaged position of the reference beads (in 3D). Each Kip3-QDot event was tracked in the two channels and co-ordinates were obtained after offset and drift correction (see workflow in Figure3.7).

The 3D Kip3-QDot track data was fitted to a spline (a spline is a piecewise cubic curve bent to pass through a number of predefined points referred to as 'knots') using non-linear least-squares fitting. 4 knots were placed along the QDot-Kip3 track that includes the start and end point of the track and 2 additional roughly equidistant points (to each other as well as to the start and end points) along the track (the number of knots can be reduced or increased to account for the flexibility

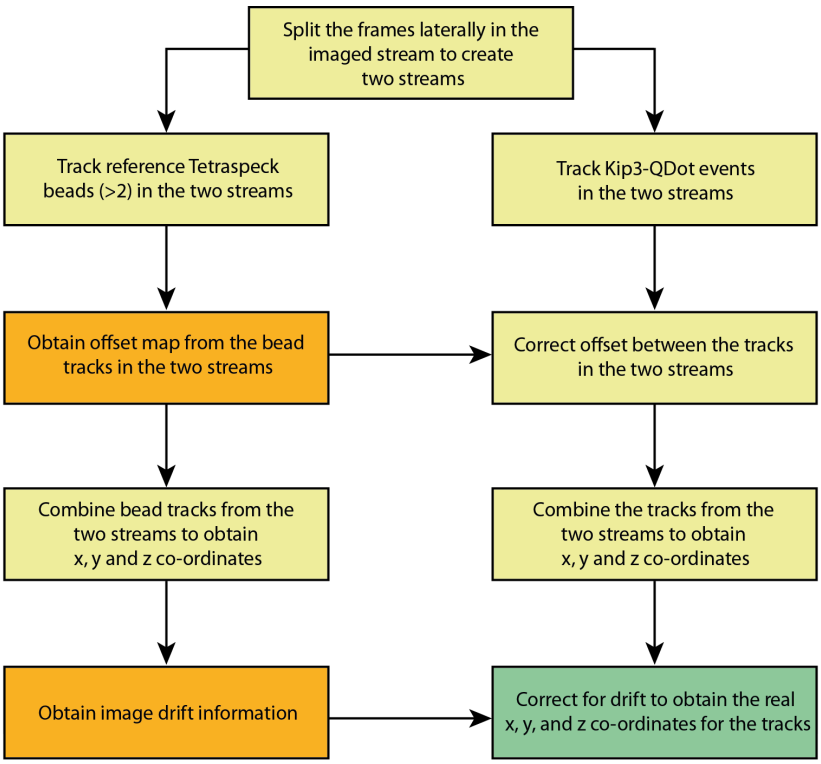

Figure 3.7: Workflow to obtain the 3D co-ordinates of the tracks for Kip3-QDot motility events imaged using Parallax.

of the MT). The x-position of the first and last knots were kept constant (since the maximum displacement is always along the x-axis), while all other positions were varied to find the optimal path with least square fitting. The x-position of the inner knots was restricted within the x-position of the start and end points. A cubic spline along the knots was interpolated in all three dimensions and the minimum distance to the spline was calculated. In addition, instead of using a regular spline, a tube around the spline with a radius of 12.5 nm was used to account for the MT width. Minimum distance of each tracked data point from the surface of the fitted tube was calculated by subtracting 12.5 nm from the minimum distance to the spline and because negative values denote points within the tube they were replaced with their absolute values multiplied by 5 (as a penalty to make their contribution less significant when optimizing the fitted path). The points of the track were then projected on the optimized path and the angle of the Kip3-QDot to the path was extracted by calculating the angle between the projection vector (the vector from the path to each data point with the shortest distance) and the tangent vector (the vector for each projection point in the direction of the spline).

A large number of the acquired 3D tracks of Kip3-QDot motility events were eliminated from further analysis based on the following criteria.

- Tracks smaller than 3000 nm were ignored.
- Tracks on fluctuating MTs or MTs interacting with the valley surface were ignored. Such MTs were identified by imaging the MTs before adding the Kip3-QDot conjugates and detecting floppy swiveling MTs (occurs if the MTs are not rigidly bound to the ridges) or MTs having a weird profile (probably due to interaction with the valley surface).
- Tracks with very large displacements (>500 nm between frames) possibly obtained on MTs that got displaced while imaging the QDot signal were also eliminated.
- Tracks with large and/or frequent gaps were also ignored. Such tracks were obtained for Kip3-QDot conjugates having one or more of the following issues; (i) poor signal-to-noise ratio, (ii) blinking very frequently, (iii) too close to reference beads and/or (iv) too close to other Kip3-QDot conjugates.

Single Kip3 motor proteins undergo left-handed helical motion

The 3D stepping assays were performed as described above. In the example Kip3-QDot motility event in Figure 3.8A (see further example tracks in Figure S4), it is observed that Kip3-QDot does not move linearly along the fitted tube (representing the MT) but takes a left-handed helical trajectory around the longitudinal axis of the tube. The mean distance of the tracked data points from the surface of the fitted tube is 24 ± 17 nm (mean $\pm$ S.D.), which is within the range estimated earlier. In order to obtain the rotational pitch of the track, the angular information for the Kip3-QDot event was plotted against the distance travelled (see Figure 3.8B, S4). The maxima (or minima) were selected by hand and the corresponding rotational pitch and end-to-end velocity were recorded. Automatic analysis approaches to obtain the rotational pitch were not employed since the rotational pitch for the single molecule events were not completely uniform but showed some expected stochastic variance. The cumulative angle was acquired after smoothening the data (rolling frame average over 10 consecutive frames) and plotted against the distance travelled to provide the handedness of rotation (see Figure 3.8C; angles

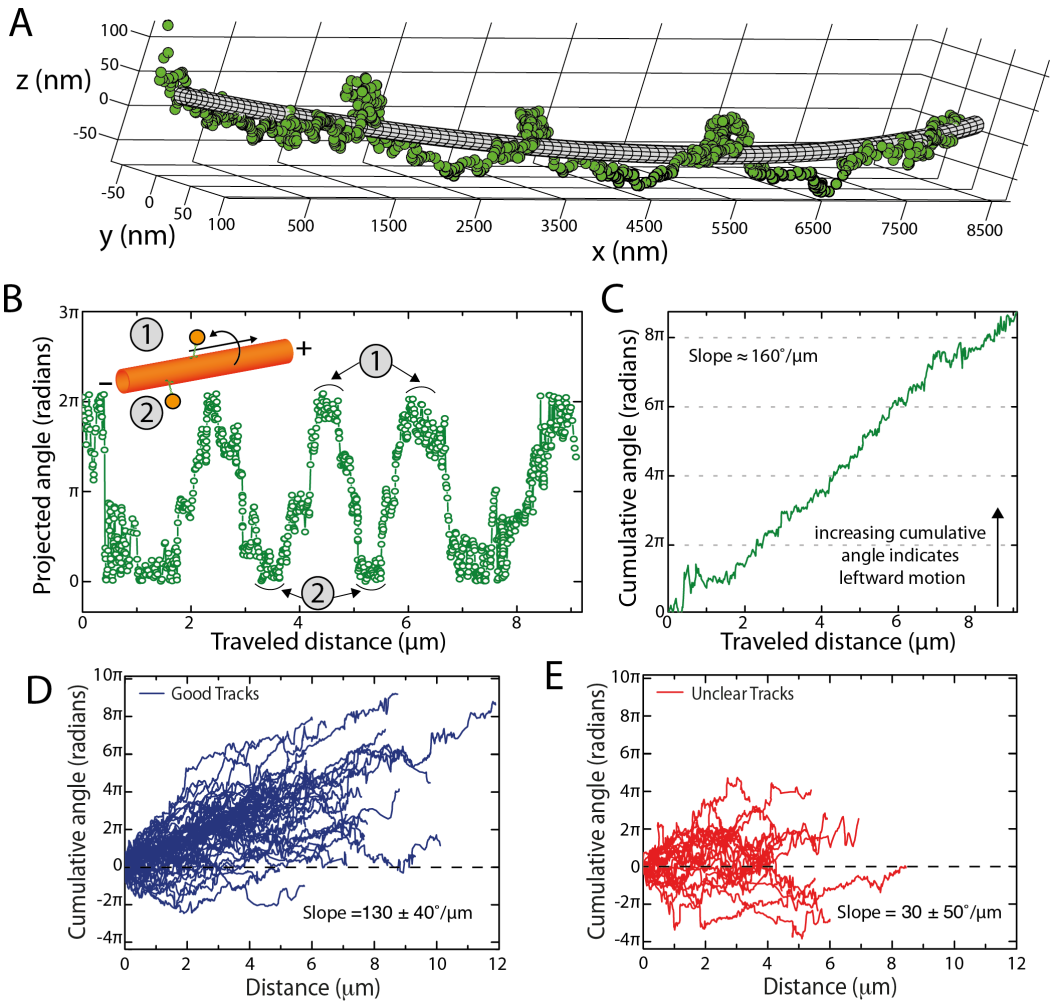

Figure 3.8: Single Kip3 motor proteins rotate around freely suspended MTs. (A) The 3D tracking results for an example Kip3-QDot event is fitted to a 25nm wide tube using non-linear least-squares fitting. **(B)** The projected angle of the Kip3-QDot with respect to the MT lattice is shown for every position along the MT axis (travelled distance). Here, the maxima (minima) denotes the position of Kip3-QDot on top (bottom) of the MT lattice. **(C)** The increase of the cumulative angle with increasing travelled distance indicates the directionality of rotation, with positive values denoting angular changes towards the left (in the direction of motion). The example Kip3-QDot moves around the MT with an average velocity of 43 ± 1 nm/s and has a rotational pitch of 2.1 ± 0.3 μm (both mean ± S.D., n=3). **(D)** The cumulative angle for all the 53 events that showed clear rotations is plotted versus the linear distance travelled. All the events show left-handed rotation around the fitted tube in the direction of motion with a slope of 130 ± 40 °/μm. **(E)** The cumulative angle for all the 23 unclear events plotted versus the distance travelled. The unclear events also have a leftward bias, though less pronounced (slope $= 30 \pm 50$ °/μm).

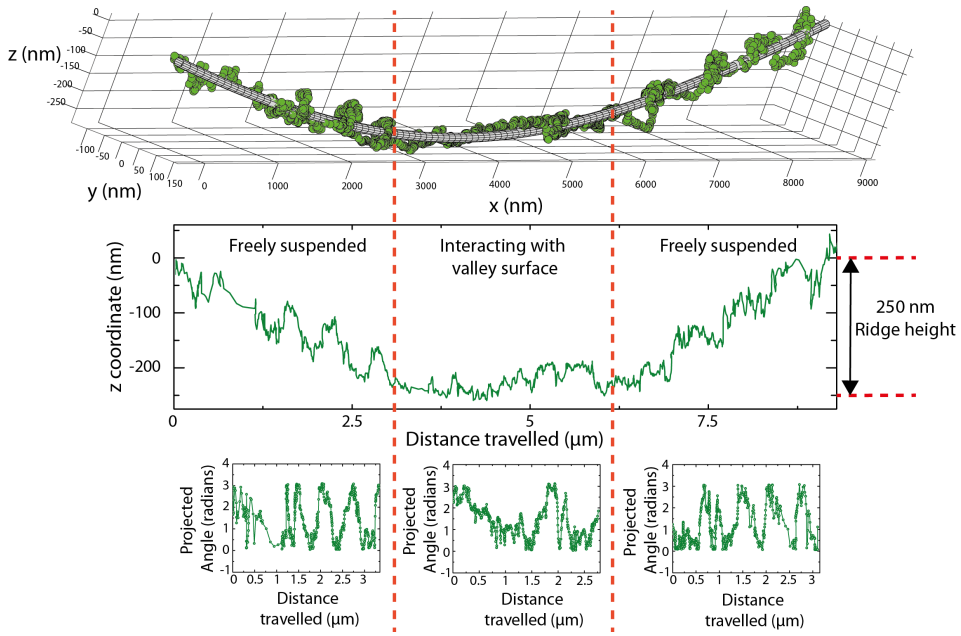

Figure 3.9: 3D motility of Kip3 is hindered on surface interacting MTs. 3-D tracking data around the fitted tube for an example Kip3-QDot event at 10 µM ATP. Plot of the z-coordinate versus the forward distance travelled indicates that the template MT for the Kip3-QDot event is freely suspended at the ends but touches the valley surface in the middle. The track is split into 3 sections indicated by the red dotted lines. The Kip3-QDot rotates freely in the first suspended section as indicated by the 3-D tracking data around the fitted tube and plot of the projected angle with linear distance travelled. The pitch is 0.68 ± 0.07 µm, and the average distance of the Kip3-QDot track from the fitted tube surface is 19.5 nm. The rotational motion of the Kip3-QDot is restricted in the second section where the MT interacts with the surface as indicated by the 3-D tracking data around the fitted tube and plot of the projected angle with linear distance travelled. The average distance of the Kip3-QDot track from the fitted tube surface is 9.4 nm. The Kip3-QDot rotates freely in the third suspended section as indicated by the 3-D tracking data around the fitted tube and plot of the projected angle with linear distance travelled. The pitch is 0.66 ± 0.07 µm, and the average distance of the Kip3-QDot track from the fitted tube surface is 15.3 nm.

are positive for left-handed rotation). For this example track, the rotational pitch is 2.1 ± 0.3 µm (average velocity = 43 ± 1 nm/s; number of rotations = 3).

For statistical evaluation of the Kip3-QDot motion, 50 (out of 77) tracks found suitable for tube fitting showed clear left-handed helical motion. The analysis of the rotations yielded 110 complete rotations for the 50 tracks with an estimated rotational pitch of 1.9 ± 0.3 µm and average velocity of 43 ± 5 nm/s4. Furthermore, the cumulative angles versus travelled distance for these Kip3-QDot events showed a clear preference in directionality towards the left (slope = 30 ± 50 °/µm; Figure 3.8D). The remaining 23 tracks did not rotate robustly around the MT but showed rather erratic transverse motion (Figure 3.8E). In addition, the distance from the

fitted tube for these unclear events was 14.1 ± 3.2 nm, which is significantly lower than for the other 50 tracks (17.9 ± 2.9 nm; p=0.003, Mann-Whitney U test). The unclear tracks could either hint towards an alternate mode of motility for the Kip3-Qdots or simply arise due to poor tracking, poor fitting or motors moving on surface-interacting MTs not rejected during the pre-screening. Indeed, for the example Kip3-QDot event (at limiting ATP conditions) along a MT interacting with the valley surface in the middle (Figure 3.9), it was observed that the Kip3-QDot rotated robustly at the suspended ends but moves rather erratically in the middle where the MT was interacting with the surface. Further, the average distance from the fitted tube for the middle section of the event was much lower (9.4 nm) than for the suspended ends (19.5 nm and 15.3 nm). Therefore, when the entire 3D lattice of a MT is accessible, unhindered Kip3 motors have a left-handed helical trajectory.

3.5 Discussion

In this chapter, a robust suspended MT assay was established by immobilizing MTs on 250 nm high polymer ridges stamped on glass using UV-NIL lithography, allowing the entire MT lattice to be accessible for interaction with motors and MAP. By suspending MTs reliably at a height of 200-250 nm, the motility of single Kip3 motors coupled to QDots was studied in 3D, using Parallax, in conjunction with HILO imaging, to significantly reduce the background due to QDots diffusing in solution.

In the 3D stepping assays it was observed that single Kip3 motor proteins move in a left-handed helical trajectory around the longitudinal axis of the MTs with a pitch of ~2 µm. This pitch is significantly shorter than the supertwist of double stabilized MTs (~8 µm), consistent with observations made in gliding rotation assays (see previous chapter). This validates the hypothesis that single Kip3 motors do not move along a single MT protofilament but can stochastically switch protofilaments. Since, observed clear left-handed helical trajectories were observed, the side-stepping has to be biased towards the left, with approximately 1 leftward side-step every 18 forward steps. While Bugiel et al. [155] also verify that Kip3 can sidestep on the MT lattice, they suggest that protofilament switching occurs in both directions (even against load). However, the Kip3 motility in their

assay was observed with large polystyrene beads (0.6 µm diameter) under axial or longitudinal load. It can be speculated that the contrary observation made in Bugiel et al. is due to the application of load on the motor. It has been hypothesized that Kip3 is occasionally triggered to switch out of the step cycle when subjected to any axial or longitudinal load allowing it to enter a weakly bound slip state where it diffuses unspecifically, allowing for the observations made using optical tweezers [137, 155]. The results in this work demonstrate that unloaded Kip3 motors sidestep with a leftward bias, which indicates that protofilament switching is most likely to occur with the regular step cycle of the motor.

The structural elements that provide Kip3 the capacity to perform side-steps within the step cycle can be speculated upon. Assuming motility in a hand-over-hand fashion, it will matter which features in the motor structure can extend the reach of the forward stepping motor head. Based on recent studies, it can be hypothesized that there are two factors that determine the side-stepping capacity of processive kinesin motors:

- **Flexibility of the neck:** Studies on kinesin-1 have revealed that a flexible neck region increases the reach of the forward binding motor head thereby allowing it to switch protofilaments [98, 158]. A recent study predicting the structure of Kip3 and other kinesin-8s indicates that the first heptad of the neck region has a low probability of forming a coiled coil [134]. It can be speculated that during forward stepping the first heptad of the neck coiled-coil can uncoil, providing Kip3 motors the extension necessary to reach tubulin-binding sites in the adjacent left protofilament, as observed for a kinesin-1 mutant with a flexible neck [98].

- **Length of the neck-linker:** In previous studies on kinesin-2 motors it has been speculated that the motor can side-step due to a neck-linker longer than kinesin-1 18aa in comparison to 14aa) [58, 110]. In a collaboration work with the laboratory of Professor Jonathan Howard, we proposed a similar hypothesis for Kip3 (see Bormuth et al. for all details [92]). Briefly, primary sequence allignment of Kip3 with other kinesin-8 motors reveal that the neck-linker of Kip3 is longer than kinesin-1 (17aa in comparison to 14aa). Accounting for necklinker docking of the rear motor head [159], the corresponding length of the necklinkers between both heads was estimated

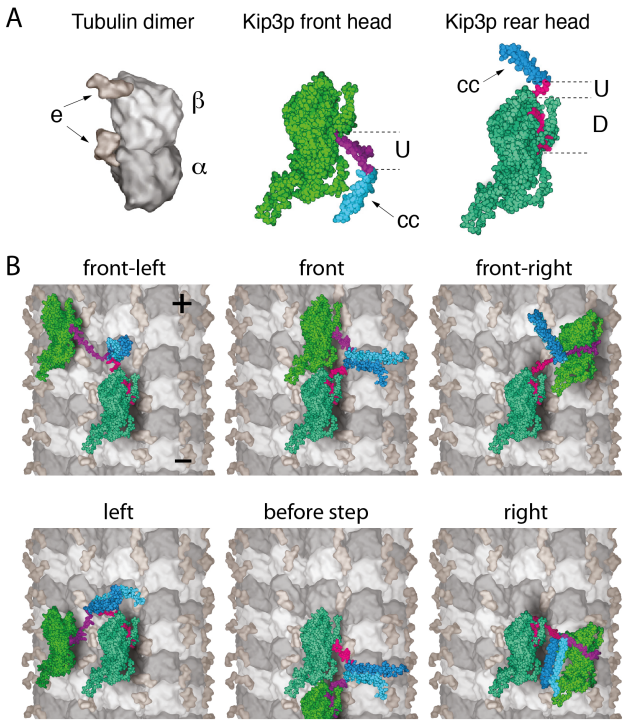

C

position	distance (Å)	
	3D model	tubulin-tubulin
front	53	81
left	79	60
front-left	93	108
front-right	103	93
right	105	60

Figure 3.10: Virtual 3D-reconstruction of Kip3 stepping. The model is based on a combination of atomic coordinates for kinesin-1 [156, 157] (where additional amino acids in the Kip3 motor domain compared to kinesin-1 were inserted as unstructured peptide chains) and MTs [92] obtained by x-ray crystallography and electron-tomography. **(A)** Tubulin dimer: composed of α-tubulin and β-tubulin monomers, with the unstructured surface-exposed e-Hooks (e). Kip3 front head: shown with undocked necklinker (U) and following coiled-coil dimerization domain (cc). Kip3 rear head: shown with docked (D) and undocked (U) neck-linker parts. **(B)** Illustration of different Kip3 configurations bound with both heads to adjacent tubulin dimers. **(C)** Estimated 3D distances between the positions where the neck-linkers protrude from the motor heads, respecting the volumes of the heads. For comparison, the direct distances between the corresponding tubulin dimers are given. Comparison between the 3D distances obtained from the model and the available neck-linker length (85 Å) suggests that a forward-swinging Kip3 head (i) can most readily reach the tubulin dimer in the front (53 Å needed), (ii) can switch to the protofilament on the left (79 Å for left and 93 Å for front-left needed), but (iii) has difficulties to step to the protofilament on the right which would require a longer neck-linker than it actually exhibits (103 Å for front-right and 105 Å for right needed). The modeled preference for left-stepping over right-stepping is in agreement with the results.

to be 85 Å. As illustrated in Figure 3.10A and 3.10B, all configurations of Kip3 with both heads bound simultaneously to adjacent tubulin dimers were modelled using previous x-ray crystallography and electron-tomography data on kinesin-1 (where additional amino acids in the Kip3 neck-linker were inserted as unstructured peptide chains). Comparisons between the 3D distances obtained from the model (Figure 3.10C) and the available neck-linker length (85 Å) suggest that the forward stepping motor head of Kip3 can easily reach the forward tubulin-binding site (53 Å), sideward left tubulin-binding site (79 Å) and perhaps even the forward left tubulin-binding site (93 Å). However, it may have difficulties switching to the right protofilament due to the motor geometry. This would explain why Kip3 motors preferentially step to the left protofilaments.

In conclusion, a novel experimental setup has been established to study the 3D trajectories of single Kip3 motors. Using the setup, it was observed that Kip3 motors have left-handed helical trajectories around the MT lattice, which can be attributed to their flexible neck and longer neck-linker. In the next chapter the rotational motion of Kip3 is studied in a quantitative manner under different experimental conditions to understand exactly how the side-stepping is coupled to the mechanochemical cycle of the motor.

Acknowledgements

Prof. Wilhelm Walter provided assistance in making the Kip3-mfGFP construct. The Parallax setup was built by Dr. Felix Ruhnow and Dr. Friedrich Schwarz. The analysis and fitting protocol was developed with Dr. Felix Ruhnow. Polymer patterned glass structures were fabricated by Dr. Salvatore Girardo. 3D reconstruction of Kip3 stepping was performed by Burkhard Rammner.

CHAPTER 4

Sidestepping mechanism of Kip3

Three dimesional assays developed in the previous chapters provide unambiguous evidence that Kip3 employs a directed left-biased sidestepping strategy. Further analysis of 3D stepping and gliding data revealed that sidestepping is not directly coupled to forward stepping but sidestepping probability increases with step dwell time. Additionally, it was observed that sidestepping probability increases on (i) prolonging the step dwell time by limiting the ATP concentration and (ii) weakening the motor-MT interactions by chopping the MT e-hooks. It was hypothesized, supplemented with numerical simulations, that in the ATP waiting state the motor can switch from a two head-bound (2HB) to a one head-bound (1HB) conformation with sidestepping predominantly possible if ATP binds in the 1HB conformation. Finally, it was shown that a kinesin-1 mutant with an extended neck-linker can switch protofilaments under rate-limiting ATP conditions hinting towards a general side-stepping mechanism coupled to the step cycle for all processive kinesins with long neck-linkers.

4.1 Leftward sidestepping is not directly coupled to the forward stepping.

In Chapter 3, 3D tracking of single Kip3 motors on suspended MTs confirmed that Kip3 undergoes left-handed helical motion around the MT lattice. However, there was a substantial variation in Kip3-QDot track velocities (ranging from 35-55 nm/s) and rotational pitches (ranging from 1-3 µm). Interestingly, on plotting the rotational pitch with respect to the average velocity for each of the 50 tracks (Figure 4.1A; data for individual rotations is also shown) a significant dependence of the rotational pitch on the velocity ($R = 0.43$, $p<0.01$; pearson correlation coefficient) can be observed.

Gliding motility assays using S-MTs in combination with FLIC microscopy (referred to as speckle-FLIC gliding assays) provide a simpler alternate means to investigate the rotational motion of Kip3 motors. However, in contrast to the single molecule Kip3-QDot data (performed on Kip3-mfGFP) the observed rotational pitch and gliding velocity of MTs gliding on Kip3-eGFP motors (rotational pitch ~1-1.5 µm and gliding velocity ~20-50 nm/s; see Chapter 2) was much lower. To overrule artifacts due to different constructs, speckle-FLIC gliding assays were performed with Kip3-mfGFP motors. Consistent with the previous FLIC gliding assays (in Chapter 2) a lower rotational pitch (1.6 ± 0.1 µm) and average velocity (34 ± 2 nm/s; N=315) was observed. Also, the variation in rotational pitch and gliding velocity was substantial (as observed for FLIC gliding assays with Kip3-eGFP in Chapter 2). However, on plotting the rotational pitch with respect to the average velocity, an even stronger dependence of the rotational pitch on the velocity was observed ($R = 0.87$, $p<0.001$; Figure 4.1B) that extended well to the data obtained for single Kip3-QDot tracks. Since the results from both experiments are consistent, the data was combined to investigate the correlation of rotational pitch and velocity ($R = 0.80$, $p<0.001$). This indicates that there is a linear dependence of rotational pitch of the motor (MT) on the stepping (gliding) velocity.

The rotational pitch and motor velocity information was used to calculate individual motor parameters such as forward stepping rate (the rate at which the motor steps forward), dwell time per forward step (the average time taken per forward step), sidestepping rate (the rate at which the motor performs sidesteps to the left) and sidestepping probability (the probability to perform a leftward sidestep

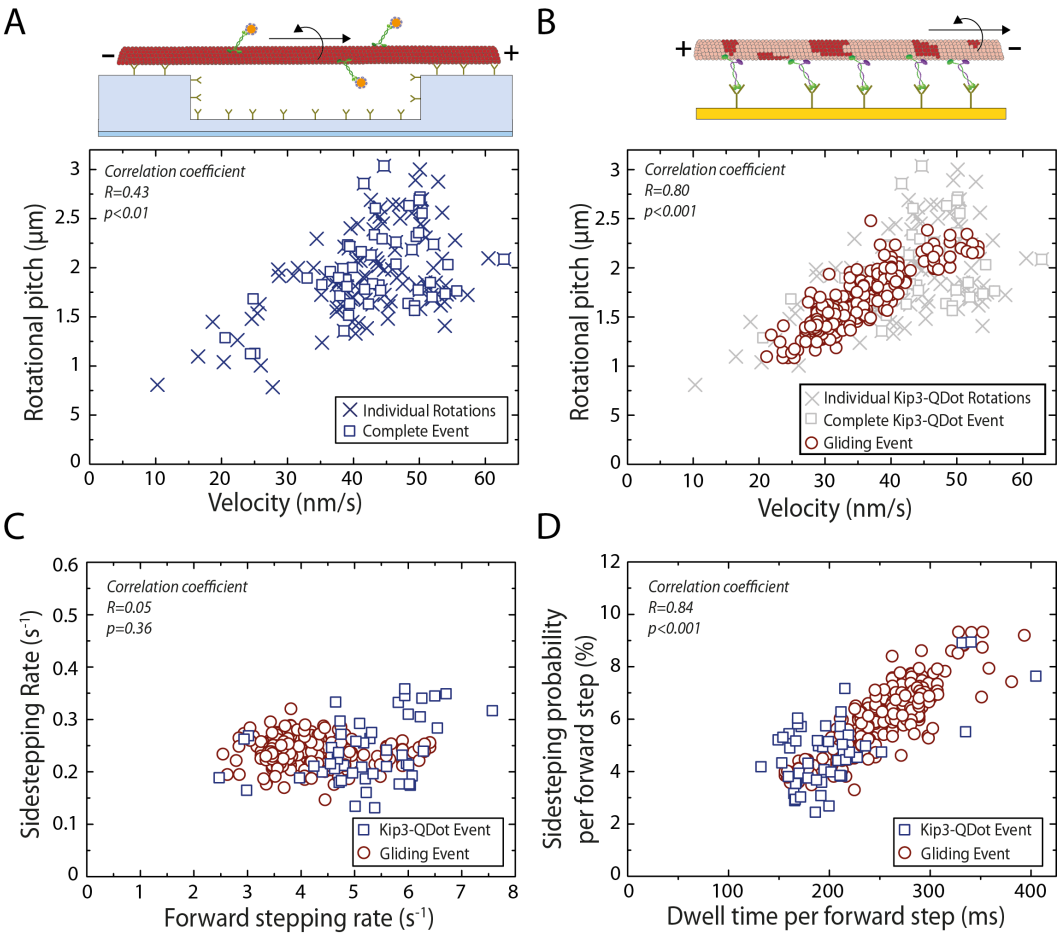

Figure 4.1: Analysis of the rotational pitch for Kip3. (A) The rotational pitch of 50 Kip3-QDot tracks is shown in dependence on the forward velocity. Each individual rotation is represented by a blue cross while a blue square represents one complete Kip3-QDot track. **(B)** The rotational pitch of MTs in Kip3 driven speckle-FLIC gliding assays is shown in dependence on the forward velocity. Here, the rotational pitch of 315 MTs is represented by red circles and single molecule Kip3-QDot data is shown in grey for reference. There is a significant dependence of the rotational pitch on the velocity in both experiments (single molecule R = 0.43, p<0.01; gliding assay R = 0.87, p<0.001; combined R = 0.80, p<0.001; pearson correlation coefficient). **(C)** Estimated sidestepping rate for the data shown in **(A)** and **(B)** is plotted against the forward stepping rate (blue squares single molecule assay, red circles gliding assay). The sidestepping rate is similar in both experiments (combined 0.24 ± 0.01 sidesteps per second, N = 365) and no significant dependence of sidestepping rate on the forward stepping rate can be observed (combined R = 0.05, p= 0.36). **(D)** Estimated sidestepping probability per forward step is shown in dependence of the average dwell time per forward step (blue squares single molecule assay, red circles gliding assay). Here, the sidestepping probability for each forward step strongly depends (combined R = 0.84, p<0.001) on the amount of time it takes to make a forward step.

per forward step), as described below.

Calculation of motor parameters

Double-stabilized MTs have a lefthanded supertwist with a pitch of Ψ_0=8.4 µm (average rotational pitch obtained for kinesin-1 driven speckle-FLIC gliding assays in Chapter 2), a tubulin interdimer distance of $d_{\mathbf{step}} = 8.3\,\text{nm}$ [160] and 14 protofilaments. Kinesinss that do not switch protofilaments (e.g. kinesin-1) would then slightly rotate to the left in order to complete a full rotation within 8.4 µm. The angle per step can then be calculated as $\theta = 360^\circ/N_{\mathbf{steps}} = 360^\circ/(8400/8.3) = 0.36^\circ$

For Kip3 the number of forward steps $N_{\mathbf{steps}}$ per full rotation (rotational pitch $\Psi_{\mathbf{Kip3}}$ is ~1.9/um in 3D stepping assays; see chapter 3) is much lower ($N_{\mathbf{steps}} = \Psi_{\mathbf{Kip3}}/d_{\mathbf{step}} = 1900/8.3 = 229$) and this would only account for 82° of the rotation ($N_{\mathbf{steps}} \times \theta_{\mathbf{step}}$). The remaining 278° must be attributed to sidestepping. Since 14 PF would yield a $\theta_{\mathbf{PF}} = 360^\circ/14 = 26^\circ$ for each protofilament switch, Kip3 must switch protofilaments $N_{\mathbf{switch}} = 278^\circ/\theta_{\mathbf{PF}} = 278^\circ/26 = 11$ times while it takes 229 forward steps. This yields a sidestep per forward step probability of 5 % (one sidestep per 21 forward steps). The side sidestepping rate $k_{\mathbf{sidestep}} = N_{switch} \times v_{\mathbf{Kip3}}/\Psi_{\mathbf{Kip3}}$ ($v_{\mathbf{Kip3}}$ is the velocity of Kip3 during rotation). In summary, the sidestep probability and rate can be calculated from the rotational pitch $\Psi_{\mathbf{Kip3}}$ (given in nm) and velocity $v_{\mathbf{Kip3}}$ (given in nm/s) by:

$$P_{\mathbf{sidestep}} = \frac{N_{\mathbf{switch}}}{N_{\mathbf{steps}}} = \frac{14 \times d_{\mathbf{step}} \times (1 - \Psi_{\mathbf{Kip3}}/\Psi_0)}{\Psi_{\mathbf{Kip3}}} \tag{4.1}$$

where $d_{\mathbf{step}} = 8.3\,\text{nm}$ and $\Psi_0 = 8400\,\text{nm}$

$$k_{\mathbf{sidestep}} = N_{\mathbf{switch}} \times \frac{v_{\mathbf{Kip3}}}{\Psi_{\mathbf{Kip3}}} = \frac{14 \times v_{\mathbf{Kip3}} \times (1 - \Psi_{\mathbf{Kip3}}/\Psi_0)}{\Psi_{\mathbf{Kip3}}} \tag{4.2}$$

where $\Psi_0 = 8400\,\text{nm}$

Further, the forward stepping rate $k_{\mathbf{forward}}$ and dwell time per forward step $t_{\mathbf{step}}$ can be calculated from the velocity $v_{\mathbf{Kip3}}$ by:

$$k_{\mathbf{forward}} = \frac{v_{\mathbf{Kip3}}}{d_{\mathbf{step}}} \tag{4.3}$$

$$t_{\mathbf{step}} = \frac{1}{k_{\mathbf{forward}}} \tag{4.4}$$

From the combined data obtained for Kip3 from 3D stepping and speckle-FLIC gliding assays, the sidestepping rate was calculated and plotted against the forward stepping rate (Figure 4.1C). Here, no dependence of the sidestepping rate on the forward stepping rate was observed ($R = 0.05$, $p = 0.36$) and the sidestepping rate was constant (0.24 ± 0.01 sidesteps per second; $N = 368$) for a large range of forward stepping rates (2.5-7.5 forward steps per second). This means that the sidestepping is uncoupled from the forward stepping and the sidestepping probability strongly depends ($R = 0.84$, $p<0.001$) on the forward step dwell time (Figure 4.1D).

4.2 ATP waiting state is the crucial step for sidestepping

In the 3D stepping and speckle-FLIC gliding assays for Kip3, it was observed that sidestepping is uncoupled from the forward stepping and the probability to sidestep for each forward step (3-9 %) strongly depends on the amount of time it takes to make a forward step (150-400 ms; Figure 4.1D). To further understand the origin of this uncoupling of sideward stepping and forward stepping, several experimental parameters were varied in order to affect the dwell time per forward step.

First, the dwell time per forward step was changed by varying the temperature (17-32 °C) in Kip3 driven speckle-FLIC gliding assays and the rotational pitch of gliding MTs was measured. Though the dwell time per forward step could be varied significantly (100 to 500 ms per forward step) only a marginal variation in the sidestepping probabilities (between 7 % and 8 %) was observed (Figure 4.2A). Since temperature affects all the transition rates in the step cycle simultaneously, this observation indicates that the sidestepping is linked to a specific state in the step-cycle and not to the complete step.

Second, Kip3 driven speckle-FLIC gliding assays were performed with additional phosphate ions (P_i) in the imaging solution. This would theoretically extend the time spent by the motor in the post-hydrolysis ADP.P_i state (shown to be a rate-limiting step in the kinesin-1 step cycle [80]). In control stepping assays on Kip3, additional P_i (exchanging 112.5 mM KCl with KPi in the imaging solution) changed the dwell time per forward step marginally (~3% increase in buffer with additional P_i), indicating that the post-hydrolysis ADP.P_i state is not rate-limiting

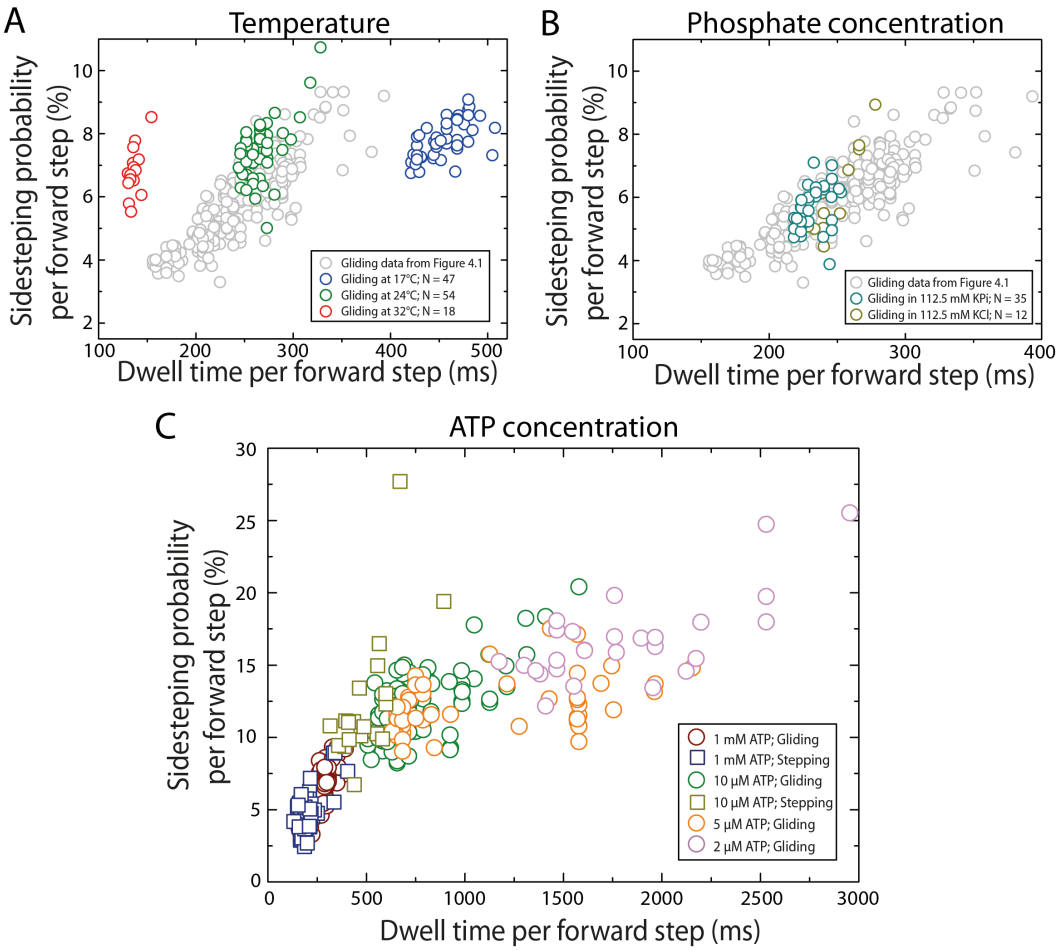

Figure 4.2: Experimental parameters that influence sidestepping probability of Kip3. (A) Speckle-FLIC gliding assays were performed at 17 °C (blue), 24 °C (green) and 32 °C (red). While the dwell time per forward step varied substantially (453 ± 19 ms at 17 °C, 262 ± 10 ms at 24 °C and 135 ± 5 ms at 32 °C) there was only a marginal increase in sidestepping probability per forward step on decreasing temperature (6.5 ± 0.5 % at 17 °C, 7.5 ± 0.4 % at 24 °C and 7.7 ± 0.3 % at 32 °C). Gliding data from Figure 4.1B is plotted in grey for reference. **(B)** Speckle-FLIC gliding assays were performed in assay buffer with additional P_i (BRB80 with 112.5 mM KPi) followed by exchange of the normal assay buffer (BRB80 with 112.5 mM KCl). Both, the dwell time per forward step (230 ± 10 ms in buffer with KPi and 244 ± 22 ms in buffer with KCL, p = 0.012) and the sidestepping probability per forward step (5.8 ± 0.7 % in buffer with KPi and 5.7 ± 1.8 % in buffer with KCL, p = 0.913) do not change significantly in the buffer with additional P_i. **(C)** The estimated sidestepping probability per forward step is shown in dependence of the dwell time per forward step for Kip3-QDot tracks (squares) at 1 mM (blue; N = 50) and 10 µM ATP (olive; N = 19) as well as for MT gliding events (circles) at 1 mM (red; N = 315), 10 µM (green; N = 146), 5 µM (orange; N = 61) and 2 µM ATP (pink; N = 48). The leftward sidestepping probability per forward step increases with increase in dwell time per forward step, eventually saturating at ~20 % probability to make a leftward protofilament switch per forward step.

for the Kip3 step cycle. Indeed, upon measuring the rotational pitch of MTs in Kip3 driven speckle-FLIC gliding assays with additional P_i in the imaging solution no significant change was observed in either the sidestepping probability ($p = 0.913$; Figure 4.2B) or the dwell time of the forward step ($p = 0.012$). This suggests that the post-hydrolysis ADP.P_i state does not play a crucial role in the side-stepping mechanism.

Finally, the dwell time per forward step was prolonged by limiting the ATP concentration thereby extending the ATP waiting state. 3D stepping assays using Kip3-QDots were performed on suspended microtubules at limiting ATP conditions (10 µM ATP) and it was observed that most Kip3-QDot tracks again had a left-handed helical trajectory on the MT. Here, 19 tracks (with 50 complete rotations) yielded an estimated rotational pitch of 0.9 ± 0.2 µm, average velocity of 17 ± 5 nm/s and slope of the cumulative angle 300 ± 100 °/µm. Kip3-QDot stepping assays with ATP concentration lower than 10 µM ATP could not be performed reliably because the Kip3-QDot tracks were too short (less than two rotations before dissociation of Kip3-QDots from the MTs). Therefore, Kip3 driven speckle-FLIC gliding assays were performed and the rotational pitch as well as the average velocity of MTs was measured at 10 µM ATP (0.9 ± 0.1 µm, 12 ± 1 nm/s; $N = 146$), 5 µM ATP (0.9 ± 0.1 µm, 7 ± 5 nm/s; $N = 61$) and 2 µM ATP (0.7 ± 0.1 µm, 5 ± 1 nm/s; $N = 48$). Figure 4.2C shows the measured sidestepping probability for each individual track (both stepping and gliding motility assays) in dependence of the step dwell time. It was observed that the sidestepping probability increased with the dwell time per forward step (extending the trend observed at 1 mM ATP in Figure 4.1D) eventually saturating at 15-20 % (per forward step). This indicates that the sidestepping mechanism is linked to the ATP waiting state.

4.3 Proposed model for Kip3 sidestepping

One possibility to explain the dependence of the sidestepping probability with dwell time per forward step (extended by prolonging the ATP waiting state) is that Kip3 waits for ATP in two different conformations, both of them having different side-stepping probabilities. In case of kinesin-1, it has been shown that the motor can transition from the 2HB conformation to a 1HB conformation while waiting for ATP [81, 84, 161–164]. It is possible that a similar transition,

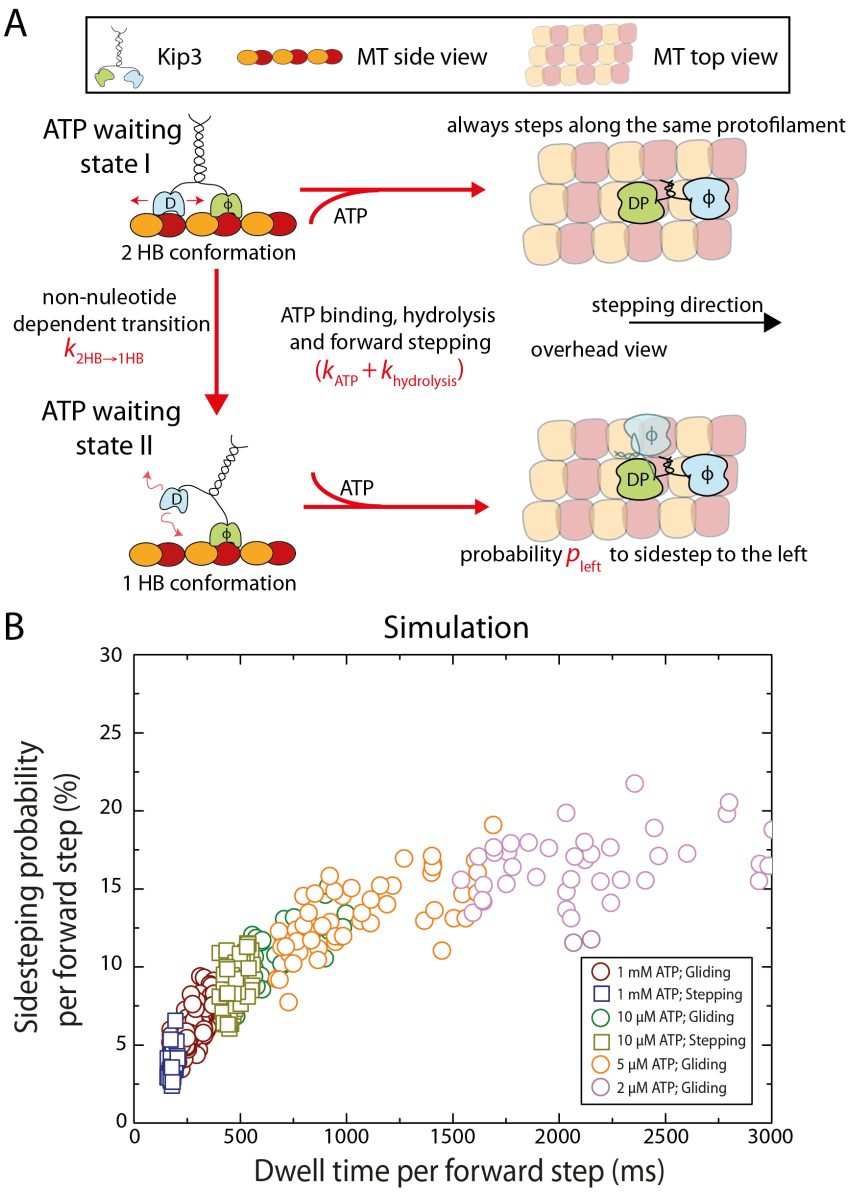

Figure 4.3: Proposed model for the sidestepping mechanism of Kip3. (A) Illustration of the proposed model to explain the increase in sidestepping probability upon increasing the duration of the ATP waiting state. It is possible that Kip3 can undergo a nucleotide independent transition from a 2HB conformation to a 1HB conformation ($k_{\mathbf{2HB \rightarrow 1HB}}$) in the ATP waiting state. Further, sidestepping is only possible upon ATP binding in the 1HB conformation with a probability. **(B)** The simulated sidestepping probability per forward step is shown in dependence of the dwell time per forward step for 50 single molecule tracks at 1 mM and 10 µM ATP as well as for 300 gliding MTs at 1 mM and 50 gliding MTs at 10 µM, 5 µM and 2 µM ATP (same markers and colors as in Figure 4.2C). Parameters of the numerical simulation are given in Table 4.1. Here, the difference between single molecule and gliding motility assays is only the probability of futile steps (ranging between 0-50 % for gliding events and 0-20 % for stepping events) to account for the experimentally observed velocity variations.

which is nucleotide independent, occurs for Kip3 and sidestepping predominantly occurs in the 1HB conformation (Figure 4.3A). This would explain the observation made in Figure 4.3C, which indicates that the sidestepping probability increases when the ATP waiting state of Kip3 is prolonged. Further, the saturation of sidestepping probability at 15-20 % (per forward step) suggests that there is a maximum sidestepping probability ($p_{\mathbf{left}}$) of the motor in the 1HB conformation which is predominantly populated at low ATP concentration.

To verify the proposed model, Kip3 gliding and stepping events were simulated as single Poisson steppers using Monte-Carlo simulations on a MATLAB-based computer program. Here, three states were assumed: (i) a 2HB ATP waiting state (Figure 4.3A, state I), (ii) a 1HB ATP waiting state (state II) and (iii) a hydrolysis state that includes ATP hydrolysis, motor head attachment and ADP as well as P_i release (remainder of the cycle). The simplification for the states was based on the hypothesis that there are two different motor conformations when Kip3 waits for ATP (therefore ATP dependent), while the rest of the step cycle is independent of the ATP concentration. Furthermore, the binding rates for ATP as well as the remaining transitions rate were the same in both conformations. The transition from the 2HB-ATP to 1HB-ATP conformation ($k_{\mathbf{2HB\rightarrow 1HB}}$) is nucleotide independent and was estimated from the sidestepping probability at 1 µM ATP. To account for the experimentally observed velocity variations (at same ATP concentrations) a probability of futile steps $p_{\boldsymbol{futile}}$ was added, which introduces a heterogeneity in the ATP binding rate for each simulated motor. The parameters $t_{\mathbf{step(max)}}$ (dwell time per step at saturating ATP concentration) and $K_{\mathbf{M}}$ (Michelis-Menten constant; ATP concentration at which the motor velocity is halved) were determined by fitting the dependence of the velocity on ATP concentration with Michelis-Menten kinetics (Figure 4.4). The parameter $p_{\mathbf{left}}$ was approximated from the saturation value of the sidestepping probability observed in Figure 4.2C and $d_{\mathbf{step}}$ was obtained from literature [160]. The parameters $t_{\mathbf{rest}}$, $k_{\mathbf{2HB\rightarrow 1HB}}$ and $p_{\mathbf{futile}}$ were approximated from the best fit of the model to the data in Figure 4.2C. Dwell time and sidestepping information for each simulated event was obtained by averaging over 2 rotations (14 protofilament switches constitute 1 rotation) for stepping events and by averaging over 6 rotations for gliding events. The MATLAB code of the simulation is included in the Supplementary information and the parameters for the simulation are listed in Table 1.

Simulation Parameter	Value
$t_{\mathbf{step(max)}}$	160 ms (at 1 mM ATP)
$t_{\mathbf{waiting\ ATP(max)}}$	115 ms (at 1 mM ATP)
$t_{\mathbf{rest}}$	45 ms (independent of [ATP])
$d_{\mathbf{step}}$	8.3 nm
$K_{\mathbf{M}}$	15 µM
$t_{\mathbf{step}}$([ATP])	$t_{\mathbf{step(max)}}\times$ ([ATP]+$K_{\mathbf{M}}$)/[ATP]
$k_{\mathbf{ATP}}$([ATP])	1/($t_{\mathbf{step}}$([ATP])-$t_{\mathbf{rest}}$)
$k_{\mathbf{ATP(max)}}$	8.70 s^{-1} (at 1mM ATP)
$k_{\mathbf{2HB\rightarrow 1HB}}$	2.18 s^{-1} (on normal MTs)* 4.35 s^{-1} (on subtilisin treated MTs)*
$p_{\mathbf{left}}$	18 %
$p_{\mathbf{futile}}$	0-20 % (for stepping events)* 0-60 % (for gliding events)* 20-45 % (for subtilisin treated MT gliding events)*

Table 4.1: Parameter of the numerical simulation using the proposed model. The dwell time $t_{\mathbf{step(max)}}$ at saturating ATP conditions was determined by fitting the dependence of the velocity on ATP concentration with Michalis-Menden kinetics (see Figure 4.3). The dwell time of the ATP hydrolysis $t_{\mathbf{hydrolysis}}$ was adjusted in order to get a similar slope as in Figure 4.1D. While $t_{\mathbf{rest}}$ is not affected by ATP concentration, $t_{\mathbf{step}}$([ATP]) and $t_{\mathbf{waiting\ ATP}}$([ATP]) change with decreasing ATP concentration. The average dwell time at different ATP concentrations was calculated with the estimated $K_{\mathbf{M}}$ from control stepping assays (see Figure S6). The ATP binding rate is then estimated for the different ATP concentrations, while the transition rate from the 2HB to the 1HB conformation $k_{\mathbf{2HB\rightarrow 1HB}}$ was kept constant since it is assumed to be a non-nucleotide dependent transition. Only the simulations of gliding events with subtilisin treated MTs used an increased transition rate $k_{\mathbf{2HB\rightarrow 1HB}}$ due to a weaker interaction of the ADP bound motor with the MT (see Figure 4.5A). The probability $p_{\mathbf{left}}$ can be estimated from the saturating sidestepping probability at limiting ATP conditions (see Figure 4.2C) and a probability for futile steps $p_{\mathbf{futile}}$ was added to account for the experimentally observed velocity variations, which might be due to multi-motor effects. * indicates that the values are estimated from best fit to experimental data.

Figure 4.3C shows data from numerical simulation of Kip3 motility using the proposed model with a transition rate $k_{\mathbf{2HB\rightarrow 1HB}}$ 4-fold lower than the ATP binding rate at saturating ATP concentration ($k_{\mathbf{ATP(max)}}$). It was assumed that the ATP waiting state is one of the rate-limiting steps with the motor spending 70 % of the ~160 ms long step cycle waiting to bind ATP ($t_{\mathbf{waitingATP(max)}} \cong 0.7 \times t_{\mathbf{step(max)}}$). The model also includes that once the motor transitions to the 1HB conformation it can step to the neighboring protofilament (on the left) with the probability $p_{\mathbf{left}}$ = 0.18. The good agreement of the numerical simulation with the experimental data shows that the proposed model can indeed be used to describe the Kip3 motility at varying ATP concentrations.

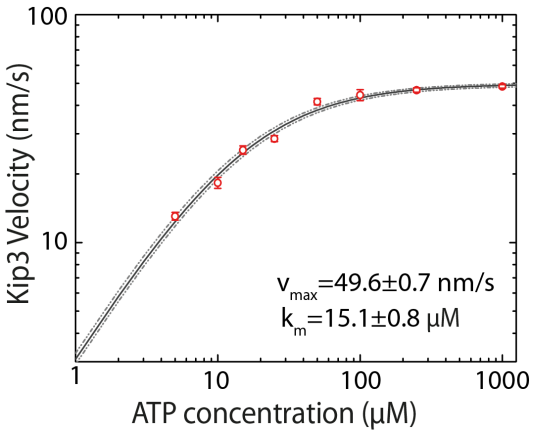

Figure 4.4: Dependence of Kip3 stepping velocity with ATP concentration. The Kip3 stepping velocity varies with ATP concentration (plotted logarithmically) according to Michelis-Mentis kinetics, yielding maximum stepping velocity $v_{\mathbf{max}}$=49.6 ± 0.7 nm/s and $K_{\mathbf{M}}$=15.1 ± 0.8 µM. Each data point in the graph represents the 90-350 stepping events.

4.4 Leftward sidestepping probability increases with higher transition rate from 2HB to 1HB conformation

According to this model (Figure 3A), an increase in the sidestepping probability is predicted if the transition rate from the 2HB to the 1HB conformation ($k_{\mathbf{2HB\rightarrow 1HB}}$) is increased. To test this hypothesis, Kip3 driven speckle-FLIC gliding assays were performed with subtilisin treated MTs where the negatively-charged e-hooks were cleaved off. On such MTs it was shown that the (diffusive) interaction of Kip3 in the presence of ADP is significantly weakened [165]. Likely, this modification of the MT surface leads to a weaker interaction of the trailing ADP-bound motor head, increasing the transition rate from the 2HB to the 1HB conformation. Indeed, when performing control assays with subtilisin treated MT at 1 µM a ~10-fold reduction in MT-association rate and interaction time was observed (Figure 4.5A). Still, control stepping assays with 1mM ATP showed normal motility of Kip3 motors with a ~10 % reduction of the stepping velocity (normal MTs 54 ± 3 nm/s, subtilisin MTs 49 ± 4 nm/s; imaged simultaneously; Figure 4.5B). The estimated rotational pitch (1.1 ± 0.1 µm, N = 159) for subtilisin treated MTs in Kip3 driven speckle-FLIC gliding assay (at 1 µM ATP) was shorter than for normal MTs while the velocity (35 ± 2 nm/s) was in the same range. Figure 4.5C shows the estimated sidestepping probability for each individual MT in the Kip3 driven speckle-FLIC

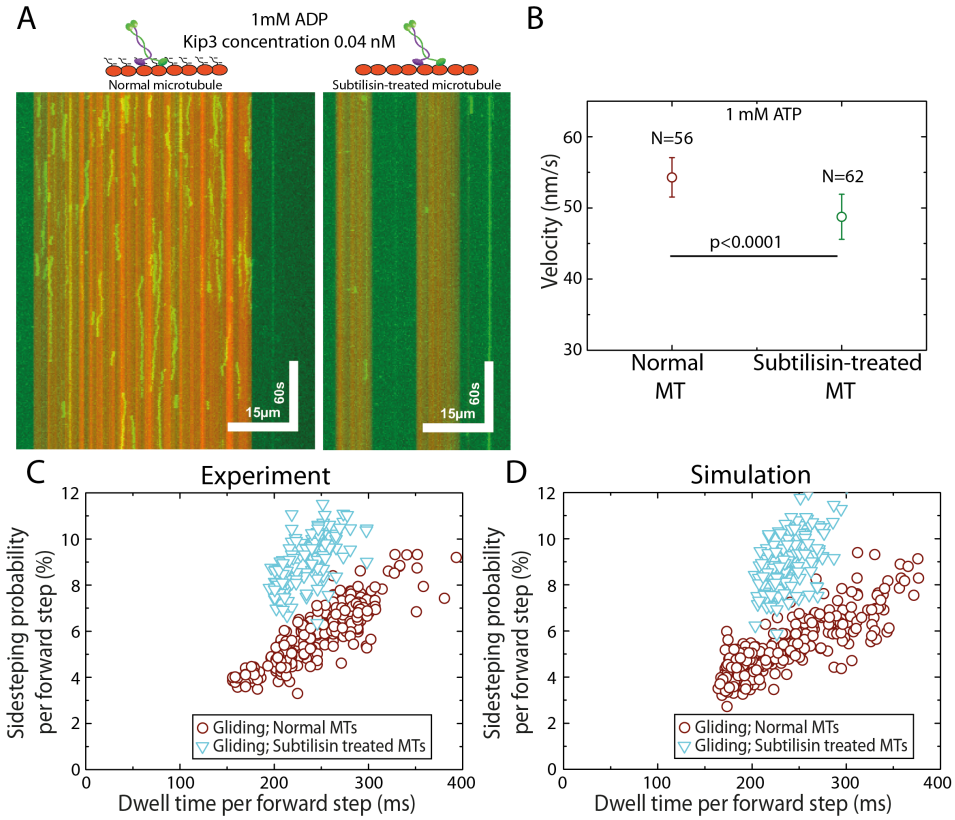

Figure 4.5: Sidestepping probability increases on changing the motor-MT interaction. **(A)** The interaction of Kip3 motor proteins on MTs at 1mM ADP was observed on normal (speckled rhodamine labeled) and subtilisin treated (1:3 rhodamine labeled) MTs coupled to the surface of the same channel. On subtilisin treated MTs a 10 folds lower MT association rate and interaction time was observed. Here, an example kymograph on a normal MT (left) and a subtilisin treated MT (right) is shown. MTs are represented in red and Kip3 motors are represented in green. **(B)** Kip3 stepping assays were performed at 1mM ATP and the stepping velocity of Kip3 motors on normal MTs (54 ± 3 nm/s; N = 56) was found to be significantly higher than the stepping velocity on subtilisin treated MTs (49 ± 4 nm/s; N = 62). **(C)** The estimated sidestepping probability per forward step is shown in dependence of the dwell time per forward step for normal (red circles; N = 315) and subtilisin treated MTs (green triangles; N = 159) in Kip3 driven speckle-FLIC gliding assays (1 mM ATP). MTs were treated with subtilisin to remove the negatively charged e-hooks, which weakens the motor-MT interaction in the ATP waiting state. Therefore, the increased sidestepping probability of subtilisin treated MTs is due to higher transition rate from the 2HB to the 1HB conformation ($k_{\mathbf{2HB \rightarrow 1HB}}$). **(D)** The simulated sidestepping probability per forward step is shown in dependence of the dwell time per forward step for 300 normal gliding MTs and 150 subtilisin treated MTs. Here, the transition rate ($k_{\mathbf{2HB \rightarrow 1HB}}$) for subtilisin treated MTs was increased 2-folds compared to normal MTs and $p_{\mathbf{futile}}$ (ranging between 20-50 %) was changed due to less velocity variations.

gliding assays (normal and subtilisin MTs). As predicted, the sidestepping probability increased when removing the MT e-hooks, and thereby increasing the transition rate $k_{\mathbf{2HB\rightarrow 1HB}}$. Again, numerical simulations using the proposed model were in good agreement with the experimental data for subtilisin treated MTs when the transition rate $k_{\mathbf{2HB\rightarrow 1HB}}$ was increased 2-folds (Figure 4.5D). This means, that the interaction of the trailing motor-head with the MT lattice (Figure 4.3A, in state I) is crucial for the sidestepping mechanism of Kip3.

4.5 Extension of the neck linker of kinesin-1 induces sidestepping under limiting ATP conditions

Finally, it was investigated if the proposed sidestepping mechanism for Kip3 can be generalized. It has been shown that kinesin-1 can also switch from a 2HB to a 1HB conformation in the ATP waiting state at limiting ATP concentrations [84]. Here, kinesin-1 driven speckle-FLIC gliding assays were performed at varying the ATP concentrations (1 mM ATP to 1 µM ATP) in order to prolong the ATP waiting state to the same order as for Kip3 (at 1 µM ATP). Figure 4.6A shows the rotational pitch at four different ATP concentrations (1 mM, 10 µM, 4 µM, 1 µM). Here, the rotational pitch only decreased slightly from 7.9 ± 0.3 µm for 1 mM ATP (N = 44) to 7.3 ± 0.5 µm for 1 µM ATP (N = 50), even though the step dwell time increased from 10 ms (817 ± 5 nm/s) to more than 900 ms (9 ± 1 nm/s), which is 6-fold longer than for Kip3 (at 1 mM ATP). The decrease in rotational pitch would result in a sidestepping probability of ~0.1 %, effectively one sidestep per 1000 forward steps (at limiting ATP concentration). Since the sidestepping probability would decrease further at saturating ATP concentration and because kinesin-1 takes 100 steps before detaching, sidestepping would occur very rarely, which is consistent with earlier studies that kinesin-1 follows the protofilaments [91, 93]. However, it has also been suggested that motors from kinesin-2 and kinesin-8 family can switch protofilaments due to a longer neck-linker (see Discussion in Chapter 3). Therefore, to verify if a longer neck-linker would enable kinesin-1 to sidestep speckle-FLIC gliding assays were performed with the kinesin-$1_{\mathbf{+DAL}}$ mutant (necklinker extended by 3 amino acids DAL at the C-terminal direction) [33]. Figure 4.6B shows the

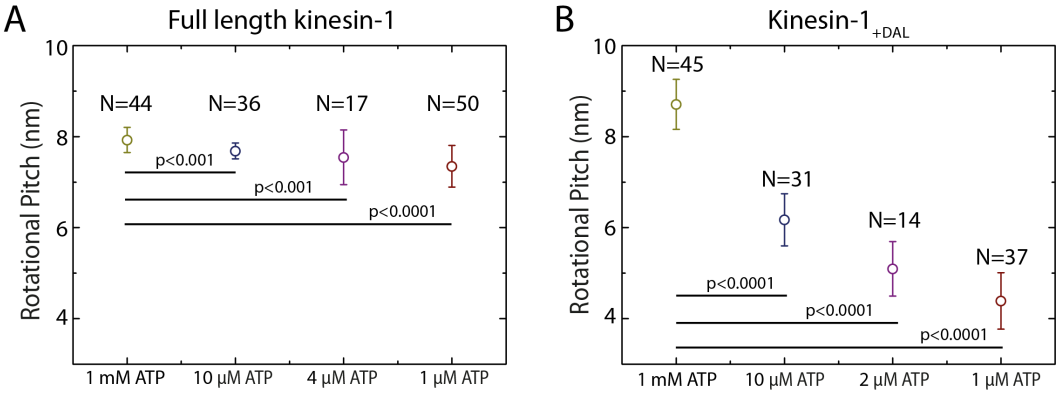

Figure 4.6: Kinesin-1 with an extended necklinker switches protofilament. (A) The rotational pitch of MTs in speckle-FLIC gliding assays with full length kinesin-1 is shown for various ATP concentrations. Here, the rotational pitch only decreased slightly from 7.9 ± 0.3 µm for 1 mM ATP (N = 44) to 7.3 ± 0.5 µm for 1 µM ATP (N = 50), even though the step dwell time increased from 10 ms (817 ± 5 nm/s) to more than 900 ms (9 ± 1 nm/s). **(B)** The rotational pitch of MTs in speckle-FLIC gliding assays with the kinesin-1+DAL mutant (necklinker extended by 3 amino acids DAL at the C-terminal direction) is shown for various ATP concentrations. Here, the rotational pitch decreased roughly 2-folds from 8.7 ± 0.6 µm for 1 mM ATP (N = 45) to 4.4 ± 0.6 nm/s for 1 µM ATP (N = 37), while the step dwell time increased from 17 ms (485 ± 6 nm/s) to 1600 ms (5 ± 1 nm/s).

rotational pitch at four different ATP concentrations (1 mM, 10 µM, 2 µM, 1 µM). Here, the rotational pitch decreased by ~50 % from 8.7 ± 0.6 µm for 1 mM ATP (N = 45) to 4.4 ± 0.6 µm for 1 µM ATP (N = 37), while the step dwell time increased from 17 ms (485 ± 6 nm/s) to 1600 ms (1 ± 1 nm/s). This means that the longer necklinker allows kinesin-1$_{\mathbf{+DAL}}$ to sidestep (at limiting ATP concentration) with a sidestepping probability of ~1.3 % (one sidestep per 77 forward steps). In conclusion, the results indicate that (i) the longer necklinker indeed enables the sidestepping of kinesin-1$_{\mathbf{+DAL}}$ and (ii) the sidestepping probability, similar to the case of Kip3, depends on the time spent by the motor in the ATP waiting state.

4.6 Discussion

Model for Kip3 sidestepping mechanism

In the 3D stepping and speckle-FLIC gliding assays with Kip3 it was observed that sidestepping is uncoupled from the forward stepping and the probability to sidestep for each forward step (3-9 %) strongly depends on the amount of time it takes to make a forward step (~150-400 ms; Figure 4.1D). To further interpret this

observation, the step dwell time was altered by varying the temperature, thereby effecting all the transition rates in the step cycle simultaneously. Only a marginal change was observed in sidestepping probability (7-8 %) over a range of forward step dwell time (~100-500 ms; Figure 4.2A). This implies that the sidestepping is linked to a specific state in the step-cycle and not to the complete step (all rates are effected by temperature). Increasing the dwell time of the motor in the post-hydrolysis ADP.P_i state by slowing down phosphate release (additional P_i in imaging solution) did not affect the sidestepping probability (Figure 4.2B). However, limiting the ATP concentration led to a correlated increase in the sidestepping probability (8-20 %) with step dwell time (~300-3000 ms) saturating eventually (for dwell times >750 ms; Figure 4.3C). This implies that sidestepping is linked to the ATP waiting state and the following model for the sidestepping mechanism of Kip3 was proposed (Figure 4.7): (i) ATP waiting state [2] is one of the rate-limiting step in Kip3 step-cycle ($t_{\mathbf{waitingATP}} \cong 0.7 \times t_{\mathbf{step(max)}}$), (ii) transition from 2HB conformation to 1HB conformation occurs in ATP waiting state (state [2] to state [2']), and (iii) sidestepping of Kip3 is only possible in 1HB conformation (state [4'] to state [5]).

First, it was hypothesized that the ATP waiting state is one of the rate limiting steps in the Kip3 step cycle at saturating ATP concentrations. Here, it was assumed that Kip3 has a similar stepping mechanism as kinesin-1 and therefore, the step cycle of kinesin-1 was used as reference [81]. In contrast to kinesin-1 (~10-15 ms per forward step), Kip3 spends 10-fold more time for each forward step (140-170 ms), which means that one (or more) step has to be much longer. While the post-hydrolysis ADP.P_i state is rate limiting step for kinesin-1 [80], it was shown that for Kip3 the required longer step cannot be attributed to the P_i release state [1] because only a minor increase (~3%) increase in the dwell time of the forward step was observed with addition of P_i in the imaging solution. Further, it is likely that ATP hydrolysis (state [3], $K_{\mathbf{M}} = 15\,\mu M$) is efficient as in kinesin-1 ($t_{\mathbf{hydrolysis}} \leq 8$ ms [84]) and should not increase the dwell time of the forward step. Finally, while a prolonged dwell time in state [4] cannot be ruled out, an elongation of this state would make the motor vulnerable to premature P_i release followed by MT unbinding [85] (which is contradicted by the high processivity of Kip3 [34, 95]). Considering these points, it can be proposed that ATP binding is rate-limiting, but further biochemical studies to confirm the cycle rates must be done in the future. Still, possible explanations

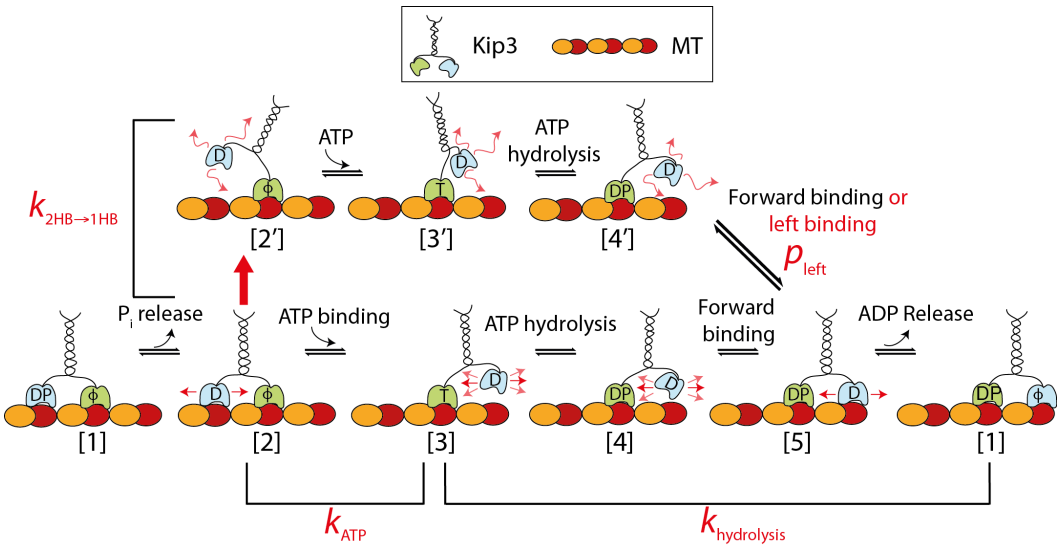

Figure 4.7: Schematic model for Kip3 leftward sidestepping mechanism After completing a step, the motor has released ADP from the leading head and has both heads tightly bound to the MT (1). After P_i release from the trailing head, the interaction of this head with the MT becomes weaker, but both heads are still bound to the MT (2). While waiting for ATP in this two-head bound (2HB) conformation a bifurcation in the pathway can occur: (i) the leading head binds ATP ($k_{\mathbf{ATP}}$) with the motor in the 2HB conformation or (ii) the trailing head unbinds from the MT before ATP binding and the motor transitions to a one-head bound (1HB) conformation (2'). This transition ($k_{\mathbf{2HB\rightarrow 1HB}}$) is nucleotide independent and can explain different sidestepping probability per forward step: (i) If the leading head binds ATP with the motor in the 2HB conformation (2) the trailing head moves forward (3) and ATP hydrolysis ($k_{\mathbf{hydrolysis}}$) induces binding (4→5). Here, the necklinker is restricted and binding is limited to the tubulin dimer directly in front of the bound head (only forward stepping). (ii) If the leading head binds ATP with the motor in the 1HB conformation (2') the trailing head is moved forward (3') and ATP hydrolysis also induces binding (4'→5). However, the necklinker is less restricted and the unbound head can access more binding sites (e.g. forward, leftward, rightward etc.). If we assume, that the most probable alternate binding site is directly to the left of the bound head [92], we can add a probability $p_{\mathbf{left}}$ for switching to the protofilament on the left. Since both pathways are possible at physiological conditions the effective sidestepping probability is reduced because the transition from the 2HB to 1HB conformation is less likely than ATP binding ($k_{\mathbf{2HB\rightarrow 1HB}} = k_{\mathbf{ATP(max)}}/4$). However, with lowering ATP concentrations the 1HB state becomes more likely leading to an increased effective sidestepping probability. Consequently, the effective sidestepping probability saturates (should approach $p_{\mathbf{left}}$) at limiting ATP concentration where the 1HB state (2') is predominantly occupied. Here T denotes ATP, D denotes ADP, DP denotes ADP plus phosphate, and Φ denotes no nucleotide. Loose binding or diffusion is represented by red arrows.

for the slow kinetics of ATP binding and efficient ATP hydrolysis involve the presence of structural elements in the motor domain that block the ATP binding site (similar to kinesin-5, [166]) and/or front head gating, where rearward strain slows nucleotide binding to the front head [75, 167]. Without further data, a more detailed description is not possible at this point and for simplicity, it was assumed that ATP binding can be estimated with the measured Michaelis-Menten constant from control stepping assays ($k_{\mathbf{ATP}}([ATP]) = 1/(t_{\mathbf{step}}([ATP]) - t_{\mathbf{rest}})$, $t_{\mathbf{step}}([ATP]) = t_{\mathbf{step(max)}} \times ([ATP] + K_{\mathbf{M}})/[ATP], K_{\mathbf{M}} = 15\,\mu M$; Figure 4.4).

Second, it was suggested that Kip3 binds ATP in either a 2HB or 1HB conformation with the leading head tightly bound to the MT lattice without nucleotide. Here, the trailing head (with ADP bound) is either weakly interacting with the MT (state [2]) or remains freely diffusive (within a space confined by the motor geometry; state [2']). The suggested nucleotide independent transition from a 2HB conformation to 1HB conformation has been previously reported for kinesin-1 [81, 84, 161–164] if the ATP waiting state was substantially long (limiting ATP concentrations). Since it is assumed that Kip3 spends most of the step cycle in the ATP waiting state (~140-170 ms), which is more than 20-folds longer than for kinesin-1 (<8 ms, (Mickolajczyk et al., 2015)), the transition from the 2HB to the 1HB conformation would not only occur at limiting ATP concentrations but already at physiological ATP concentrations. Therefore, ATP can bind in both the 2HB and 1HB conformation at physiological conditions while ATP binding predominantly occurs in the 1HB conformation at limiting ATP concentrations.

Third, it was proposed that sidestepping probability is enhanced if Kip3 binds ATP in the 1HB conformation. During each forward step, ATP binding and hydrolysis in the leading head propels the trailing head forward due to neck linker docking [72], which can then diffusively search for the next tubulin-binding site [168]. Forward stepping is therefore a combination of a powerstroke and a Brownian ratchet mechanism [169]. Typically, inter-head tension is stored in the neck linker domain when the motor is in a 2HB conformation [158, 170, 171]. If the trailing head releases before the powerstroke, elastic energy is dissipated, which leads to a weaker powerstroke in the 1HB conformation as compared to the 2HB conformation. Therefore, the position of diffusing head before binding to the MT could be different (states [4] and [4']). Additionally, the position of diffusing head can also be effected due to partial (or different) neck-linker docking in the 1HB

conformation. Consequently, the binding rate for different tubulin binding sites could be affected by the position of the diffusing head. Furthermore, the accessible tubulin binding sites will most likely depend on the reach of the diffusing head, which strongly relates to the structure of the motor neck. Here, Kip3 (17aa) has a longer neck linker than kinesin-1 (14aa) [92] and the first heptad of the neck coiled-coil is predicted to be loosely coiled [134] (see Discussion in Chapter 3). This provides the unbound Kip3 motor domain the capacity to reach tubulin binding sites on the neighboring protofilaments. Without high-precision tracking data binding rates to the specific binding sites (for 2HB and 1HB conformation) cannot be resolved. Therefore, the stepping mechanism was simplified with the assumptions that Kip3 can only sidestep when binding ATP in the 1HB conformation and the only possible alternative binding site (apart from the forward binding site) is directly on the left of the bound head (which is the most likely alternative binding site [92], as discussed in Chapter 3). In summary, the proposed model of the Kip3 step cycle involves a bifurcation in the ATP waiting state (Figure 4.7) with a nucleotide independent transition from a 2HB conformation to a 1HB conformation. The enhanced probability to switch to the leftward protofilament in the 1HB conformation explains the observations made in 3D stepping and speckle-FLIC gliding assays (under varying ATP concentrations; Figure 4.2C). Here, longer dwell times directly refer to longer ATP waiting states and thus a greater likelihood to transition to the 1HB conformation, increasing the effective sidestepping probability. Numerical simulations based on the model (Figure 4.3B) are in good agreement with the experimental observations when it is assumed that at saturating ATP concentrations Kip3 transitions from a 2HB to a 1HB conformation once every 4 steps ($k_{\mathbf{2HB\rightarrow 1HB}} = k_{\mathbf{ATP(max)}}/4$) and the sidestepping probability in the 1HB conformation ($p_{\mathbf{left}}$) is 18 %.

Sidestepping probability can be regulated by MT modification

If the proposed model can describe the sidestepping mechanism of Kip3 (Figure 4.7) the interaction of the trailing head with the MT (state [2]) would play a crucial role. Reducing this interaction and thereby increasing the transition rate from the 2HB to the 1HB conformation ($k_{\mathbf{2HB\rightarrow 1HB}}$) should increase the sidestepping probability. Indeed, a shorter rotational pitch was observed in speckle-FLIC gliding assays with subtilisin treated MTs, at similar gliding speeds (Figure 4.4C). Here,

the digestion of the MT e-hook by subtilisin leads to a diminished electrostatic interaction between the MT lattice and structural elements in the kinesin-8 motor domain (loop 2 and loop 12 [134, 135]) in the presence of ADP. Control experiments with subtilisin treated MTs show a 10-fold reduction in landing rate and interaction time of Kip3 motors (in 1mM ADP; Figure 4.4A), indicating that the increased sidestepping rate could indeed be caused by a weakened interaction of the motor with the MT. Again, numerical simulations and experimental data with subtilisin treated MTs are in good agreement (Figure 4.4) if a 2-fold higher transition rate ($k_{\mathbf{2HB\rightarrow 1HB}} = k_{\mathbf{ATP(max)}}/2$) than with normal MTs is assumed. In conclusion, the observations suggest that post-translational modifications of MTs could affect the sidestepping mechanism of Kip3 without the need for motor regulatory factors.

General strategy for kinesin motors to circumvent roadblocks

Finally, it was explored if the proposed sidestepping mechanism is specific to Kip3 or whether it can be generalized to other processive kinesin motors. Most torsional studies on plus-end directed kinesins [89, 92, 98, 172] including a kinesin-1 mutant with a large flexible insert at the neck-linker [98] reveal a left-handed trajectory around MTs. Since all these motors have a longer neck-linker than wt-kinesin-1 (17-18aa long compared to 14aa [92, 173]) the sidestepping probability could be dependent on the neck-linker length. In addition, while the transition from the 2HB to the 1HB conformation ($k_{\mathbf{2HB\rightarrow 1HB}}$) could be similar between various kinesin motors [84], the ATP waiting state could vary and the transition to the 1HB conformation is not likely if the ATP binding rate is high ($k_{\mathbf{ATP}} \gg k_{\mathbf{2HB\rightarrow 1HB}}$). Therefore, both of these factors have to coincide in order to observe sidestepping. This can be seen in the experimental data from speckle-FLIC gliding assays at various ATP concentrations with wt-kinesin-1 and kinesin-$1_{\mathbf{+DAL}}$ mutant (3aa extended neck-linker). Almost no sidestepping was observed for kinesin-1 at 1μM ATP, but the sidestepping probability increased to ~1.3 % for kinesin-$1_{\mathbf{+DAL}}$ (one sidestep per 77 forward steps). If it is assumed that at this ATP concentration both motor constructs only bind ATP in the 1HB conformation, the data would suggest a probability $p_{\mathbf{left}}$ of less than 0.1 % for kinesin-1 and 1.3 % for kinesin-$1_{\mathbf{+DAL}}$. Based on this observation it can be proposed that all processive kinesin have an alternate pathway in the step cycle where they could transition to a 1HB conformation. It is likely this transition occurs stochastically if the ATP waiting

state becomes rate limiting or can be forced if the motors encounter a roadblock at the forward binding site. Directly in front of a roadblock, motors would wait in the 1HB conformation, most likely after ATP hydrolysis, but the unbound head cannot attach to the forward binding site. Because kinesin motors with short neck-linkers cannot reach any other binding site they would pause and detach at the roadblocks [46, 57, 96, 111], while other kinesins with longer neck-linkers could switch the protofilament in order to circumvent them (kinesin-2, [58, 110]).

In conclusion, it seems that Kip3 has evolved an elaborate mechanism to switch protofilaments in order to avoid any roadblocks that it encounters along the MT lattice and to negotiate traffic jams at MT ends [112]. Directed sidestepping incorporated within the motor step cycle would enable the motor to reach the end of crowded MTs in an energy efficient manner. In the next chapter, the impact of static roadblocks on Kip3 motility was studied in order to understand the precise roadblock circumvention strategy employed by the motor.

Acknowledgements

The MATLAB code for the Kip3 sidestepping mechanism was written by Dr. Felix Ruhnow.

CHAPTER 5

Influence of roadblocks on Kip3 motility

In order to investigate the roadblock (RB) circumnavigation strategy employed by the Kip3, motility assays are performed on RB-decorated MTs. Rigor binding kinesin-1 mutants are employed as static RBs. Observations made in Kip3 driven speckle-FLIC gliding assays with RB-decorated MTs are consistent with the sidestepping model which just accounts for left-biased sidestepping. However, single molecule observations on RB-decorated suspended MTs suggest that there is also an unbiased diffusive component in the motor motility induced by RBs. Further, Kip3 stepping assays on RB-decorated surface-immobilized MTs reveal that the unbiased diffusive component depends on the ionic strength of the buffer and gets screened in the normal (i.e. high salt) assay conditions. Based on the observations, it is proposed that Kip3 has a dual-mode strategy to avoid RBs. Upon encountering a RB, the motor has a default strategy to circumnavigate it by left-biased sidestepping which occurs within the step cycle. However, the motor also has a back-up strategy, that becomes prominent at high RB densities, which involves switching out of the step cycle into an unbiased diffusive state.

5.1 Rigor binding kinesin-1 can be used as static MT roadblocks (RBs)

In order to understand how Kip3 circumnavigates RBs, the motility of Kip3 was explored on MTs decorated with RBs. For such hindered motility studies, it is necessary to identify MT RBs with suitable properties. An ideal MT RB would bind irreversibly on the MT lattice, blocking precisely the tubulin-binding site of kinesin motor domains. Ideally, one would first study how kinesin motility is affected by ideal RBs before extending the study to RBs with other biophysical characteristics. In Schneider et al. [57], a rigor-kinesin-1 mutant was generated to study the impact of RBs on kinesin-1 motility [57]. This kinesin-1 mutant (shortened dimeric rat kinesin-1 rkin430 with or without a GFP tag on the C-terminal end) has a T93N point mutation in the Walker A domain which inhibits ATP binding in the motor head [174], thereby rendering the motor domain to permanently remain in the nucleotide-free state (i.e. strong binding with MT). TIRF microscopy in the stepping assay geometry on GFP-labeled rigor-kinesin-1 revealed that these motors bound statically to the MT lattice with a very low MT dissociation rate ($\sim$0.003 s^{-1}) [57]. Their properties are therefore ideal to study the scenario of Kip3 motors encountering permanently blocked sites in the MT lattice.

One concern with extending the RB assays performed on kinesin-1 to Kip3 is the significant difference in the ionic strength of the assay buffer used for *in vitro* assays performed on the two motors. In most previous studies, kinesin-1 motility assays have been performed in BRB80 (comprised of 80 mM Pipes; referred to as kinesin-1 buffer conditions) while Kip3 motility assays have been performed in BRB80 + 112.5 mM KCl (referred to as Kip3 buffer conditions). Under Kip3 buffer conditions, it was observed that rigor-kinesin-1 binds statically to the MT lattice, but the MT association rate is $\sim$5 times lower and the MT dissociation rate is $\sim$30 times higher in comparison to kinesin-1 buffer conditions (values not quantified rigorously in current work). In previous RB assays for kinesin-1, rigor-kinesin-1 RBs were incubated with surface-immobilized MTs for a few minutes after which the free rigor-kinesin-1 was washed out of solution. Since the MT dissociation rate is low in kinesin-1 buffer conditions, almost no RBs detach even after a 20 min waiting period. Therefore, when performing kinesin-1 stepping assays on such RB-decorated MTs the RB density effectively remained constant over time. Under

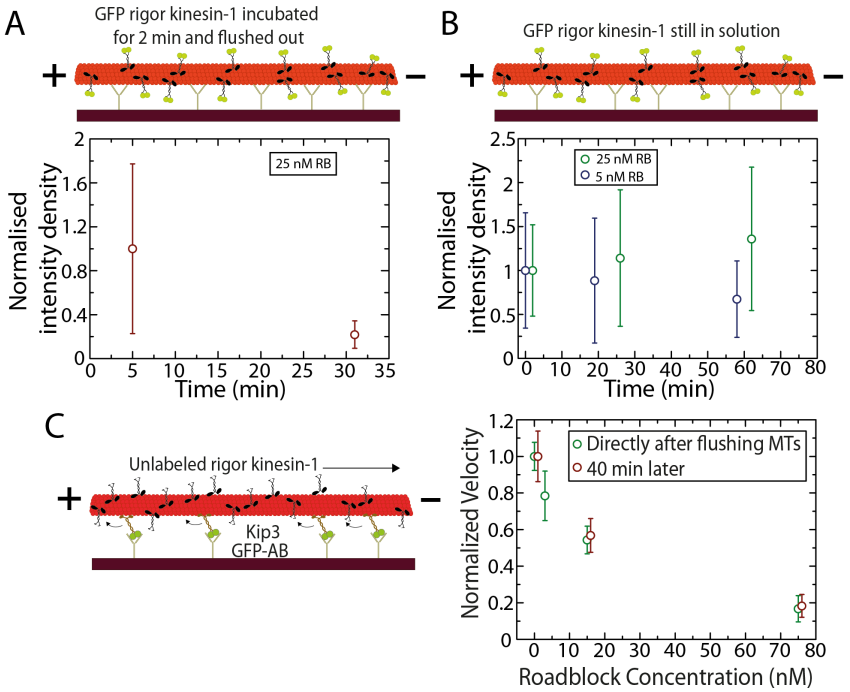

Figure 5.1: Characterization of rigor-kinesin-1 as static roadblocks. (A) Surface-immobilized MTs were incubated with 25 nM GFP-labeled rigor-kinesin-1 solution for 2 min after which the free rigor-kinesin-1 was washed out. The normalized intensity density of the GFP-labeled rigor-kinesin-1 on MTs is plotted as a function of time. The significant drop in the normalized intensity density indicates that the rigor-kinesin-1 motors get off the MTs over time. **(B)** Surface-immobilized MTs were incubated with 25 nM (green) and 5 nM (blue) GFP-labeled rigor-kinesin-1 solution for 2 min and the free rigor-kinesin-1 was not washed out. The normalized intensity density of the GFP-labeled rigor-kinesin-1 on MTs is plotted as a function of time. The effective density of rigor-kinesin-1 motors remains constant over time. **(C)** Kip3 gliding assays were performed with unlabeled rigor-kinesin-1 decorated MTs (with free rigor-kinesin-1 in solution) and the normalized gliding velocity (green) is plotted as a function of rigor-kinesin-1(RB) concentration. The gliding velocity reduces with increasing RB densities on the MT surface. The gliding velocity is impacted by RBs to the same extent over time (red) indicating that the effective RB density on MTs remains constant.

Kip3 buffer conditions, the MT dissociation rate of rigor-kinesin-1 is significantly higher and thus the effective RB concentration would reduce over time. Indeed, on incubating 25nM of GFP-labeled rigor-kinesin-1 under Kip3 buffer conditions, ~25 min after washing out the free rigor-kinesin-1, the RB density on the MTs reduced to ~5 % of the initial density (Figure 5.1A). Therefore, this strategy is not ideal to perform Kip3 motility assays as the effective RB density reduces rapidly.

In order to overcome this issue, rigor mutants were not washed out, but kept in the imaging buffer while imaging. In control experiments under Kip3 buffer conditions, surface-immobilized MTs incubated with 25 nM (or 5 nM) GFP-labeled

rigor-kinesin-1 had a relatively constant RB density over time (for >1 h; Figure 5.1B). Using this strategy, Kip3-mfGFP driven MT gliding assays were performed for varying concentrations of unlabeled rigor-kinesin-1 (0 nM, 3 nM, 15 nM and 75 nM). The rigor-kinesin-1 concentration in the imaging solution only provides a qualitative information regarding the RB density on the gliding MTs because: (i) The rigor-kinesin-1 motors are unlabeled. GFP-labeled rigor-kinesin-1 cannot be used in these assays since the Kip3 motor are also labeled with GFP and are bound to the surface via GFP antibodies. (ii) The density of MTs vary from assay to assay. For the same concentration of rigor-kinesin-1 in the imaging solution, a higher density of MTs leads to a lower RB density on the MTs. Regardless, on increasing the density of RBs the velocity of MTs gliding on Kip3 reduced (Figure 5.1C), similar to observations made in previous RB studies on kinesin-1 [46]. Further, the gliding velocity was rather constant even after 40 min for different RB decoration densities (Figure 5.1C), indicating that the effective RB density on MTs remained constant over time. Therefore, this RB decoration strategy could be employed in the motility assays established previously in the present work, to study the 3D motility of Kip3 on RB-decorated MTs.

5.2 Kip3 driven RB-decorated S-MTs gliding perform left-handed rotations

The speckle-FLIC approach (see Chapter 2) was used to obtain rotational information from RB-decorated S-MTs gliding on surface-immobilized Kip3 motors (Figure 5.2A). Similar to observations made in Figure 5.1C, S-MTs in the presence of 15 nM (or 60 nM) unlabeled rigor-kinesin-1 had gliding velocities significantly lower than S-MTs without RB decoration (slowing down to 5-15 nm/s for 60 nM RB decoration in comparison to ~50 nm/s on RB free MTs). Also, the RB-decorated S-MTs performed clear rotations with pitches considerably shorter than S-MTs with no RBs. Figure 5.2B shows the measured sidestepping probability of each gliding MT (with no RBs, 15 nM RBs or 60 nM RBs; qualitative indicator of RB density) in dependence of the step dwell time. Similar to the observation made at limiting ATP conditions (Figure 4.2C in Chapter 4), the sidestepping probability increased with the dwell time per forward step eventually saturating at 15-20 % per forward step (Figure 5.2A).

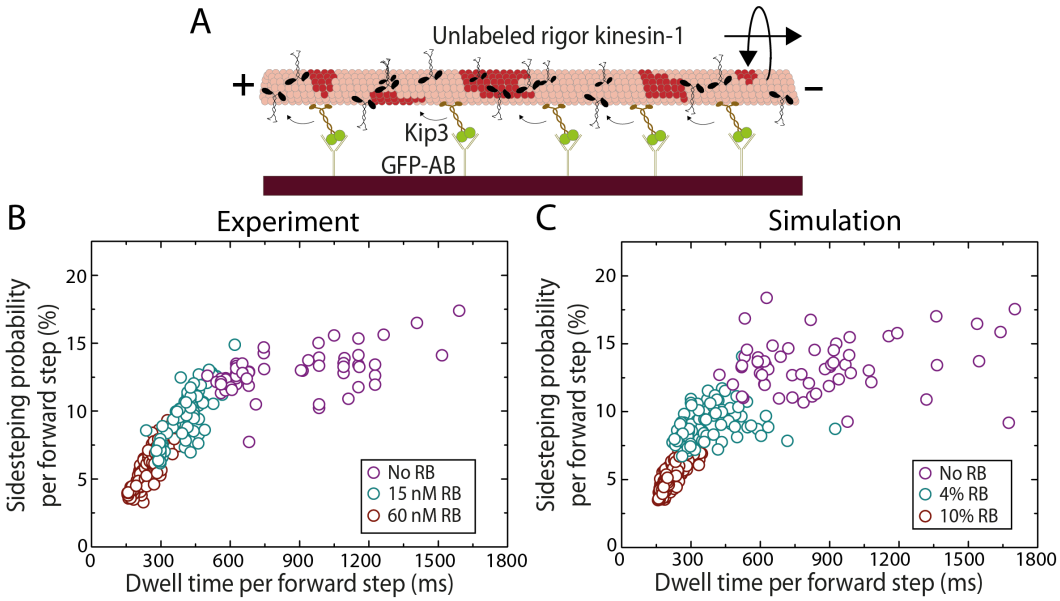

Figure 5.2: Left-biased sidestepping explains rotational motion of RB-decorated S-MTs gliding on Kip3. (A) Illustration of the experimental geometry. Kip3 driven speckle-FLIC gliding assays were performed on rigor-kinesin-1 decorated MTs. **(B)** Rotational motion of rigor-kinesin-1 decorated S-MTs gliding on Kip3-mfGFP was evaluated for different RB densities. The estimated sidestepping probability per forward step (calculated as discussed in the Supplementary information) is shown in dependence of the dwell time per forward step for MTs decorated with no RBs (red circles; N=315), 15 nM RBs (green circles; N=99) and 60 nM RBs (purple circles; N=61). On increasing the RB density on MTs, the dwell time per forward step increases along with correlated increase in the sidestepping probability with eventual saturation at 15-20 %. **(C)** The simulated sidestepping probability per forward step is shown in dependence to the dwell time per forward step for gliding events with no RB decoration (red circles; N=300), 4 % RB decoration (green circles; N=100) and 10 % RB decoration (purple circles; N=60). The simulation provides results similar to the experiments in **A** assuming the same parameters as used for the simulation in Chapter 4.

To understand the observations made in Figure 5.2B, the simulations introduced in Chapter 4 (Section 4.3) were extended to account for RBs hindering the motor path. In the simulation, a certain percentage ($r_{\mathbf{RB}}$) of tubulin-binding sites were blocked (thereby representing a site-specific RB) for the simulated Poisson steppers. On encountering these blocked sites the stepper would pause (in a state comparable to the ATP waiting state) with a possibility to transition to a 1HB state ($k_{\mathbf{2HB\rightarrow 1HB}}$), thereby having a probability $p_{\mathbf{left}}$ to make a leftward sidestep. Assuming the same parameters as used for simulations on MTs without RBs (Table 4.1, Chapter 4), a good agreement of the numerical simulation (Figure 5.2C) with the experimental data could be achieved for $r_{\mathbf{RB}}$ of 4 % and 10 % corresponding to 15 nM RBs and 60 nM RBs in the experiments (Figure 5.2C). The simulation results have a

larger variance than the experimental results due to greater stochasticity of single Poissons steppers in comparison to multi-motor gliding events (presumably the variations in motility averages out in an ensemble multi-motor system). Based on the simulation, it is interesting to note that a RB encounter event can be equated with a prolonged ATP waiting state for a particular step and $p_{\mathbf{left}}$ for Kip3 motors does not increase in response to the RB encounter.

5.3 Kip3-QDots have irregular left-biased tracks on RB-decorated MTs

3D stepping assays (described in Chapter 3) were performed to observe the 3D motility of single Kip3-mfGFP motors on RB-decorated suspended MTs (Figure 5.3A). Kip3-QDots moving along suspended MT at 15nM unlabeled rigor-kinesin-1 were slower (23.4 ± 8.0 nm/s; N=43) and had shorter track lengths. As seen for the example Kip3-QDot track in Figure 5.3B (projected angle plot in Figure 5.3C; further example Kip3-QDot tracks can be seen in Figure S7), Kip3 motors have a left-handed helical trajectory even on a MT lattice decorated with RBs. The cumulative angles versus travelled distance for the 43 evaluated Kip3-QDot events indicated that there was a clear preference in directionality towards the left (Figure 5.3D). However, inconsistent with the results obtained from speckle-FLIC gliding assays with RB-decorated MTs, the leftward sidestepping probability did not change substantially in presence of RBs (slope = 130 ± 120 °/µm for MT with RBs in comparison to slope = 130 ± 40 °/µm for MT without RBs). Further, the motion of the Kip3-QDot events was more erratic (in comparison to motion on MTs without RBs) with no consistent rotational pitch (see example tracks in Figure 5.3B, 5.3C and supplementary Figure S7). To further understand this motility feature 3D stepping assays were performed using higher incubation concentrations of RB (60 nM). At such high RB decoration densities Kip3-QDot tracks were too short and it was difficult to obtain events with runlength >2 µm. This suggests that while Kip3 motors are able to circumnavigate MTs decorated with low (or medium) density of static RBs, their motion is severely hindered on heavily crowded MTs.

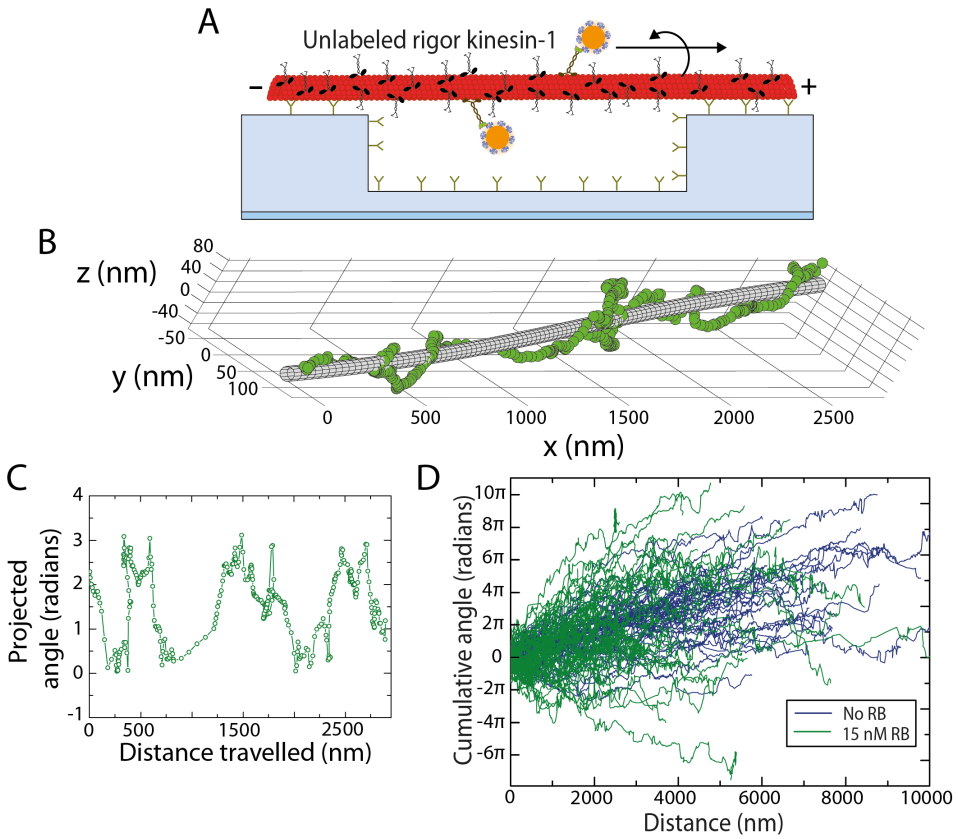

Figure 5.3: 3D tracks of Kip3-QDots on RB-decorated suspended MTs reveal erratic left-biased motion. (A) Illustration of the experimental geometry. Kip3-QDots were imaged in 3D, using Parallax, on rigor-kinesin-1 decorated S-MTs. **(B, C)** The 3D tracking data around the fitted tube and plot of the angle projected by the Kip3-QDot to the fitted path with respect to the linear distance travelled is shown for an example track on a MT decorated with 15 nM rigor-kinesin-1 RBs. **(D)** The cumulative angle plots for all 43 events on MTs decorated with rigor-kinesin-1 RBs (green) along with 50 events on MTs without RBs (blue). While Kip3 motors have an average left-handed helical path around RB-decorated MTs (slope of cumulative angle 130 ± 120 °/µm), the motion is considerably more irregular than on MTs without any RBs.

5.4 At low ionic strength, processivity of Kip3 is not impacted by RBs

In 3D stepping assays, it was observed that the runlength of Kip3 motors reduced upon increasing the number of RBs on the MT lattice. Characterization of the percentage of motors that reached the MT end at varying concentrations of RBs can be performed in conventional stepping motility assays (where the MTs are surface-immobilized). These experiments would provide a simpler approach (in comparison to 3D stepping assays) to quantify the motility efficiency of Kip3 motors.

The GFP label on the motor is not optimal for quantifying motor processivity since it has a low fluorescence lifetime (motor runlengths would be underestimated due to photobleaching). Therefore, Kip3 motors were coupled to Atto647N-labeled nanobodies (which bind specifically to GFP) which have far superior fluorescence characteristics over GFP (excellent fluorescence quantum yield with high photostability) making them highly suitable for studying slow motors with long runlengths and MT interaction time.

TIRF microscopy measurements of Kip3-mfGFP (labeled with Atto647 nanobodies) stepping along surface-immobilized MTs was carried out at varying concentrations of unlabeled RBs on the MT lattice. While most Kip3 motors reached the MT ends at very low or no RB decoration, the runlengths were substantially shortened for MTs decorated with higher densities of roadblocks with almost no motors reaching the MT end (Figure 5.4A). Interestingly, unlike the speckle-FLIC gliding assays and 3D stepping assays performed earlier, the motor velocity was not affected much, indicating that at these experimental conditions the motors do not pause upon encountering RBs.

In 3D stepping assays, a diffusive component was observed in Kip3 motility on RB-decorated MTs. Since diffusive motility is likely due to electrostatic interaction between the motor and the MT lattice, it is possible that this interaction is screened out in a buffer with high salt. Therefore, conventional stepping motility assays of Kip3 were performed under kinesin-1 buffer conditions (BRB80 with no additional salt), at varying concentrations of unlabeled RBs on the MT lattice. It was observed that the Kip3 stepping velocity goes down with the density of RBs on the MT, reducing to ~3 nm/s at a high RB decoration density (in comparison to ~30 nm/s on MTs without RBs) (Figure 5.4B). Qualitatively, the tracks appear irregular, indicating a diffusive component in the Kip3 stepping motility that gets enhanced on increasing the RB concentration. Interestingly, though the RB decoration slows down the motor motility, it has a negligible impact on runlengths, with average MT interaction times increasing to >30 min on MTs with high RB decoration (to place this into context, the MT interaction time is <1 s for kinesin-1 on RB-free MTs [57]) . Therefore, in kinesin-1 buffer conditions, Kip3 is superprocessive even on densely crowded MTs.

While this preliminary study reveals interesting cues regarding the motility strategy employed by Kip3 motors, most of the observations are qualitative. A thorough

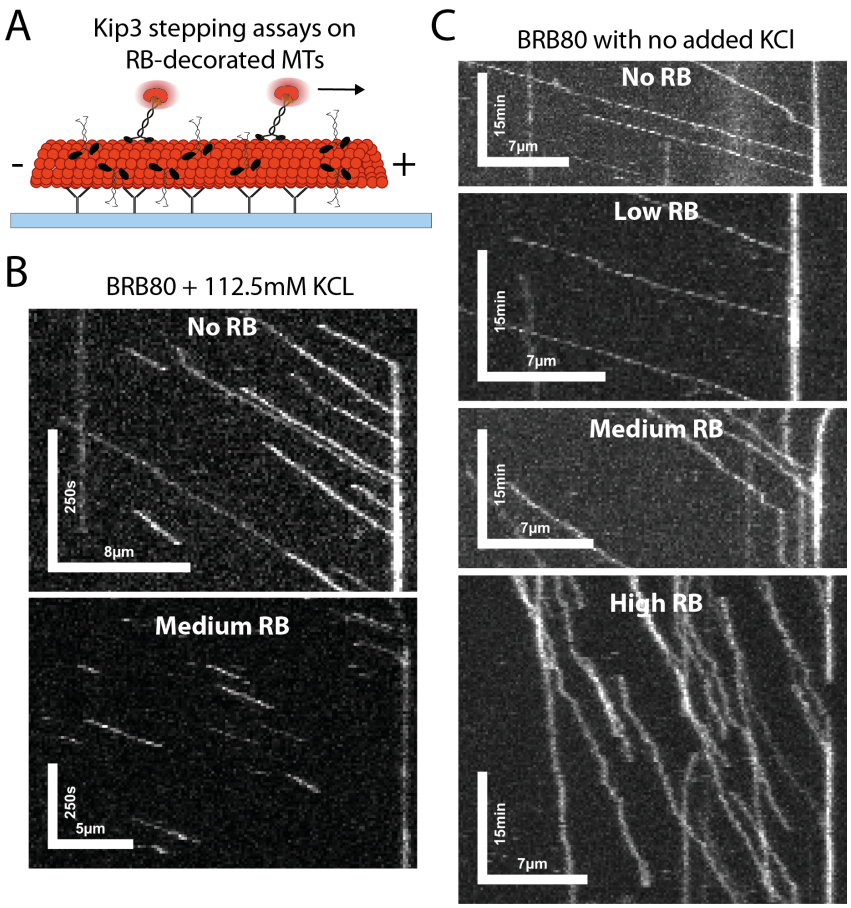

Figure 5.4: Kip3 processivity is not hindered by RBs in a buffer with low ionic strength. **A** Illustration of the experimental geometry. Conventional stepping assays were performed for Kip3 (labeled with Atto647 nanobody specific to GFP) in different ionic strength buffers on MTs decorated with unlabeled rigor-kinesin-1 RBs. **(B)** Example kymographs for Kip3 motility under normal assay conditions (BRB80 + 112.5 mM KCl) on MTs decorated with no RBs (upper kymograph) and medium density of RBs (lower kymograph). RBs have little or no influence on Kip3 stepping velocity but significantly reduces runlength and MT interaction time. Note: The scale bars are different due to different image acquisition rates. **(C)** Example kymographs for Kip3 motility under low ionic strength assay conditions (BRB80 with no excess salt) on MTs decorated with no RBs (1st kymograph), low RB density (2nd kymograph), medium RB density (3rd kymograph) and high RB density (4th kymograph). Kip3 stepping velocity reduces with increase in RB density. However, there is no apparent decrease in runlengths leading to MT interaction times >30 min. In all these experiments, the information regarding the density of RB decoration is qualitative since the RBs were unlabeled.

study should be performed in the future where the RB density is characterized quantitatively, in order to determine how the motility parameters (velocity, runlength and MT interaction time) of the Kip3 motors is affected by the average lattice spacing between RBs (under different salt conditions). It will also be insightful to perform the 3D motility studies on Kip3 in kinesin-1 buffer conditions.

5.5 Discussion

In this chapter, Kip3 motility assays were performed on MTs decorated with rigor-kinesin-1 motors which acted as static RBs with a low MT dissociation rate (0.1-0.01 s^{-1}).

In Kip3 driven gliding rotation assays using RB-decorated MTs, a correlated reduction in the gliding velocity with increase in RB density was observed. Further, the dependence of the calculated sidestepping probability on the dwell time per forward step (Figure 5.2A) was observed to be similar to the one obtained for gliding rotation assays (on MTs without RBs) at varying ATP concentrations (see Figure 4.2C in Chapter 4). Simulations to explain the sidestepping behavior of Kip3 motors at limiting ATP conditions could explain the observed rotation data for speckle-FLIC gliding assays with RB-decorated MTs (Figure 5.2B). According to the sidestepping model proposed in Chapter 4, Kip3 motors can perform leftward sidesteps only if the motor transitions from a 2HB conformation to a 1HB conformation which occurs in the rate-limiting ATP waiting state. However, in case of the RB-decorated MTs, the slowdown in velocity is most likely not due to the motor waiting in the ATP waiting state (state [2] in Figure 5.5) but in the post-hydrolysis ADP.P_i state (state [4]) in Figure 5.5). It can be proposed that the transition from a 2HB conformation to a 1HB conformation for Kip3 motors can also occur in the post-hydrolysis ADP.P_i state (state [4]→state [4']; Figure 5.5) when the motor encounters a roadblock in the forward tubulin-binding site. Upon transitioning to the 1HB conformation, the motor has a probability $p_{\mathbf{left}}$ to perform directed leftward sidesteps which would enable the motor to circumnavigate RBs. Interestingly, $p_{\mathbf{left}}$ remains constant at 15-20 % irrespective of the density of RBs on MTs (as can be seen from the saturation of the sidestepping probability in Figure 5.2). This could imply that when the forward binding site is blocked, the motor only has a 15-20 % probability to circumnavigate RBs by directed leftwards sidestepping. This poses the question of whether the motor waits for the RB to dissociate in a paused state, switch to a diffusive state, or dissociate itself when not performing the leftward sidestep. To explore this question, 3D single molecule measurements were performed.

In Kip3 stepping assays on RB-decorated suspended MTs, the following was observed (see Figure 5.3, S7): (i) Kip3 motors were slower and the tracks had an overall left-handed trajectory; (ii) While there was a general left-handed bias,

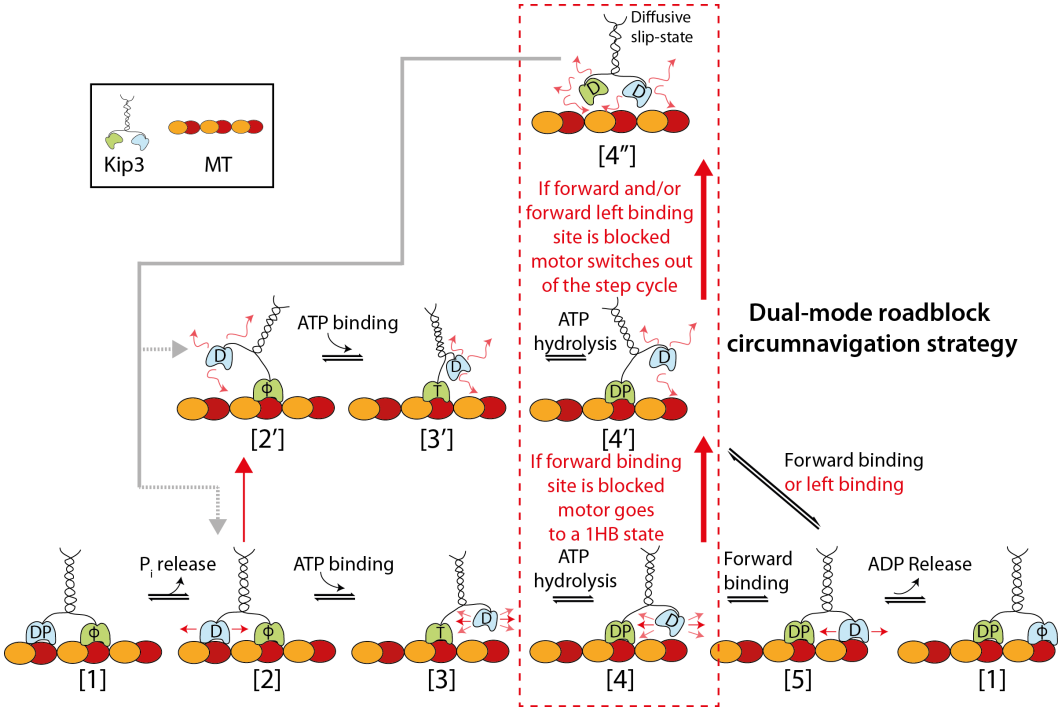

Figure 5.5: Dual-mode roadblock circumnavigation strategy employed by Kip3. In the proposed model for Kip3 step cycle discussed in Figure 4.6, there is a bifurcation in the pathway when the motor waits for ATP, where the motor could transition from a 2HB conformation (state[2]) to a 1HB conformation [2']. In the 1HB conformation the motor has a probability to perform a leftward sidestep. Here, it was proposed that the motor can make a similar transition from a 2HB conformation to a 1HB conformation in the post-hydrolysis ADP.P_i state ([4]→[4']) when it encounters a RB in the forward tubulin-binding site. Upon switching to the 1HB conformation [4'], the motor has a probability to perform a leftward sidestep to circumnavigate the RB without having to switch out of the step cycle. However, the motor also has a probability to switch out of the step cycle completely to enter a diffusive state [4''] where it can circumnavigate the RB by unbiased diffusive motion. The motor can switch back to the step cycle stochastically at a different tubulin-binding site in the ATP waiting state ([2] or [2']). The switch to the diffusive state becomes even more prominent in case of heavy RB decoration where often the forward as well as the leftward tubulin binding sites are blocked. Here T denotes ATP, D denotes ADP, DP denotes ADP plus phosphate, and Φ denotes no nucleotide. Loose binding or diffusion is represented by red arrows.

the motion of Kip3 motors on RB-decorated MTs was rather erratic; (iii) The runlengths of the tracks was reduced significantly with an increase in RB density. These observations imply that upon encountering RBs, Kip3 can either perform directed leftward sidesteps (as discussed earlier), undergo short bursts of unbiased diffusion or detach from the MT lattice. This would suggest that in the post-hydrolysis ADP.P_i state (state [4]) the motor has a probability to switch out of the step cycle, which would occur due to P_i release from the tethered head, leading to

both heads being ADP bound (state [4"] in Figure 5.5). In this state, the motor can diffuse on the MT lattice [165] and/or is vulnerable to detach (as shown for kinesin-1 in [85]), which would explain the observed results

To characterize the motility parameters (velocity, runlength and MT interaction time) of Kip3 motors as a response to RB density, stepping motility assays were performed on RB-decorated surface-immobilized MTs. While the results are preliminary and no quantitative characterization of the RB density was performed, it was evident that the run length and MT interaction time of the Kip3 motors went down with the increase in RB density (as previously observed in 3D stepping assays; Figure 5.4A). Interestingly, contrary to the stepping motility assays on RB-decorated suspended MTs, there was no (or relatively small) slowdown in the Kip3 stepping velocity as a response to RBs. It is possible that in the stepping assays on RB-decorated suspended MTs, only the Kip3-QDot tracks with mutiple Kip3 per QDot were selected for analysis (since all tracks with single Kip3 per QDot were screened due to short runlengths; see selection criteria for Kip3-QDot tracks in Chapter 3), resulting in the observed slowdown in velocity. Therefore, upon encountering RBs, Kip3 motors either undergo premature detachment or make directed leftward sidesteps (yet to be verified conclusively) and have no significant pause state (as observed for kinesin-1 [46, 57, 111]) and/or diffusive state. Further experiments must be performed to resolve the conflicting observations and understand how the multiple motor geometry would make the Kip3 driven motility slower upon encountering RBs.

Again, contradictory to the 3D suspended MT assays, single Kip3 motors in conventional RB stepping assays had no evident diffusive component in their motility. This suggests that while there might be a minor diffusive component in Kip3 motility, it only becomes apparent when more than one Kip3 motor is interacting with the MT lattice simultaneously. Since the ionic strength of the buffer used for Kip3 motility assays is high (Kip3 buffer conditions) it is possible that the diffusive interaction of the motor is screened out. Therefore, conventional stepping assays were performed on RB-decorated surface-immobilized MTs using a buffer with reduced ionic strength (kinesin-1 buffer conditions). Under these conditions, it was observed that on increasing the RB decoration on MTs (i) the motor velocity slowed down (up to 10 times slower at the highest employed RB densities), (ii) the motility became more irregular (qualitative observation) and (iii)

runlength did not get affected while MT interaction time increased (>30 min at the highest employed RB densities). This revealing set of observations confirm that Kip3 can indeed switch to a diffusive state in order to navigate RBs when the RB density becomes significantly high. As suggested earlier, this switch possibly occurs in the state [4] or state [4'] (see Figure 5.5) when the trailing motor-head cannot bind to the forward (or leftward) tubulin-binding sites since they are blocked by RBs. This diffusive state may be the slip-state observed in a previous force study on Kip3 [137] and would also explain the unbiased side-stepping induced by sideward forces on Kip3, as observed by Bugiel et al. [155]. Switching out of the step cycle into an unbiased diffusive state would allow Kip3 motors to circumnavigate RBs more efficiently [175]. Once in the diffusive state, the motor would stochastically switch back into the step cycle at a different tubulin-binding site when ADP release is triggered in one of the two diffusive ADP bound heads. Further studies are necessary to understand what prevents spontaneous MT triggered ADP release in the motor heads in order to keep the motor in the diffusive slip-state. Studies on a Kip3 analog indicates interaction of the tail domain with either the motor domain and/or the MT lattice might be involved in sustaining the slip-state [176].

All previous *in vitro* studies on Kip3 have been performed in BRB80 + 112.5 mM KCl, even though the ionic strength of the physiologically relevant buffer is close to that of BRB80. The buffer conditions with high ionic strength was possibly chosen in these studies due to the motor motility being slower (~30 nm/s in BRB80 in comparison to ~50 nm/s in BRB80 + 112.5 mM KCl) and irregular in BRB80 (due to the diffusive component in the motility). Interpretation of the results in the previous chapters would have been difficult if the diffusive component in Kip3 motility was more prominent. Further, one could speculate that the transition rate $k_{\mathbf{2HB \rightarrow 1HB}}$ (to transition from state[2] to state[2']; see Figure 5.5) is much lower in low ionic strength buffers, since this transition is dependent on the electrostatic interaction of the motor head with the MT lattice (as evident from the experiments performed on subtilisin-treated MTs; see Figure 4.4 in Chapter 4). It would be interesting to perform Kip3 stepping assays on suspended MTs in BRB80 to check if the motors maintain a left-handed helical trajectory in low ionic strength buffers. It is possible that in a physiologically relevant buffer, Kip3 seldom transitions to a 1HB conformation (where leftward sidestepping becomes a possibility) unless it is compelled to do so by the RBs it encounters on its path.

To summarize, it can be hypothesized that Kip3 has a dual-mode strategy to circumnavigate RBs (Figure 5.5). It is described as follows:

- When there are no RBs on the MT lattice, the motor walks along a single protofilament to reach the MT plus-end with maximum efficiency.
- If the motor encounters a RB along its path it circumnavigates the RB by left-biased sidestepping, which occurs within the step cycle. This is possible due to a flexible neck region and an extended neck linker.
- If both the forward and leftward tubulin-binding sites are blocked, the motor can also switch out of the step cycle to enter a diffusive slip-state. However, this is not energy efficient as the motor goes through futile hydrolysis cycles and slips back and forth. Therefore, this is a backup strategy mostly employed when the RB density is very high.

It must be noted that the proposed hypothesis is speculative, based only on preliminary evidence. Rigorous quantitative experiments must be performed to further verify the hypothesis.

Acknowledgements

Prof. Wilhelm Walter and Dr. Rene Schneider provided the rigor-kinesin-1 constructs. The preliminary RB studies on Kip3 under different salt conditions were performed with Dr. Felix Ruhnow.

CHAPTER 6

Summary and outlook

During mitosis, kinesin-8 motors play a key role in regulating the spindle length based to their MT plus end depolymerization activity. In order to reach the plus-end of MTs, kinesin-8 motors show superprocessive motility. To gain insight into the mechanism conferring such high motor processivity even on crowded MTs in the cytoplasm, the 3D motility of yeast kinesin-8, Kip3, along MTs was explored in two *in vitro* motility assays established in this work. Firstly, MT gliding assays were performed on reflective surfaces coated with Kip3 motors where the rotational motion of gliding MTs were measured using rhodamine speckled MTs in combination with FLIC microscopy. Rotational periodicities unrelated to the MT supertwist was observed. Secondly, stepping assays were performed on freely suspended MTs along with 3D tracking of the single QDot conjugated Kip3 motors, using Parallax. Helical motion with leftward pitches in the order of 2 µm was observed, confirming conclusively that Kip3 motors switch protofilaments in a biased manner. The ability to switch protofilaments was attributed to the flexible neck and long necklinker of Kip3. Additionally, 3D stepping and gliding assays revealed that sidestepping is not directly coupled to forward stepping but sidestepping probability increases on (i) prolonging the step dwell time by limiting the ATP concentration and (ii) weakening the motor-MT interactions by cleaving the MT e-hooks. It was hypothesized, supplemented with numerical simulations, that in the ATP waiting

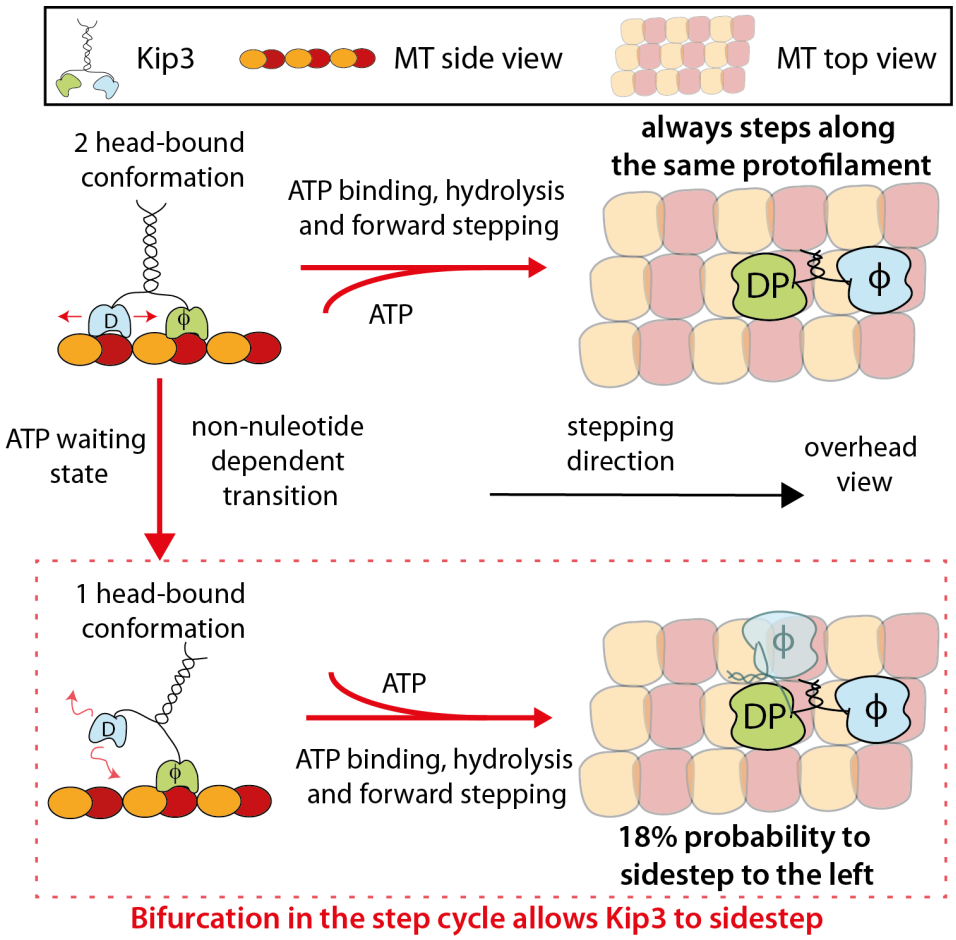

Figure 6.1: Illustration of the directed sidestepping strategy employed by Kip3. In the rate-limiting ATP waiting state Kip3 can transition from a 2HB conformation to a 1HB conformation. Whereas, the motor can step forward in both conformations, it can perform directed leftward side-steps only in the 1HB conformation. Here D denotes ADP, DP denotes ADP plus P_i, and Φ denotes no nucleotide. Loose binding or diffusion is represented by red arrows.

state the motor can switch from a 2HB conformation to a 1HB conformation with sidestepping only possible if ATP binds in the 1HB conformation (see Figure 6.1). Finally, Kip3 motility assays on RB decorated MTs revealed that Kip3 might have a dual-mode strategy to avoid RBs. Upon encountering a RB in the forward tubulin binding site, Kip3 circumvents it by (i) directed leftward sidestepping which occurs within the motor step cycle or (ii) unbiased diffusive motility when the motor switches out of the step cycle to enter a slip-state (Figure 6.2).

Since Kip3 solely functions as a MT plus-end depolymerase, efficiency in reaching the MT plus-end is crucial for its function. The proposed dual-mode strategy to circumnavigate around RBs would allow Kip3 motors to always reach

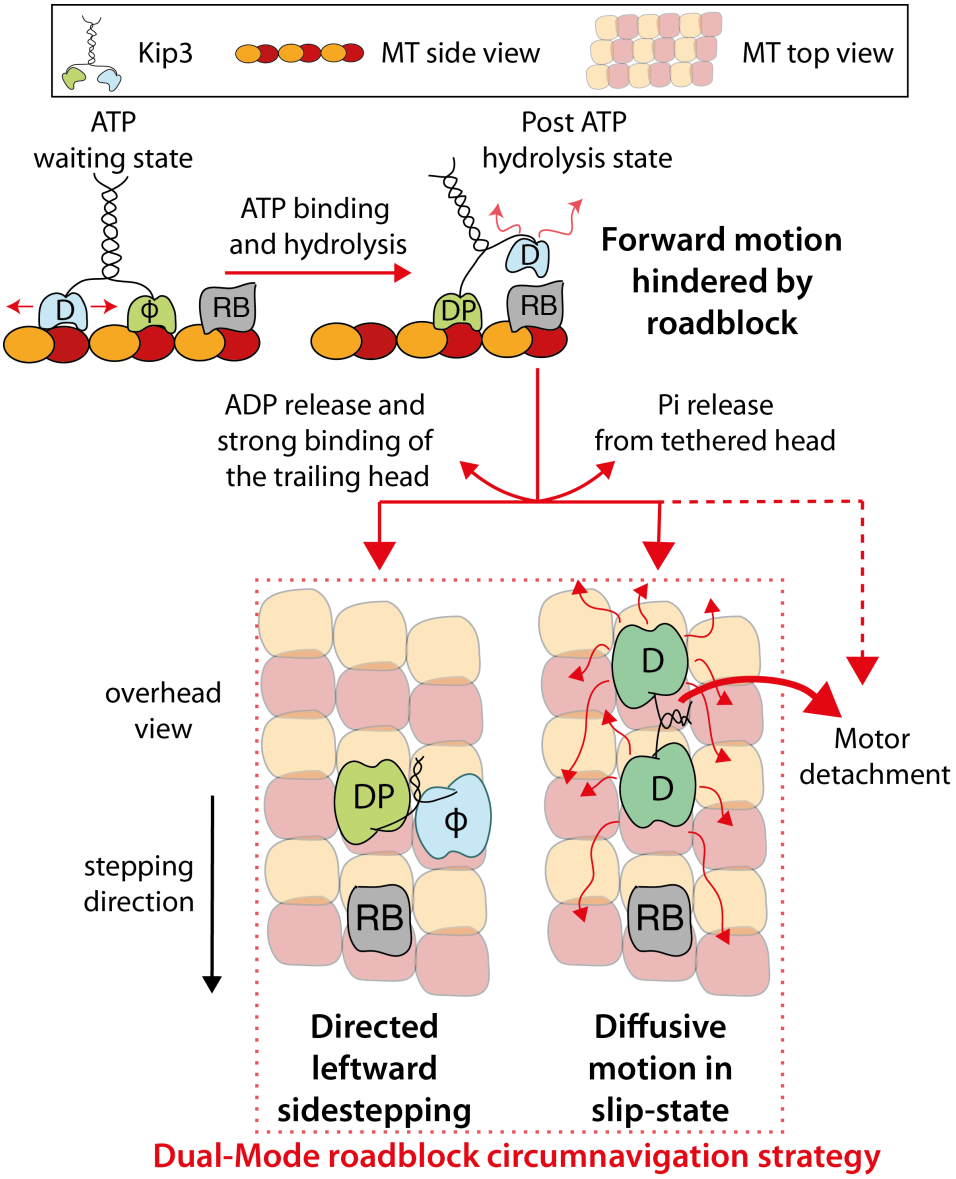

Figure 6.2: Illustration of the RB circumnavigation strategy used by Kip3. Kip3 feels the presence of a RB blocking the forward tubulin-binding site in the post-hydrolysis ADP.P_i state. In response, there is a kinetic race between the freely diffusing rear motor-head binding to the left tubulin binding site and the tethered motor-head releasing P_i. Upon P_i release, the motor can either enter a diffusive slip-state or detach from the MT lattice (the ratio is tuned by the ionic strength of the buffer). Here D denotes ADP, DP denotes ADP plus P_i, and Φ denotes no nucleotide. Loose binding or diffusion is represented by red arrows.

the MT end in the fastest possible way, consuming the least amount of energy. On a clear MT lattice, the motor steps forward along the same protofilament with a slight bias to perform leftward protofilament switches (1 leftward switch every 20-25 forward steps). Further, upon encountering a RB at the forward tubulin binding site the motor switches to a 1HB conformation which makes it possible to switch to the left protofilament. This is energetically efficient, since the motor is capable of avoiding RBs without switching out of the step cycle, utilizing only one ATP. However, if both the forward and left tubulin-binding sites are blocked, there is a possibility that the motor gets stuck in a jam. In such a situation, the motor has a second strategy to avoid RBs, where it switches out of the cycle into a diffusive slip-state. Upon diffusing to another free tubulin binding site, the motor would switch back to the regular step cycle. If diffusion was the only RB circumnavigation strategy, the motor would undergo numerous futile hydrolysis cycles rendering the overall motility process energetically inefficient. Therefore, the diffusive mode is only a back-up mechanism.

The proposed hypothesis, though appealing, must be confirmed with further rigorous experiments. Currently, in the established 3D stepping assays, the temporal ($\geq$100 ms) and spatial resolution ($\sim$20 nm) is relatively low and there is potential to develop the assay further to increase the resolution. Dark field scattering [149, 177] and interferometric scattering approaches [84] have recently been used for 2D tracking of kinesins with high temporal and spatial resolution. Potentially, such imaging approaches can be combined with Parallax to obtain high resolution 3D tracks for kinesins in suspended MT assays. High resolution tracking of Kip3 stepping by coupling an optical probe directly to one of the motor-heads would allow first-hand observation of directed leftward sidestepping. Furthermore, genetic engineering studies on Kip3 would reveal if the neck/neck-linker of the motor are indeed the vital structural elements that enable directed leftward sidestepping.

Further experiments could also be designed to explore the response of Kip3 motors to RBs. An obvious follow-up from this work would involve analysis of the motility parameters for Kip3 in conventional stepping assays (under assay conditions with different ionic strengths) on RB decorated MTs after quantitative characterization of the RB density. Also, the aforementioned high resolution tracking techniques could be used to directly observe individual steps performed by Kip3 on RB decorated MTs. Additionally, in such assays it would be possible to explore

how often the motor switches to the diffusive slip-state and whether the switches can also occur uninduced on MTs without RBs. This would provide an indication on whether directed sidestepping or diffusive sidestepping is the dominant strategy employed by the motor.

Finally, it must be noted that in this study we use static RBs which directly block the tubulin-binding site for kinesin motor-heads. *In vivo* RBs have different excluded volumes and can be static, diffusive or directed (slower motors). A future direction in this study would be to observe the motility response of Kip3 to different RB types.

To conclude, in this work, it was discovered that Kip3 motors has a refined strategy to circumnavigate RBs on the MT lattice. Is this a unique characteristic specific to kinesin-8 motors or all kinesin motors have co-evolved to have a similar RB circumnavigation approach? Indeed, it was shown that a kinesin-1 mutant with an extended neck-linker can switch protofilaments in a directed manner under rate-limiting ATP conditions. This hints towards a general sidestepping mechanism that facilitates navigation on crowded MTs for all processive kinesins with long neck-linkers. Future research in this direction will reveal further interesting details regarding the hindered motility of MT- based motors.

CHAPTER 7

Material and Methods

7.1 Protein purification and MT preparation

Tubulin

Porcine tubulin was purified from *porcine* brain (Vorwerk Podemus, Dresden, Germany) using established protocols as described previously [178].

Kip3-eGFP

Kip3-eGFP construct has a C-terminally fused enhanced GFP (eGFP) tag followed by a 6x histidine tag. The Kip3 cDNA was obtained from a previously available plasmid used to make the construct 6xHis-Kip3-GFP (used in previous studies in Howard laboratory and our laboratory [34, 34, 112, 165, 165]). In order to fuse the cDNA with eGFP-6xHis it was inserted into the pOCC8 plasmid vector with the restriction sites NotI and AscI, which is one of the plasmids in the library developed by Aliona Bogdanova at the PEP facility at MPI-BG by modifying pOET transfer plasmids (Oxford Expression Technologies, UK). Recombinant baculovirus were prepared by co-transfecting *Spodoptera fugiperda* (SF+) cells with a defective bacmid plus the pOCC8-Kip3 plasmid by Regis Lemaitre, at the PEP facility, MPI-CBG. The resultant virus stock was infected into SF+ cells and harvested after 3 days to express the Kip3-eGFP construct. The cells were pelleted, washed

and resuspended in Kip3 buffer (25 mM Tris HCl [VWR], pH 7.4 adjusted with KOH [VWR], 300 mM NaCl [VWR], 5 mM Imidazole [Sigma], 5 mM $MgCl_2$ [VWR], 0.2 % Triton X-100 [Sigma], 10 % glycerol [VWR], 10 mM DTT [Thermo Scientific, Waltham, USA] and 1 mM ATP [Jena Bioscience GmbH, Jena, Germany]) along with an EDTA-free protease inhibitor cocktail (Complete Ultra Tablets, Sigma). All following steps were performed at 4 °C. The cells were lysed by centrifugation for 1 h at 40000 g. For purification of the Kip3-eGFP construct the cell lysate was incubated with Ni-NTA agarose (Qiagen) for 2 h, washed several times in a 10 ml column (Bio-Rad) with Kip3 buffer (with additional 30-50 mM imidazole) and eluted with Kip3 buffer containing 150 mM imidazole. Eluted protein was snap-frozen in liquid nitrogen and stored at −80 °C.

Kip3-mfGFP

Kip3-mfGFP construct has a C-terminally fused multifunctional GFP (mfGFP) tag where a loop in the GFP sequence contains an octo-histidine, a streptavidin-binding peptide (SBP) and a c-Myc tag in tandem [150]. The Kip3 cDNA was inserted in the commercially available baculovirus transfer plasmid pOET1 (Oxford Expression Technologies, UK). One HindIII restriction site was removed from Kip3 cDNA without changing the amino acid sequence by site-directed mutagenesis. mfGFP sequence was amplified via PCR and restriction sites AscI and HindIII were inserted. The sequence was then inserted into the pOET1-Kip3 using AscI and HindIII restriction enzymes (New England Biolabs). The Kip3-mfGFP construct was then expressed in Sf+ cells and purified using the same protocol as for the Kip3-eGFP construct.

Full length kinesin-1 and kinesin-1$_{+DAL}$

Full length *drosophila melanogaster* kinesin-1 heavy chain (DmKHC) with a C-terminal 6x histidine tag was expressed and purified as described in Korten et al. [179]. Kinesin-1$_{+DAL}$, a kinesin-1 mutant construct truncated at residue 559 (with a C-terminal 6x histidine tag), having an extension of 3 amino acid residues (DAL) at the neck linker was obtained from the laboratory of William O. Hancock. The construct is expressed and purified as described in Shastry et al.[170].

Kinesin-1 rigor mutants

Unlabeled (and GFP labeled) rigor kinesin-1 mutants were generated by performing a T93N single-point mutation [111] on a kinesin-1 construct truncated at residue 430 (followed by a GFP tag in case of the GFP labeled construct). The construct was expressed and purified as described in Schneider et at [57].

MT polymerization

GMP-CPP grown, taxol-stabilized S-MTs were grown in a two-step process. 25 µl of BRB80 solution (80 mM Pipes [Sigma], pH 6.9, with KOH [VWR], 1 mM EGTA [Sigma], 1 mM $MgCl_2$ [VWR]) supplemented by a high concentration (12 µM) of porcine tubulin (S-MTs: 99.44 % unlabeled and 0.56 % rhodamine-labeled [TAMRA; Thermo Fisher Scientific]; biotinylated S-MTs: 94.44 % unlabeled, 5 % unlabeled biotinylated (Cytoskeleton Inc., Denver, CO) and 0.56 % rhodamine-labeled), 1 mM GMP-CPP (Jena Bioscience, Jena, Germany) and 4 mM $MgCl_2$ were incubated on ice for 5 min and then for 20-30 min at 37 °C to grow a large number of short, dimly-labeled MT seeds. In parallel, an elongation mix consisting of a 100 µl BRB80 solution supplemented by a low concentration (0.8 µM) of porcine tubulin (96.67 % unlabeled and 3.33 % rhodamine-labeled), 1 mM GMP-CPP and 4 mM $MgCl_2$ was heated to 37 °C for 30 s (after a 5 min incubation on ice). Afterwards, 10 µl of the dimly-labeled seed solution (containing S-MT or biotinylated S-MT seeds) was added to the elongation mix (resulting total tubulin concentration ~2 µM) and incubated at 37 °C for 3 h. During this incubation period, bright extensions grew off the dim seeds and formed the speckles in the resulting S-MT and biotinylated S-MT lattices after concurrent MT end-to-end annealing. Assembled S-MTs and biotinylated S-MTs were centrifuged using a Beckman airfuge (Beckman, Brea, CA) at 100 000 g for 5 min. The pellet was resuspended in a volume of 50-100 µl BRB80T (BRB80 supplemented with 10 µM Taxol [Sigma]).

For the control stepping assays and the suspended MT stepping assays, long (average length ≥15 µm, GMP-CPP grown, taxol-stabilized (double-stabilized) rhodamine labeled MTs were produced in the following manner: 100 µl of BRB80 solution supplemented by 2 µM porcine tubulin (1:3 mixture of rhodamine-labeled and unlabeled), 1 µM GMP-CPP and 1 µM $MgCl_2$ were incubated on ice for 5 min, before polymerization for 15-20 h at 27 °C to obtain long MTs. Free tubulin was removed by centrifuging the solution using a Beckman airfuge (Beckman, Brea,

CA) at 100000 g for 5 min. The pellet was resuspended in a volume of 50-100 µl BRB80T (BRB80 supplemented with 10 µM Taxol).

For the QDot labeled MT gliding rotation assays, biotinylated double stabilized MTs were grown similar to MTs used in stepping assay, using a 1:2:50 (rhodamine-labeled:unlabeled biotinylated: unlabeled) tubulin mixture.

For cleavage of the MT e-hooks, rhodamine speckled MTs were incubated with 100-200 µg/ml subtilisin (Sigma) for 40 min at 37 °C. The reaction was stopped by subsequently adding 10 mM PMSF (Sigma) to the MT solution. The digested MTs were centrifuged and the pellet was resuspended in 50 µl BRB80T.

7.2 *In vitro* motility assays

Gliding assays

Kip3 driven gliding assays: Kip3 gliding assays were performed in microfluidic flow channels constructed from 22 mm×22 mm glass coverslips (Menzel, Braunschweig, Germany; #1.5) and 10 mm×10 mm silicon wafers having a 30 nm thermally grown oxide layer (GESIM, Grosserkmannsdorf, Germany), both dichlorodimethylsilane (DDS) coated (as described in Korten et al. [180]) to make the surface hydrophobic . NESCO (Azwell Inc., Osaka, Japan) film was used as spacer and typically, the flow channels have the dimensions of 10 mm×1.5 mm×100 µm. To perform the gliding assay, flow channels were flushed with the following sequence if: (i) fab fragment solution consisting of 20 µg/ml F(ab')2 fragments (anti-mouse IgG [Fc specific] antibody developed in goat; Sigma) in PBS in order to promote anti-body binding (incubation time 5 min), (ii) Pluronic F127 (Sigma, 1 % in PBS) in order to block the surface from unspecific protein adsorption (incubation time 30-60 min), (iii) antibody solution consisting of 0.5 mg/ml anti GFP monoclonal antibodies (mouse, MPI-CBG antibody facility) in PBS in order to allow specific binding of the antibodies to the F(ab')2 fragments (incubation time 10 min), (iv) motor dilution buffer consisting of 112.5 mM KCL, 1 mM ATP (unless mentioned otherwise; Roche), 0.1 % Tween20 (Sigma), 0.2 mg/ml casein (Sigma) and 0.2 mg/ml DTT (Sigma) in BRB80 to remove unbound antibodies, (v) motor solution consisting of 120 nM Kip3-eGFP in motor dilution buffer in order to bind the Kip3 proteins specifically to the antibodies (incubation time 10 min), (vi) S-MT solution consisting of S-MTs in motor dilution buffer (incubation time 5 min)

and (vii) imaging solution consisting of the oxygen scavenger system (consisting of 40 mM glucose [Sigma], 110 µg/ml glucose oxidase [SERVA], 22 µg/ml catalase [Sigma]) in motor dilution buffer to remove excess MTs. For experiments using Qdot coated MTs instead of S-MTs, 10-20 pM streptavidin conjugated QDot655 (Lifetechnologies) solution was added to the biotinylated MTs (or biotinylated S-MT for control assays) solution and after an incubation time of 2 min this mixture was diluted and used as stated in (vi).

In gliding assays with RB decorated MTs, unlabeled rigor kinesin-1 was diluted (to concentrations as mentioned in Chapter 5) in the imaging solution. In control gliding assays, the silicon wafers were exchanged with 18 mm×18 mm glass coverslips and Parafilm (Sigma) was used as spacers (instead of NESCO film). For the phosphate salt experiments, 112.5 mM KCl was replaced by 112.5 mM KPi (50 % monobasic, 50 % dibasic; Merck) in the imaging solution.

Kinesin-1 driven gliding assays: Full-length kinesin-1 gliding assays were performed in flow channels (constructed of easy-cleaned [181] glass coverslips and silicon wafers) flushed with the following sequence: (i) casein solution consisting of 0.5 mg/ml casein in BRB80 in order to block the flow-channel surfaces (incubation time 5 min), (ii) motor solution consisting of 150 nM kinesin-1, 1 mM MgATP, 0.2 mg/ml casein, 10 mM DDT in BRB80 in order to bind kinesin-1 proteins unspecifically to the casein surface (incubation time 5 min), (iii) S-MT solution consisting of S-MTs diluted in BRB80T supplemented with 1 mM MgATP, 0.2 mg/ml casein, 10 mM DDT (incubation time 2 min) and (iv) imaging solution consisting of 1 mM MgATP (unless specified otherwise), 0.2 mg/ml casein, 10 mM DDT, and an oxygen scavenger mixture in BRB80T to remove the excess MTs. For experiments using QDot coated MTs instead of S-MTs the previously mentioned strategy (see Kip3 gliding assay protocol) was used in (iii).

Kinesin-1_{+DAL} gliding assays were performed similar to Kip3 gliding assays except for the following changes: (i) The motors were specifically bound to the surface via Penta-His antibodies (Qiagen) instead of GFP antibodies. (ii) No additional KCl was added to the buffer. The ATP concentration was varied as indicated in the results.

Fabrication of polymer structures on glass

The patterned glass coverslips were fabricated using UV-NIL [182]. The strategy

used for fabrication is described briefly: (i) The pattern to be imprinted was designed and printed on a chrome photomask (JD Photo Data, Herts, UK). (ii) The Master was fabricated by photolithography by using a mask aligner (EVG, EVGroup, St. Florian am Inn, Austria). A 4 inch silicon wafer coated with a positive photoresist (AZ 9260; MicroChemicals GmbH, Ulm, Germany), 1:3 (w/w) diluted in PGMEA (MicroChemicals GmbH), was irradiated by UV light (100 mJcm^2) through the photomask and developed in AZ400K (MicroChemicals GmbH). The surface was then spin-coated with an anti-sticking layer (ASL; EVGroup, St. Florian am Inn, Austria). (iii) 3 gr perfluoropolyether (PFPE; Fluorolink MD700, Solvay, Milan, Italy) mixed with 6 mg of a cross-linker (Irgacure 2022; BTC Europe GmbH, Koeln, Germany) was poured on the master surface. A glass substrate, functionalized with KBM primer (EVGroup) to improve polymer adhesion, was pressed on top of the liquid. (iv) After liquid spreading, the sandwich structure was exposed to UV light (5000 mJcm^2) to polymerize the liquid. (v) The glass substrate was peeled off from the master (the ASL layer on the master promotes easy release of the stamp from the master). The final stamp is a glass surface coated with the patterned (negative of the master) PFPE polymer. (vi) An easy-cleaned [181] glass coverslip (22 mm×22 mm) was spin-coated with an adhesion promoter, EVGprime/ZAP 1020 (height 10 nm; EVGroup) and with an UV curable resin, EVG NIL UV/A 200 nm (height 280 nm; EVGroup). (vii) A mask aligner (EVG 620; EVGroup), equipped with tools for the UV-NIL process, was used to control the alignment and to adjust the pressure between the stamp and the coated coverslip. (viii) Resin crosslinking was activated by UV exposure (2500 mJcm^2). The applied pressure (1 bar) ensures the filling of the hollow space in the stamp (avoids the formation of air bubbles) leading to a perfect negative copy of the structures from the stamp. (ix) Finally, the coverslip with the desired resin pattern was peeled off from the stamp. Further details on the polymer ridges structured on glass using UV-NIL can be seen in Figure 3.4.

Stepping assays

All Kip3-QDot stepping assays were performed in microfluidic flow channels constructed on 22 mm×22 mm glass coverslips patterned with UV-NIL polymer resin (unpatterned in case of control experiments) and 18 mm×18 mm unpatterned glass coverslips, both DDS-coated to make the surface hydrophobic [180]. Be-

fore silanization, the patterned coverslip was only cleaned mildly (sonicated in 5 % mucasol [VWR] and then in ethanol [VWR]) to avoid corrosion of the structure. Typically, each coverslip had three flow channels having the dimensions of 18 mm×3 mm×100 µm (L×W×H). Control Kip3 stepping assays and Kip3-QDot stepping assays were performed on unpatterned silanized coverslips as described in Korten et al. [180]. Flow channels were flushed with a sequence of: (i) Beads solution consisting of 0.5 % 200 nm Tetraspeck beads (Invitrogen) in PBS (incubation time 1 min). (ii) Antibody solution consisting of 3 mg/ml anti-beta tubulin antibody (SAP.4G5; Sigma) in PBS in order to unspecifically bind antibodies to the surface (incubation time 5 min). (iii) Pluronic F127 (1 % in PBS; Sigma) in order to block the surface from unspecific protein adsorption (incubation time >60 min). (iv) 4x BRB80 buffer to remove excess F-127 in solution and to exchange buffers. (v) MT solution with high concentration of MTs in BRB80T, followed by an immediate washing step with BRB80T in order to immobilize MTs perpendicular to the ridges via specific interactions with anti-beta tubulin antibodies. (vi) Imaging solution consisting of 112.5 mM KCL, 1 mM ATP (varied between 1 µM to 1 µM for the experiment to measure ATP dependence on Kip3 velocity), 0.1 % Tween20, 0.2 mg/ml casein, 0.2 mg/ml DTT, 10 µM Taxol and an oxygen scavenger mixture in BRB80 for imaging MTs in order to find a suitable field of view. (vii) Kip3-QDot buffer consisting of Kip3-QDot conjugate solution diluted 100 times in imaging solution. The Kip3-QDot conjugate solution consists of 100 nM QDot (QDot 655 Streptavidin conjugate) and 10 nM Kip3-mfGFP (at 10:1 conjugation ratio, unless specified otherwise), incubated in motor dilution buffer (imaging solution without the oxygen scanvenger system) for >30 min. In stepping assays with RB decorated MTs, unlabeled (or GFP-labeled when mentioned) rigor kinesin-1 was diluted (to concentrations as mentioned in Chapter 5) in the imaging solution. In control stepping assays a similar protocol was used other than the following changes; (i) Bead solution consisted of 0.1 % 100 nm Tetraspeck beads (Invitrogen) in PBS and (ii) concentration of the unconjugated Kip3 motors in the imaging solution was 0.04 nM. Further, in conventional stepping assays with RB decorated MTs, Kip3 motors were incubated with Atto 647N GFP nanobody (diluted to ~20 mg/mol; ChromoTek GmbH, Planegg-Martinsried, Germany) for 2 min in imaging buffer before flushing in the flow channels.

7.3 Image acquisition

Gliding assays

Optical imaging was performed using an inverted fluorescence microscope (Axiovert 200M, Carl Zeiss, Gőttingen, Germany or Axio Observer Z1; Carl Zeiss Microscopy GmbH, Jena, Germany) with a 63x water immersion 1.2 NA objective (Zeiss) in combination with an EMCCD camera (Ixon Plus or iXon Ultra; Andor Technology, Belfast, UK) controlled by Metamorph (Molecular Devices Corporation, Sunnyvale, CA, USA) providing a pixel size of 0.254 µm. A Lumen 200 metal arc lamp (Prior Scientific Instruments Ltd., Cambridge, UK) was used for epifluorescence excitation. Rhodamine-labeled S-MTs gliding on the silicon-wafer surfaces were imaged 'through the solution' (i.e. on the far side of the flow channels) using a TRITC filterset (ex BL520/35, dc zt532 RDCXT, em BL585/40; all Chroma Technology Corp., Rockingham, VT) with an exposure time of 400 ms per frame. Images were recorded in time-lapse mode (0.2-1 fps). For experiments with QDot coated MTs, an argon-krypton mixed gas laser at 488 nm (Innova 70 Spectrum, Coherent, Dieburg, Germany) was used to visualize the QDots attached to gliding MTs using a bandpass filter (ex BL475/35, dc zt488 RDC, em BL655/40; all Chroma). Temperature (24 °C unless mentioned otherwise) was controlled by fitting a custom made hollow brass ring around the body of the objective and connecting it to a water bath with a cooling/heating unit (F-25-MC Refrigerated/Heating Circulator; JULABO GmbH, Seelbach, Germany) [53].

For the kinesin-1 and kinesin-1_{+DAL} gliding assays, the frame rate was adjusted to 0.1-10 fps depending on the gliding speeds.

Stepping assays

Optical imaging was performed using an inverted fluorescence microscope (Axio Observer Z1) with a 63x oil immersion 1.46NA objective (Zeiss) in combination with an EMCDD camera (iXon Ultra) controlled by Metamorph. For 3D imaging, a custom built optical setup called Parallax, was placed in the image beam path between the inverted fluorescence microscope and the EMCCD camera. Details about the Parallax setup are provided in Chapter 3 (Figure 3.5). Temperature (24 °C) was maintained in the same manner as for the gliding assays. Rhodamine-labeled MTs were observed by epifluorescence using a Lumen 200 metal arc lamp

with a TRITC filter. Qdot signal from the Kip3-QDot conjugates were observed in HILO mode [154] using a PhoxX 488nm Laser (~15-30 mW; Omicron-Laserage, Rodgau-Dudenhofen, Germany) with a QDot655 filter set (same as the one used in gliding assays). For control experiments a different EMCCD (iXon Plus; Andor Technology) was used and the GFP signal from the Kip3-mfGFP motors was observed in total internal reflection (TIRF) mode using the PhoxX 488 nm Laser with a GFP filter set (ex BL475/35, dc zt 488 RDC, em BL525/35; all Chroma). In suspended MT stepping assays, reference beads and rhodamine-labeled double-stabilized MTs were immobilized on the polymer-patterned coverslips and the split images were observed simultaneously on two halves of the same camera chip. A field of view was selected when there were 3 (or more) reference beads bound to the surface and numerous MTs suspended between ridges. The MTs were imaged for 100 frames (5 fps) in order to eliminate evaluation of Kip3-QDot events on swiveling MTs or MTs touching the valley surface (interpreted qualitatively from the difference in the MT profile in the two split images). The region was then exposed to 488 nm laser light (excitation light used later for imaging the QDots) for 1-2 min to bleach the background autofluorescence signal from the polymer-pattern. Afterwards, the QDot-Kip3 mixture was flushed in and image acquisition (3-5 fps) was started after 1 min in order to record QDot-Kip3 motility events. In conventional gliding assays with RB decorated MTs, Atto647 conjugated Kip3 motors were imaged in TIRF mode using the PhoxX 642 nm Laser (~5 mW; Omicron-Laserage) with a 647 filter set (ex BL620/60, dc zt 649 RDC, em BL7000/75; all Chroma) in timelapse mode (0.05-0.2 fps).

7.4 Data Analysis

Gliding assays

The rotational pitch of S-MTs was obtained from their kymographs (space-time intensity plots), which were generated in Metamorph. The kymographs were then analyzed with MATLAB (Mathworks, Natick, MA) using the speckle analysis method described in the Chapter 2. QDots were tracked with FIESTA [145], an open-source tracking software based on MATLAB. To obtain the rotational pitch, QDot intensity profiles were analyzed analogous to the evaluation of the intensity profiles of individual speckles.

Stepping assays

The acquired image stream of the Kip3-QDot stepping assay was analyzed using FIESTA [145] where every frame was split laterally into two halves (corresponding to the two split images created by the Parallax setup [148]) to create separate image channels. Since the split beam paths cannot be projected exactly onto the two halves of the camera chip (due to limitations in the alignment of the optical elements), a translational and rotational offset between the two channels is obtained by the reference beads (minimum 3 reference points necessary). Stage drift during imaging is corrected with the averaged position of the reference beads (in 3D). Each Kip3-QDot event was tracked in the two channels and co-ordinates (in 3D; see Chapter 3) were obtained (offset and drift corrected). The co-ordinates were fitted to a tube of diameter 25 nm (to account for MT width) using spline interpolation to obtain angular information of the Kip3-QDot track with respect to the MT (see Chapter 3). In order to obtain the rotational pitch of the track, the angular information for the Kip3-QDot event was plotted against the travelled distance and the rotational pitch as well as the end-to-end velocity for each rotation was derived by manual computer-aided measurement. For calculation of the sidestepping rate as well as sidestepping probability we used the 8.4 µm supertwist (result from kinesin-1 gliding rotation assays in Chapter 2) and 8.3 nm tubulin interdimer distance for GMP-CPP MTs (see Supplementary Information). For obtaining velocities in control stepping assays, the stepping events are tracked using FIESTA and the slope of the linear fit of the distance-time information provides the velocity [53].

Analysis of distributions with error estimation

For estimating parameters from any given distribution (e.g. velocity, rotational pitch, rates) we use a bootstrapping approach [183, 184]. Here, the distribution (N number of measurements) is resampled by randomly picking N measurements from the measured distribution (with replacement) and calculating the median of the resampled distribution. This is repeated 1000 times. The resulting bootstrapping distribution is used to estimate the parameter (mean of the bootstrapping distribution) and its error (standard deviation of the bootstrapping distribution). All values and errors as well as error bars in this paper use (99 % confidence interval), unless otherwise noted.

Supplementary Information

MATLAB code for numerical simulation of the stepping mechanism

```
function Kip3Simulation
% States: % 1 = 2HB waiting for ATP, 2 = 1HB waiting for ATP, ...
    3 = ATP hydrolysis
rng('shuffle');
% motor and MT properties
t_step_max = 0.160; % time per step in s, 6.25 steps per ...
    second (51.9nm/s)
k_step_max = 1 / t_step_max;
t_rest = 0.045; % time per ATP independent state
k_rest = 1 / t_rest;
k_ATP_max = 1 / (t_step_max - t_rest);
k_2HBto1HB = k_ATP_max / 4; % transition rate from 2HB to 1HB
Km = 15; % Michaelis-Menten constant in μM
p_left = 0.18; % probability of sidestepping in 1HB
maxFutile = 0.4; % maximum probability of futile hydrolysis
minFutile = 0.2; % maximum probability of futile hydrolysis
kin1_pitch = 8400; % rotational pitch of 14-PF MTs gliding on ...
    kinesin-1
d_step = 8.3; % forward stepsize of kinesin motors
rot_perForwardStep = 360 / (kin1_pitch / d_step);
rot_perSideStep = 360 / 14;
% simulation properties
nMol = 50; % number of molecules
ATP = 1000; % ATP concentration in μM
nRotations = 2; % number of rotations to average
T = 4000; % max time per molecule
dt = 0.001; % time resolution
% initialisation
```

```
itime = zeros(nMol,1);
pitch = zeros(nMol,1);
for n = 1:nMol
    % initialisation
    nForwardStep = 0;
    nSideStep = 0;
    rotation = 0;
    state = 1;
    % calculate rates and probabilities for specific ATP ...
       concentration
    k_step = k_step_max * ATP / (Km + ATP);
    t_step = 1 / k_step;
    k_ATP = 1 / (t_step - t_rest);
    p_ATP = k_ATP * dt;
    p_rest = k_rest * dt;
    p_2HBto1HB = k_2HBto1HB * dt;
    % calculate probabilities per motor
    p_futile = minFutile + rand*(maxFutile-minFutile);
    % start Monte-Carlo-Simulation
    for t = dt:dt:T
        if state == 1 % 2HB waiting for ATP
            p = rand;
            if p<p_ATP*(1-p_futile) % ATP binds in 2HB ...
               waiting state
                state = 3; % transition to ATP hydrolysis
                nForwardStep = nForwardStep + 1; % makes a ...
                   forward step
                % adds rotation according to supertwist of ...
                   14-PF MTs
                rotation = rotation + rot_perForwardStep;
            elseif p≥p_ATP && p<p_2HBto1HB+p_ATP % transition ...
               to 1HB before ATP binding
                state = 2; % transition to 1HB waiting for ATP
            end
        end
        if state == 2 % 1HB waiting for ATP
            p = rand;
            if p<p_ATP*(1-p_futile) % ATP binds in 1HB ...
               waiting state
                state = 3; % transition to ATP hydrolysis
                p = rand;
```

```
                if p<p_left  % make sidestep after ATP binding
                    nSideStep = nSideStep+1; % makes a sidestep
                    % adds rotation according to switch of ...
                       protofilament
                    rotation = rotation + rot_perSideStep;
                else  % make forward step after ATP binding
                    nForwardStep = nForwardStep+1; % makes a ...
                       forward step
                    % adds rotation according to supertwist ...
                       of 14-PF MTs
                    rotation = rotation + rot_perForwardStep;
                end
            end
        end
        if state == 3 % ATP hydrolysis and rest of the cycle
            p = rand;
            if p<p_rest % finishing rest of cycle
                % hydrolyse ATP, release ADP from leading head,
                % followed by Pi release from trailing head
                state = 1;
            end
        end
        if rotation > nRotations*360 % check if rotations are ...
           complete
            % average over all rotations
            itime(n,1) = t / nRotations;
            pitch(n,1) = nForwardStep * d_step / nRotations;
            break;
        end
    end
end
velocity = pitch./itime;
scatter(velocity,pitch/1000);
```

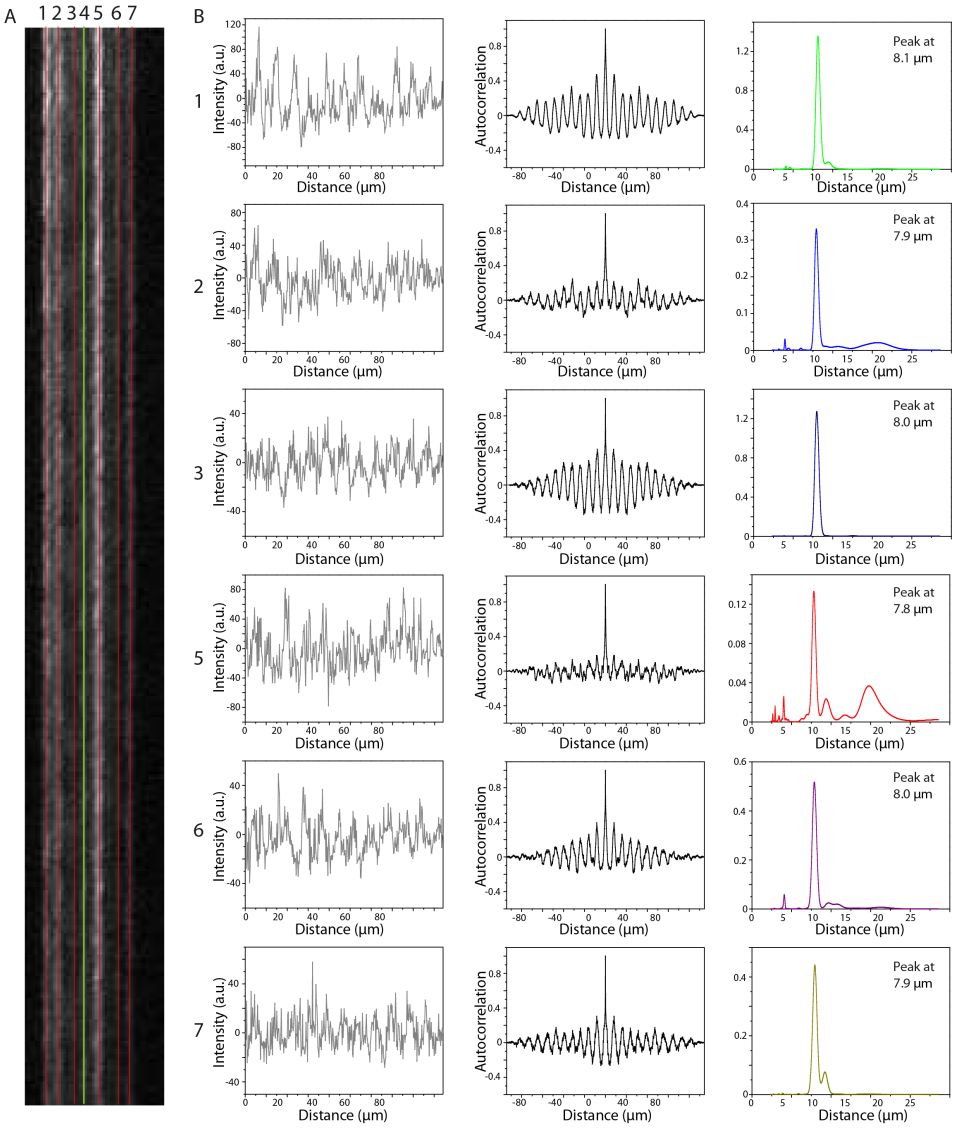

Figure S.1: Analysis of the individual speckles of the example kymograph in Figure 2.3. **(A)** Straightened kymograph (as seen in Figure 2.3C) with line scans over the seven individual speckles numbered 1 to 7. The 4th speckle (line scan marked in green) is already analyzed in Figure 2.3. The line scans over the other speckles are marked in red. **(B)** The intensity profiles over distance, the auto-correlation of the intensity profiles and the power spectra of the auto-correlation for the speckles 1,2,3,5,6,7. The corresponding peaks for the power spectra are at 8.1 µm, 7.9 µm, 8.0 µm, 7.8 µm, 8.0 µm and 7.9 µm. Figure relevant to Section 2.3.

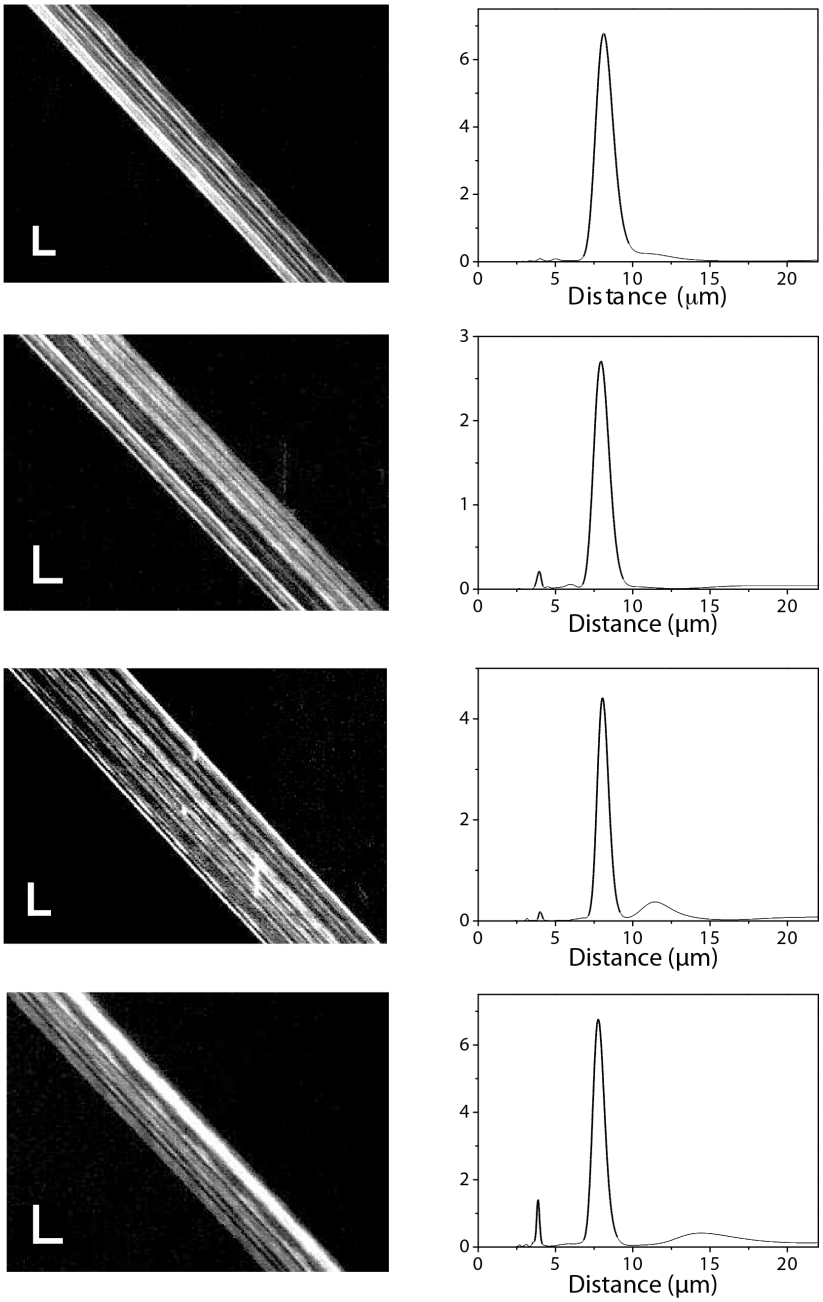

Figure S.2: Four typical kymographs of S-MTs gliding on kinesin-1. The combined power spectra for the individual kymographs have their main peak at 8.0 µm, 8.1 µm, 7.8 µm and 7.9 µm. The power spectra also have a prominent peak at half distance from the main peak. This contribution is due to some speckles being in close proximity to one another. There are also peaks at higher distances that are mainly due to variable background noise in the kymographs. Vertical scale bars represent 10 s and horizontal scale bars represent 5 µm. Figure relevant to Section 2.3.

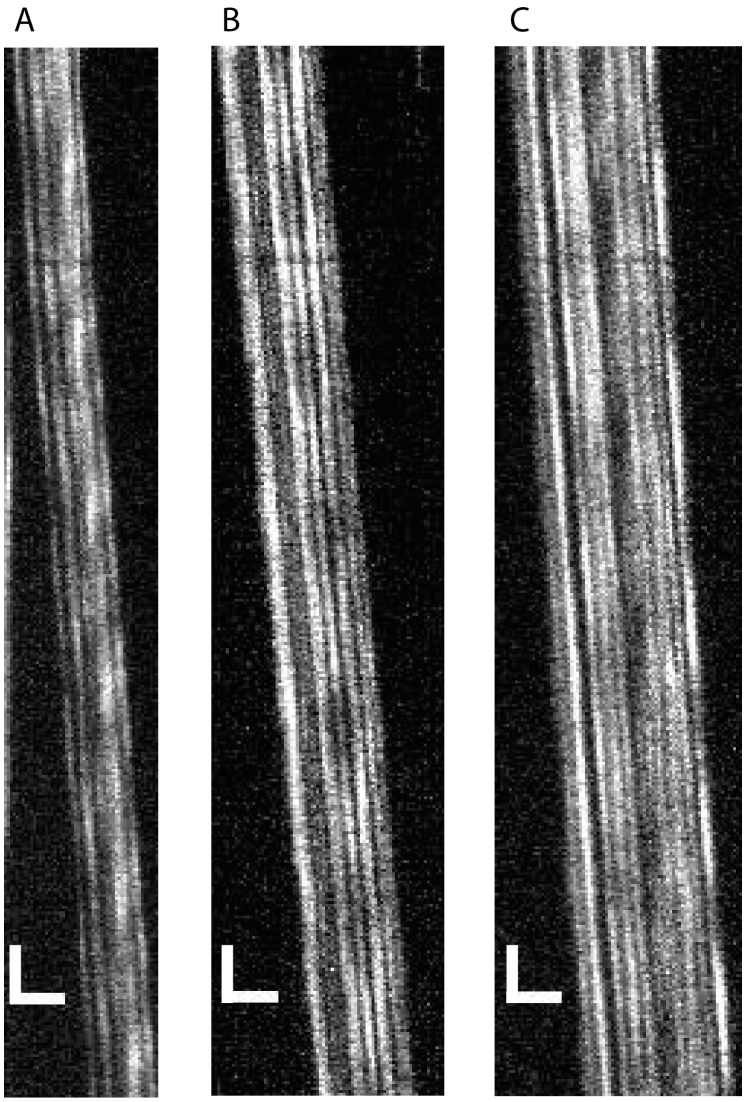

Figure S.3: Three typical kymographs of S-MTs gliding on Kip3. The combined power spectra analysis of the individual kymographs yields rotational pitches of 1.5 µm **(A)**, 1.2 µm **(B)**, and 1.3 µm **(C)**. Vertical scale bars represent 20 s and horizontal scale bars represent 5 µm. Figure relevant to Section 2.4.

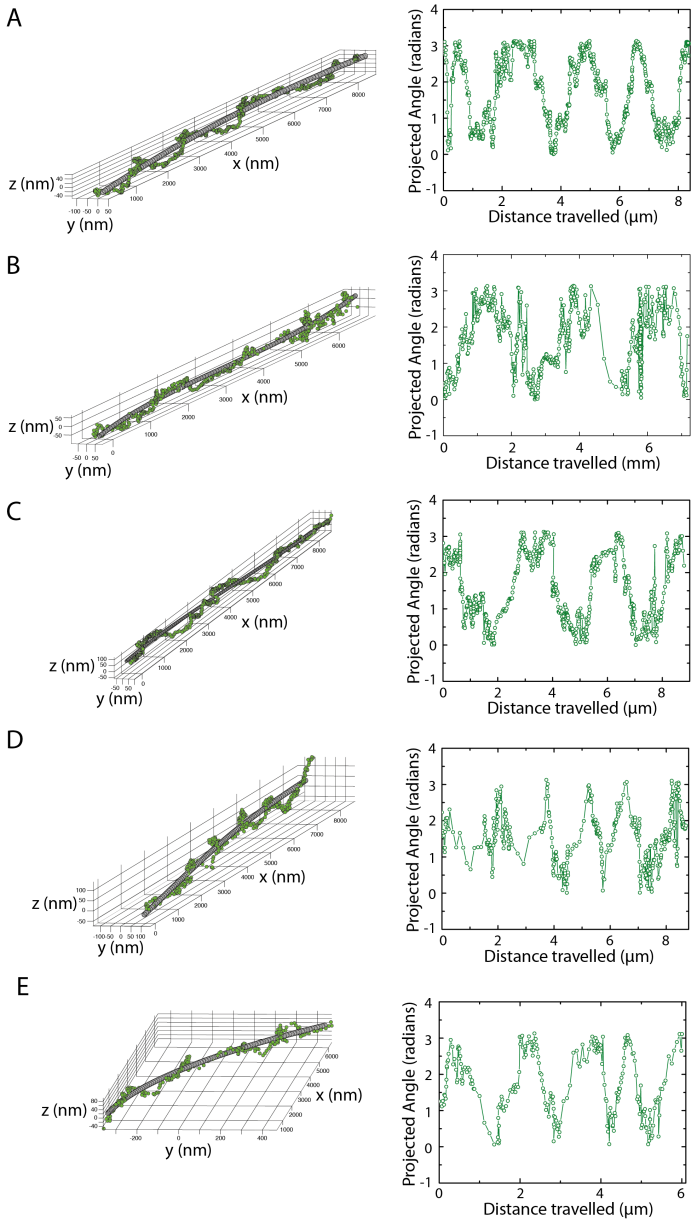

Figure S.4: Example Kip3-QDot stepping events on freely suspended MTs. The 3-D tracking data around the fitted tube and plot of the angle projected by the Kip3-QDot to the fitted path versus the distance travelled for 5 example tracks. (A) Example event A has a velocity of 42.6 ± 1.0 nm/s and rotates with an average pitch of 2.1 ± 0.2 µm (number of rotations n=3). (B) Example event B has a velocity of 43.2 ± 11.0 nm/s and rotates with an average pitch of 2.3 ± 0.3 µm (n=2). (C) Example event C has a velocity of 50.1 ± 0.1 nm/s and rotates with an average pitch of 2.7 ± 0.4 µm (n=2). (D) Example event D has a velocity of 39.4 ± 2.1 nm/s and rotates with an average pitch of 1.6 ± 0.2 µm (n=4). (E) Example event E has a velocity of 40.0 ± 4.5 nm/s and rotates with an average pitch of 1.4 ± 0.4 µm (n=3). The velocity and roational pitch are given in mean ± S.D. Figure relevant to Section 3.4.

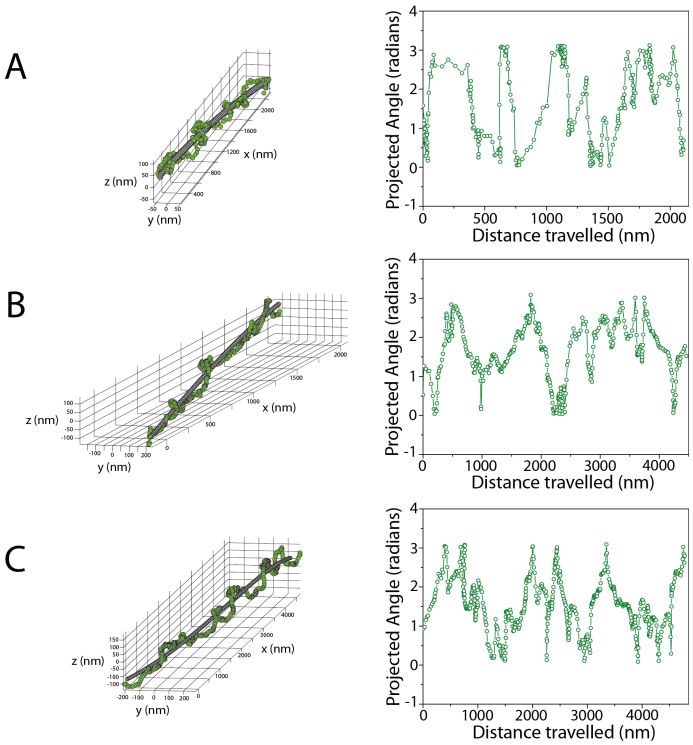

Figure S.5: Example Kip3-QDot stepping events on roadblock decorated suspended MTs. The 3-D tracking data around the fitted tube and plot of the angle projected by the Kip3-QDot to the fitted path versus the linear distance travelled for 3 example tracks (**A**, **B**, **C**) on MTs decorated with rigor kinesin-1 RBs (15 nM). Figure relevant to Section 5.3.

Bibliography

[1] P. Schwille and S. Diez, "Synthetic biology of minimal systems," *Critical Reviews in Biochemistry and Molecular Biology*, vol. 44, 2009.

[2] A. Desai and T. J. Mitchison, "Microtubule Polymerization Dynamics," *Annual Review of Cell and Developmental Biology*, vol. 13, 1997.

[3] B. Alberts, A. Johnson, J. Lewis, D. Morgan, M. Raff, K. Roberts, and P. Walter, "Molecular Biology of the Cell 6e," vol. 6, 2014.

[4] B. P. Piasecki and C. D. Silflow, "The UNI1 and UNI2 genes function in the transition of triplet to doublet microtubules between the centriole and cilium in Chlamydomonas.," *Molecular biology of the cell*, vol. 20, 2009.

[5] J. Van Mameren, K. C. Vermeulen, F. Gittes, and C. F. Schmidt, "Leveraging single protein polymers to measure flexural rigidity," *Journal of Physical Chemistry B*, vol. 113, 2009.

[6] H. Bowne-Anderson, M. Zanic, M. Kauer, and J. Howard, "Microtubule dynamic instability: A new model with coupled GTP hydrolysis and multistep catastrophe," *BioEssays*, vol. 35, 2013.

[7] K. Oiwa and H. Kojima, "Molecular motors: Keep on moving," *Nature Nanotechnology*, vol. 3, 2008.

[8] G. M. Alushin, G. C. Lander, E. H. Kellogg, R. Zhang, D. Baker, and E. Nogales, "High-Resolution microtubule structures reveal the structural transitions in $\alpha\beta$-tubulin upon GTP hydrolysis," vol. 157, 2014.

[9] M. Caplow and J. Shanks, "Evidence that a single monolayer tubulin-GTP cap is both necessary and sufficient to stabilize microtubules.," *Molecular Biology of the Cell*, vol. 7, 1996.

[10] D. N. Drechsel and M. W. Kirschner, "The minimum GTP cap required to stabilize microtubules," *Current Biology*, vol. 4, 1994.

[11] T. Mitchison and M. Kirschner, "Dynamic instability of microtubule growth.," *Nature*, vol. 312, 1984.

[12] E. Nogales and H. W. Wang, "Structural intermediates in microtubule assembly and disassembly: How and why?," *Current Opinion in Cell Biology*, vol. 18, 2006.

[13] S. Ray, "Kinesin follows the microtubule's protofilament axis," *The Journal of Cell Biology*, vol. 121, 1993.

[14] R. H. Wade, D. Chrétien, and D. Job, "Characterization of microtubule protofilament numbers. How does the surface lattice accommodate?," *Journal of Molecular Biology*, vol. 212, 1990.

[15] J. Howard, "Mechanics of Motor Proteins and the Cytoskeleton," vol. 7, 2001.

[16] P. B. Schiff, J. Fant, and S. B. Horwitz, "Promotion of microtubule assembly in vitro by taxol," *Nature*, vol. 277, 1979.

[17] A. A. Hyman, D. Chretien, I. Arnal, and R. H. Wade, "Structural changes accompanying GTP hydrolysis in microtubules: Information from a slowly hydrolyzable analogue guanylyl-(α,β)-methylene- diphosphonate," *Journal of Cell Biology*, vol. 128, 1995.

[18] B. Mickey and J. Howard, "Rigidity of microtubules is increased by stabilizing agents," *Journal of Cell Biology*, vol. 130, 1995.

[19] D. L. Coy, W. O. Hancock, M. Wagenbach, and J. Howard, "Kinesin's tail domain is an inhibitory regulator of the motor domain.," *Nature cell biology*, vol. 1, 1999.

[20] H. Y. K. Kaan, D. D. Hackney, and F. Kozielski, "The structure of the kinesin-1 motor-tail complex reveals the mechanism of autoinhibition.," *Science (New York, N.Y.)*, vol. 333, 2011.

[21] R. D. Vale, "The molecular motor toolbox for intracellular transport," *Cell*, vol. 112, 2003.

[22] H. Miki, M. Setou, K. Kaneshiro, and N. Hirokawa, "All kinesin superfamily protein, KIF, genes in mouse and human.," *Proceedings of the National Academy of Sciences of the United States of America*, vol. 98, 2001.

[23] H. Miki, Y. Okada, and N. Hirokawa, "Analysis of the kinesin superfamily: Insights into structure and function," *Trends in Cell Biology*, vol. 15, 2005.

[24] N. Hirokawa, Y. Noda, Y. Tanaka, and S. Niwa, "Kinesin superfamily motor proteins and intracellular transport.," *Nature reviews. Molecular cell biology*, vol. 10, 2009.

[25] E. M. Dagenbach and S. A. Endow, "A new kinesin tree.," *Journal of Cell Science*, vol. 117, 2004.

[26] D. J. Rashid, J. Bononi, B. P. Tripet, R. S. Hodges, and D. W. Pierce, "Monomeric and dimeric states exhibited by the kinesin-related motor protein KIF1A," *Journal of Peptide Research*, vol. 65, 2005.

[27] A. Kashina, G. Rogers, and J. Scholey, "The bimC family of kinesins: essential bipolar mitotic motors driving centrosome separation," *Biochimica et Biophysica Acta (BBA) - Molecular Cell Research*, vol. 1357, 1997.

[28] M. Brunnbauer, F. Mueller-Planitz, S. Kösem, T. H. Ho, R. Dombi, J. C. M. Gebhardt, M. Rief, and Z. Okten, "Regulation of a heterodimeric kinesin-2 through an unprocessive motor domain that is turned processive by its partner.," *Proceedings of the National Academy of Sciences of the United States of America*, vol. 107, 2010.

[29] J. M. Scholey, "Kinesin-2: a family of heterotrimeric and homodimeric motors with diverse intracellular transport functions.," *Annual review of cell and developmental biology*, vol. 29, 2013.

[30] J. Helenius, G. Brouhard, Y. Kalaidzidis, S. Diez, and J. Howard, "The depolymerizing kinesin MCAK uses lattice diffusion to rapidly target microtubule ends.," *Nature*, vol. 441, 2006.

[31] R. B. Case, D. W. Pierce, N. Hom-Booher, C. L. Hart, and R. D. Vale, "The directional preference of kinesin motors is specified by an element outside of the motor catalytic domain," *Cell*, vol. 90, 1997.

[32] M. T. Valentine, P. M. Fordyce, T. C. Krzysiak, S. P. Gilbert, and S. M. Block, "Individual dimers of the mitotic kinesin motor Eg5 step processively and support substantial loads in vitro.," *Nature cell biology*, vol. 8, 2006.

[33] G. Muthukrishnan, Y. Zhang, S. Shastry, and W. O. Hancock, "The Processivity of Kinesin-2 Motors Suggests Diminished Front-Head Gating," *Current Biology*, vol. 19, 2009.

[34] V. Varga, J. Helenius, K. Tanaka, A. A. Hyman, T. U. Tanaka, and J. Howard, "Yeast kinesin-8 depolymerizes microtubules in a length-dependent manner.," *Nature cell biology*, vol. 8, 2006.

[35] R. a. Cross and A. McAinsh, "Prime movers: the mechanochemistry of mitotic kinesins," *Nature Reviews Molecular Cell Biology*, vol. 15, 2014.

[36] E. L. Holzbaur and Y. E. Goldman, "Coordination of molecular motors: from in vitro assays to intracellular dynamics," *Current Opinion in Cell Biology*, vol. 22, 2010.

[37] C. Veigel and C. F. Schmidt, "Moving into the cell: single-molecule studies of molecular motors in complex environments.," *Nature reviews. Molecular cell biology*, vol. 12, 2011.

[38] B. M. Paschal, H. S. Shpetner, and R. B. Vallee, "MAP 1C is a microtubule-activated ATPase which translocates microtubules in vitro and has dynein-like properties," *Journal of Cell Biology*, vol. 105, 1987.

[39] J. Howard, A. J. Hudspeth, and R. D. Vale, "Movement of microtubules by single kinesin molecules," *Nature*, vol. 342, 1989.

[40] W. O. Hancock and J. Howard, "Processivity of the motor protein kinesin requires two heads," *Journal of Cell Biology*, vol. 140, 1998.

[41] R. A. Walker, E. D. Salmon, and S. A. Endow, "The Drosophila claret segregation protein is a minus-end directed motor molecule.," *Nature*, vol. 347, 1990.

[42] W. O. Hancock and J. Howard, "Kinesin's processivity results from mechanical and chemical coordination between the ATP hydrolysis cycles of the two motor domains.," *Proceedings of the National Academy of Sciences of the United States of America*, vol. 96, 1999.

[43] J. Gagliano, M. Walb, B. Blaker, J. C. MacOsko, and G. Holzwarth, "Kinesin velocity increases with the number of motors pulling against viscoelastic drag," *European Biophysics Journal*, vol. 39, 2010.

[44] A. H. Crevenna, S. Madathil, D. N. Cohen, M. Wagenbach, K. Fahmy, and J. Howard, "Secondary structure and compliance of a predicted flexible domain in kinesin-1 necessary for cooperation of motors.," *Biophysical journal*, vol. 95, dec 2008.

[45] G. Arpa á, S. Shastry, W. O. Hancock, and E. Tüzel, "Transport by populations of fast and slow kinesins uncovers novel family-dependent motor characteristics important for in vivo function," *Biophysical Journal*, vol. 107, 2014.

[46] T. Korten and S. Diez, "Setting up roadblocks for kinesin-1: mechanism for the selective speed control of cargo carrying microtubules.," *Lab on a chip*, vol. 8, 2008.

[47] L. Scharrel, R. Ma, R. Schneider, F. Julicher, and S. Diez, "Multimotor transport in a system of active and inactive kinesin-1 motors," *Biophysical Journal*, vol. 107, 2014.

[48] W. J. Walter, I. Machens, F. Rafieian, and S. Diez, "The non-processive rice kinesin-14 OsKCH1 transports actin filaments along microtubules with two distinct velocities," *Nature Plants*, vol. 1, 2015.

[49] J. Hunt, F. Gittes, and J. Howard, "The force exerted by a single kinesin molecule against a viscous load.," *Biophysical journal*, vol. 67, 1994.

[50] C. Leduc, F. Ruhnow, J. Howard, and S. Diez, "Detection of fractional steps in cargo movement by the collective operation of kinesin-1 motors.," *Proceedings of the National Academy of Sciences of the United States of America*, vol. 104, 2007.

[51] N. L. Thompson, T. P. Burghardt, and D. Axelrod, "Measuring surface dynamics of biomolecules by total internal reflection fluorescence with photobleaching recovery or correlation spectroscopy.," *Biophysical journal*, vol. 33, 1981.

[52] A. R. Thompson, G. J. Hoeprich, and C. L. Berger, "Single-molecule motility: Statistical analysis and the effects of track length on quantification of processive motion," *Biophysical Journal*, vol. 104, 2013.

[53] F. Ruhnow, L. Kloss, and S. Diez, "Challenges in estimating the motility parameters of single processive motor proteins," *bioRxiv*, 2017.

[54] A. Yildiz, M. Tomishige, R. D. Vale, and P. R. Selvin, "Kinesin walks hand-over-hand.," *Science (New York, N.Y.)*, vol. 303, 2004.

[55] C. L. Asbury, A. N. Fehr, and S. M. Block, "Kinesin moves by an asymmetric hand-over-hand mechanism.," *Science (New York, N.Y.)*, vol. 302, 2003.

[56] K. Sozański, F. Ruhnow, A. WisÃàniewska, M. Tabaka, S. Diez, and R. Hołyst, "Small Crowders Slow Down Kinesin-1 Stepping by Hindering Motor Domain Diffusion," *Physical Review Letters*, vol. 115, 2015.

[57] R. Schneider, T. Korten, W. J. Walter, and S. Diez, "Kinesin-1 Motors Can Circumvent Permanent Roadblocks by Side-Shifting to Neighboring Protofilaments," *Biophysical Journal*, vol. 108, 2015.

[58] G. J. Hoeprich, A. R. Thompson, D. P. McVicker, W. O. Hancock, and C. L. Berger, "Kinesin's Neck-Linker Determines its Ability to Navigate Obstacles on the Microtubule Surface.," *Biophysical journal*, vol. 106, 2014.

[59] A. Ashkin, J. M. Dziedzic, J. E. Bjorkholm, and S. Chu, "Observation of a single-beam gradient force optical trap for dielectric particles," *Optics Letters*, vol. 11, 1986.

[60] M. Capitanio and F. S. Pavone, "Interrogating biology with force: Single molecule high-resolution measurements with optical tweezers," *Biophysical Journal*, vol. 105, 2013.

[61] J. A. Spudich, S. E. Rice, R. S. Rock, T. J. Purcell, and H. M. Warrick, "Optical traps to study properties of molecular motors," *Cold Spring Harbor Protocols*, vol. 6, 2011.

[62] S. M. Block, L. S. Goldstein, and B. J. Schnapp, "Bead movement by single kinesin molecules studied with optical tweezers.," *Nature*, vol. 348, 1990.

[63] K. Svoboda, C. F. Schmidt, B. J. Schnapp, and S. M. Block, "Direct Observation of Kinesin Stepping by Optical Trapping Interferometry," *NatureNature*, vol. 365, 1993.

[64] C. L. Asbury, "Kinesin: World's tiniest biped," *Current Opinion in Cell Biology*, vol. 17, 2005.

[65] K. Kawaguchi, "Energetics of kinesin-1 stepping mechanism," *FEBS Letters*, vol. 582, 2008.

[66] R. D. Vale, T. Funatsu, D. W. Pierce, L. Romberg, Y. Harada, and T. Yanagida, "Direct observation of single kinesin molecules moving along microtubules.," *Nature*, vol. 380, 1996.

[67] W. Hua, E. C. Young, M. L. Fleming, and J. Gelles, "Coupling of kinesin steps to ATP hydrolysis," *Nature*, vol. 388, 1997.

[68] M. J. Schnitzer and S. M. Block, "Kinesin hydrolyses one ATP per 8-nm step.," *Nature*, vol. 388, 1997.

[69] D. D. Hackney, "Kinesin ATPase: rate-limiting ADP release.," *Proceedings of the National Academy of Sciences of the United States of America*, vol. 85, 1988.

[70] Y. Z. Ma and E. W. Taylor, "Interacting head mechanism of microtubule-kinesin ATPase," *Journal of Biological Chemistry*, vol. 272, 1997.

[71] S. P. Gilbert, M. L. Moyer, and K. A. Johnson, "Alternating site mechanism of the kinesin ATPase," *Biochemistry*, vol. 37, 1998.

[72] S. Rice, A. W. Lin, D. Safer, C. L. Hart, N. Naber, B. O. Carragher, S. M. Cain, E. Pechatnikova, E. M. Wilson-Kubalek, M. Whittaker, E. Pate, R. Cooke, E. W. Taylor, R. A. Milligan, and R. D. Vale, "A structural change in the kinesin motor protein that drives motility.," *Nature*, vol. 402, 1999.

[73] N. R. Guydosh and S. M. Block, "Backsteps induced by nucleotide analogs suggest the front head of kinesin is gated by strain.," *Proceedings of the National Academy of Sciences*, vol. 103, 2006.

[74] S. S. Rosenfeld, J. Xing, G. M. Jefferson, H. C. Cheung, and P. H. King, "Measuring kinesin's first step," *Journal of Biological Chemistry*, vol. 277, 2002.

[75] S. S. Rosenfeld, P. M. Fordyce, G. M. Jefferson, P. H. King, and S. M. Block, "Stepping and stretching. How kinesin uses internal strain to walk processively," *Journal of Biological Chemistry*, vol. 278, 2003.

[76] S. Uemura and S. Ishiwata, "Loading direction regulates the affinity of ADP for kinesin.," *Nature structural biology*, vol. 10, 2003.

[77] K. Svoboda and S. M. Block, "Force and velocity measured for single kinesin molecules," *Cell*, vol. 77, 1994.

[78] E. Meyhöfer and J. Howard, "The force generated by a single kinesin molecule against an elastic load.," *Proceedings of the National Academy of Sciences of the United States of America*, vol. 92, 1995.

[79] N. J. Carter and R. A. Cross, "Mechanics of the kinesin step.," *Nature*, vol. 435, 2005.

[80] B. Milic, J. O. L. Andreasson, W. O. Hancock, and S. M. Block, "Kinesin processivity is gated by phosphate release.," *Proceedings of the National Academy of Sciences of the United States of America*, vol. 111, 2014.

[81] W. O. Hancock, "The Kinesin-1 Chemomechanical Cycle: Stepping Toward a Consensus," *Biophysical Journal*, vol. 110, 2016.

[82] K. Svoboda, P. P. Mitra, and S. M. Block, "Fluctuation analysis of motor protein movement and single enzyme kinetics.," *Proceedings of the National Academy of Sciences of the United States of America*, vol. 91, 1994.

[83] J. O. L. Andreasson, S. Shastry, W. O. Hancock, and S. M. Block, "The mechanochemical cycle of mammalian kinesin-2 KIF3A/B under load," *Current Biology*, vol. 25, 2015.

[84] K. J. Mickolajczyk, N. C. Deffenbaugh, J. Ortega Arroyo, J. Andrecka, P. Kukura, and W. O. Hancock, "Kinetics of nucleotide-dependent structural transitions in the kinesin-1 hydrolysis cycle.," *Proceedings of the National Academy of Sciences of the United States of America*, vol. 112, 2015.

[85] K. J. Mickolajczyk and W. O. Hancock, "Kinesin Processivity Is Determined by a Kinetic Race from a Vulnerable One-Head-Bound State," *Biophysical Journal*, vol. 112, 2017.

[86] R. D. Vale and Y. Y. Toyoshima, "Rotation and translocation of microtubules in vitro induced by dyneins from Tetrahymena cilia.," *Cell*, vol. 52, 1988.

[87] J. Yajima and R. a. Cross, "A torque component in the kinesin-1 power stroke.," *Nature chemical biology*, vol. 1, 2005.

[88] T. Nishizaka, T. Yagi, Y. Tanaka, and S. Ishiwata, "Right-handed rotation of an actin filament in an in vitro motile system.," *Nature*, vol. 361, 1993.

[89] J. Yajima, K. Mizutani, and T. Nishizaka, "A torque component present in mitotic kinesin Eg5 revealed by three-dimensional tracking.," *Nature structural & molecular biology*, vol. 15, 2008.

[90] S. Yamaguchi, K. Saito, M. Sutoh, T. Nishizaka, Y. Y. Toyoshima, and J. Yajima, "Torque generation by axonemal outer-arm dynein," *Biophysical Journal*, vol. 108, 2015.

[91] B. Nitzsche, F. Ruhnow, and S. Diez, "Quantum-dot-assisted characterization of microtubule rotations during cargo transport.," *Nature nanotechnology*, vol. 3, 2008.

[92] V. Bormuth, B. Nitzsche, F. Ruhnow, A. Mitra, M. Storch, B. Rammner, J. Howard, and S. Diez, "The highly processive kinesin-8, Kip3, switches microtubule protofilaments with a bias toward the left," *Biophysical Journal*, vol. 103, 2012.

[93] A. Mitra, F. Ruhnow, B. Nitzsche, and S. Diez, "Impact-Free Measurement of Microtubule Rotations on Kinesin and Cytoplasmic-Dynein Coated Surfaces," *Plos One*, vol. 10, 2015.

[94] S. L. Reck-Peterson, A. Yildiz, A. P. Carter, A. Gennerich, N. Zhang, and R. D. Vale, "Single-molecule analysis of dynein processivity and stepping behavior.," *Cell*, vol. 126, 2006.

[95] V. Varga, C. Leduc, V. Bormuth, S. Diez, and J. Howard, "Kinesin-8 Motors Act Cooperatively to Mediate Length-Dependent Microtubule Depolymerization," *Cell*, vol. 138, 2009.

[96] M. C. Tarhan, Y. Orazov, R. Yokokawa, S. L. Karsten, and H. Fujita, "Biosensing MAPs as "roadblocks": kinesin-based functional analysis of tau protein isoforms and mutants using suspended microtubules (sMTs)," *Lab on a chip*, vol. 13, 2013.

[97] S. Can, M. A. Dewitt, and A. Yildiz, "Bidirectional helical motility of cytoplasmic dynein around microtubules.," *eLife*, 2014.

[98] M. Brunnbauer, R. Dombi, T.-H. Ho, M. Schliwa, M. Rief, and Z. Ökten, "Torque generation of kinesin motors is governed by the stability of the neck domain.," *Molecular cell*, vol. 46, 2012.

[99] J. Kerssemakers, J. Howard, H. Hess, and S. Diez, "The distance that kinesin-1 holds its cargo from the microtubule surface measured by fluorescence interference contrast microscopy.," *Proceedings of the National Academy of Sciences of the United States of America*, vol. 103, 2006.

[100] A. D. Dinsmore, E. R. Weeks, V. Prasad, A. C. Levitt, and D. A. Weitz, "Three-dimensional confocal microscopy of colloids.," *Applied optics*, vol. 40, 2001.

[101] V. Levi, Q. Ruan, and E. Gratton, "3-D Particle Tracking in a Two-Photon Microscope: Application to the Study of Molecular Dynamics in Cells," *Biophysical Journal*, vol. 88, 2005.

[102] J.-H. Spille, T. Kaminski, H.-P. Königshoven, and U. Kubitscheck, "Dynamic three-dimensional tracking of single fluorescent nanoparticles deep inside living tissue.," *Optics express*, vol. 20, 2012.

[103] H. Deschout, F. Cella Zanacchi, M. Mlodzianoski, A. Diaspro, J. Bewersdorf, S. T. Hess, and K. Braeckmans, "Precisely and accurately localizing single emitters in fluorescence microscopy.," *Nature methods*, vol. 11, 2014.

[104] a. P. Wong and J. T. Groves, "Topographical imaging of an intermembrane junction by combined fluorescence interference and energy transfer microscopies.," *Journal of the American Chemical Society*, vol. 123, 2001.

[105] Y. Sun, O. Sato, F. Ruhnow, M. E. Arsenault, M. Ikebe, and Y. E. Goldman, "Single-molecule stepping and structural dynamics of myosin X.," *Nature structural & molecular biology*, vol. 17, 2010.

[106] L. A. Amos and D. Schlieper, "Microtubules and maps," *Advances in Protein Chemistry*, vol. 71, 2005.

[107] R. Dixit, J. L. Ross, Y. E. Goldman, and E. L. F. Holzbaur, "Differential Regulation of Dynein and Kinesin Motor Proteins by Tau," *Science*, vol. 319, 2008.

[108] A. Seitz, H. Kojima, K. Oiwa, E. M. Mandelkow, Y. H. Song, and E. Mandelkow, "Single-molecule investigation of the interference between kinesin, tau and MAP2c," *EMBO Journal*, vol. 21, 2002.

[109] M. Vershinin, B. C. Carter, D. S. Razafsky, S. J. King, and S. P. Gross, "Multiple-motor based transport and its regulation by Tau.," *Proceedings of the National Academy of Sciences of the United States of America*, vol. 104, 2007.

[110] G. J. Hoeprich, K. J. Mickolajczyk, S. R. Nelson, W. O. Hancock, and C. L. Berger, "The axonal transport motor kinesin-2 navigates microtubule obstacles via protofilament switching," *Traffic*, vol. 18, 2017.

[111] I. A. Telley, P. Bieling, and T. Surrey, "Obstacles on the microtubule reduce the processivity of kinesin-1 in a minimal in vitro system and in cell extract," *Biophysical Journal*, vol. 96, 2009.

[112] C. Leduc, K. Padberg-Gehle, V. Varga, D. Helbing, S. Diez, and J. Howard, "Molecular crowding creates traffic jams of kinesin motors on microtubules," *Proceedings of the National Academy of Sciences*, vol. 109, 2012.

[113] A. Seitz and T. Surrey, "Processive movement of single kinesins on crowded microtubules visualized using quantum dots," *The EMBO Journal*, vol. 25, 2006.

[114] K. Dreblow, N. Kalchishkova, and K. J. Böhm, "Kinesin passing permanent blockages along its protofilament track.," *Biochemical and biophysical research communications*, vol. 395, 2010.

[115] I. M.-T. C. Crevel, M. Nyitrai, M. C. Alonso, S. Weiss, M. a. Geeves, and R. a. Cross, "What kinesin does at roadblocks: the coordination mechanism for molecular walking.," *The EMBO journal*, vol. 23, 2004.

[116] A. F. Straight, J. W. Sedat, and A. W. Murray, "Time-lapse microscopy reveals unique roles for kinesins during anaphase in budding yeast," *Journal of Cell Biology*, vol. 143, 1998.

[117] M. M. Wargacki, J. C. Tay, E. G. Muller, C. L. Asbury, and T. N. Davis, "Kip3, the yeast kinesin-8, is required for clustering of kinetochores at metaphase," *Cell Cycle*, vol. 9, 2010.

[118] K. Jaqaman, E. M. King, A. C. Amaro, J. R. Winter, J. F. Dorn, H. L. Elliott, N. Mchedlishvili, S. E. McClelland, I. M. Porter, M. Posch, A. Toso, G. Danuser, A. D. McAinsh, P. Meraldi, and J. R. Swedlow, "Kinetochore alignment within the metaphase plate is regulated by centromere stiffness and microtubule depolymerases," *Journal of Cell Biology*, vol. 188, 2010.

[119] C. Peters, K. Brejc, L. Belmont, A. J. Bodey, Y. Lee, M. Yu, J. Guo, R. Sakowicz, J. Hartman, and C. A. Moores, "Insight into the molecular mechanism of the multitasking kinesin-8 motor.," *The EMBO journal*, vol. 29, 2010.

[120] G. Goshima, R. Wollman, N. Stuurman, J. M. Scholey, and R. D. Vale, "Length control of the metaphase spindle," *Current Biology*, vol. 15, 2005.

[121] J. Stumpff, G. von Dassow, M. Wagenbach, C. Asbury, and L. Wordeman, "The Kinesin-8 Motor Kif18A Suppresses Kinetochore Movements to Control Mitotic Chromosome Alignment," *Developmental Cell*, vol. 14, 2008.

[122] M. I. Mayr, S. Hummer, J. Bormann, T. Gruner, S. Adio, G. Woehlke, and T. U. Mayer, "The Human Kinesin Kif18A Is a Motile Microtubule Depolymerase Essential for Chromosome Congression," *Current Biology*, vol. 17, 2007.

[123] R. R. West, T. Malmstrom, and J. R. McIntosh, "Kinesins klp5(+) and klp6(+) are required for normal chromosome movement in mitosis.," *Journal of cell science*, vol. 115, 2002.

[124] M. A. Garcia, N. Koonrugsa, and T. Toda, "Two kinesin-like Kin I family proteins in fission yeast regulate the establishment of metaphase and the onset of anaphase A," *Current Biology*, vol. 12, 2002.

[125] M. S. Savoian and D. M. Glover, "Drosophila Klp67A binds prophase kinetochores to subsequently regulate congression and spindle length.," *Journal of cell science*, vol. 123, 2010.

[126] Y. Du, C. A. English, and R. Ohi, "The Kinesin-8 Kif18A Dampens Microtubule Plus-End Dynamics," *Current Biology*, vol. 20, 2010.

[127] M. L. Gupta, P. Carvalho, D. M. Roof, and D. Pellman, "Plus end-specific depolymerase activity of Kip3, a kinesin-8 protein, explains its role in positioning the yeast mitotic spindle.," *Nature cell biology*, vol. 8, 2006.

[128] C. Tischer, D. Brunner, and M. Dogterom, "Force- and kinesin-8-dependent effects in the spatial regulation of fission yeast microtubule dynamics.," *Molecular systems biology*, vol. 5, 2009.

[129] S. G. Martin, "Microtubule-dependent cell morphogenesis in the fission yeast," *Trends in Cell Biology*, vol. 19, 2009.

[130] F. Chang and P. Nurse, "How fission yeast fission in the middle," *Cell*, vol. 84, 1996.

[131] P. T. Tran, L. Marsh, V. Doye, S. Inoué, and F. Chang, "A mechanism for nuclear positioning in fission yeast based on microtubule pushing," *Journal of Cell Biology*, vol. 153, 2001.

[132] S. Niwa, K. Nakajima, H. Miki, Y. Minato, D. Wang, and N. Hirokawa, "KIF19A Is a Microtubule-Depolymerizing Kinesin for Ciliary Length Control," *Developmental Cell*, vol. 23, 2012.

[133] M. I. Mayr, M. Storch, J. Howard, and T. U. Mayer, "A non-motor microtubule binding site is essential for the high processivity and mitotic function of kinesin-8 Kif18A," *PLoS ONE*, vol. 6, 2011.

[134] H. Arellano-Santoyo, E. A. Geyer, E. Stokasimov, G.-Y. Chen, X. Su, W. Hancock, L. M. Rice, D. Pellman, F. Bahna, A. Kaczynska, and et Al., "A Tubulin Binding Switch Underlies Kip3/Kinesin-8 Depolymerase Activity," *Developmental Cell*, vol. 42, 2017.

[135] D. Wang, R. Nitta, M. Morikawa, H. Yajima, S. Inoue, H. Shigematsu, M. Kikkawa, and N. Hirokawa, "Motility and microtubule depolymerization mechanisms of the kinesin-8 motor, KIF19A," *eLife*, vol. 5, 2016.

[136] X. Su, W. Qiu, M. L. Gupta, J. B. Pereira-Leal, S. L. Reck-Peterson, and D. Pellman, "Mechanisms Underlying the Dual-Mode Regulation of Microtubule Dynamics by Kip3/Kinesin-8," *Molecular Cell*, vol. 43, 2011.

[137] A. Jannasch, V. Bormuth, M. Storch, J. Howard, and E. Schäffer, "Kinesin-8 is a low-force motor protein with a weakly bound slip state," *Biophysical Journal*, vol. 104, 2013.

[138] M. K. Gardner, M. Zanic, C. Gell, V. Bormuth, and J. Howard, "Depolymerizing kinesins Kip3 and MCAK shape cellular microtubule architecture by differential control of catastrophe," *Cell*, vol. 147, 2011.

[139] G. J. Brouhard, J. H. Stear, T. L. Noetzel, J. Al-Bassam, K. Kinoshita, S. C. Harrison, J. Howard, and A. A. Hyman, "XMAP215 Is a Processive Microtubule Polymerase," *Cell*, vol. 132, 2008.

[140] Y. Chen, M. M. Rolls, and W. O. Hancock, "An EB1-kinesin complex is sufficient to steer microtubule growth in vitro," *Current Biology*, vol. 24, 2014.

[141] L. Reese, A. Melbinger, and E. Frey, "Crowding of molecular motors determines microtubule depolymerization," *Biophysical Journal*, vol. 101, 2011.

[142] A. Melbinger, L. Reese, and E. Frey, "Microtubule length regulation by molecular motors," *Physical Review Letters*, vol. 108, 2012.

[143] B. Nitzsche, E. Dudek, L. Hajdo, A. A. Kasprzak, A. Vilfan, and S. Diez, "Working stroke of the kinesin-14, ncd, comprises two substeps of different direction," *Proceedings of the National Academy of Sciences*, vol. 113, 2016.

[144] P. Meurer-Grob, J. Kasparian, and R. H. Wade, "Microtubule structure at improved resolution," *Biochemistry*, vol. 40, 2001.

[145] F. Ruhnow, D. Zwicker, and S. Diez, "Tracking single particles and elongated filaments with nanometer precision.," *Biophysical journal*, vol. 100, 2011.

[146] S. C. B. Gopinath, K. Awazu, M. Fujimaki, K. Shimizu, W. Mizutani, and K. Tsukagoshi, "Surface functionalization chemistries on highly sensitive silica-based sensor chips," *The Analyst*, vol. 137, 2012.

[147] P. Bieling, I. A. Telley, J. Piehler, and T. Surrey, "Processive kinesins require loose mechanical coupling for efficient collective motility," *EMBO reports*, vol. 9, 2008.

[148] Y. Sun, J. D. McKenna, J. M. Murray, E. M. Ostap, and Y. E. Goldman, "Parallax: high accuracy three-dimensional single molecule tracking using split images.," *Nano letters*, vol. 9, 2009.

[149] R. Schneider, T. Glaser, M. Berndt, and S. Diez, "Using a quartz paraboloid for versatile wide-field TIR microscopy with sub-nanometer localization accuracy," *Optics Express*, vol. 21, 2013.

[150] T. Kobayashi, N. Morone, T. Kashiyama, H. Oyamada, N. Kurebayashi, and T. Murayama, "Engineering a novel multifunctional green fluorescent protein tag for a wide variety of protein research," *PLoS ONE*, vol. 3, 2008.

[151] I. H. Barrette-Ng, S. C. Wu, W. M. Tjia, S. L. Wong, and K. K. S. Ng, "The structure of the SBP-Tag-streptavidin complex reveals a novel helical scaffold bridging binding pockets on separate subunits," *Acta Crystallographica Section D: Biological Crystallography*, vol. 69, 2013.

[152] A. D. Keefe, D. S. Wilson, B. Seelig, and J. W. Szostak, "One-Step Purification of Recombinant Proteins Using a Nanomolar-Affinity Streptavidin-Binding Peptide, the SBP-Tag," *Protein Expression and Purification*, vol. 23, 2001.

[153] T. L. Hawkins, D. Sept, B. Mogessie, A. Straube, and J. L. Ross, "Mechanical properties of doubly stabilized microtubule filaments," *Biophysical Journal*, vol. 104, 2013.

[154] M. Tokunaga, N. Imamoto, and K. Sakata-Sogawa, "Highly inclined thin illumination enables clear single-molecule imaging in cells.," *Nature methods*, vol. 5, 2008.

[155] M. Bugiel, E. Böhl, and E. Schäffer, "The Kinesin-8 Kip3 Switches Protofilaments in a Sideward Random Walk Asymmetrically Biased by Force," *Biophysical Journal*, vol. 108, 2015.

[156] M. Kikkawa and N. Hirokawa, "High-resolution cryo-EM maps show the nucleotide binding pocket of KIF1A in open and closed conformations.," *The EMBO journal*, vol. 25, 2006.

[157] F. Kozielski, S. Sack, A. Marx, M. Thormählen, E. Schönbrunn, V. Biou, A. Thompson, E. M. Mandelkow, and E. Mandelkow, "The crystal structure of dimeric kinesin and implications for microtubule-dependent motility," *Cell*, vol. 91, 1997.

[158] A. Yildiz, M. Tomishige, A. Gennerich, and R. D. Vale, "Intramolecular Strain Coordinates Kinesin Stepping Behavior along Microtubules," *Cell*, vol. 134, 2008.

[159] S. Rice, A. W. Lin, D. Safer, C. L. Hart, N. Naber, B. O. Carragher, S. M. Cain, E. Pechatnikova, E. M. Wilson-Kubalek, M. Whittaker, E. Pate, R. Cooke, E. W. Taylor, R. A. Milligan, and R. D. Vale, "A structural change in the kinesin motor protein that drives motility.," *Nature*, vol. 402, 1999.

[160] R. Zhang, G. M. Alushin, A. Brown, and E. Nogales, "Mechanistic origin of microtubule dynamic instability and its modulation by EB proteins," *Cell*, vol. 162, 2015.

[161] A. B. Asenjo and H. Sosa, "A mobile kinesin-head intermediate during the ATP-waiting state.," *Proceedings of the National Academy of Sciences of the United States of America*, vol. 106, 2009.

[162] T. Mori, R. D. Vale, and M. Tomishige, "How kinesin waits between steps.," *Nature*, vol. 450, 2007.

[163] E. Toprak, A. Yildiz, M. T. Hoffman, S. S. Rosenfeld, and P. R. Selvin, "Why kinesin is so processive.," *Proceedings of the National Academy of Sciences of the United States of America*, vol. 106, 2009.

[164] S. Verbrugge, Z. Lansky, and E. J. G. Peterman, "Kinesin's step dissected with single-motor FRET.," *Proceedings of the National Academy of Sciences of the United States of America*, vol. 106, 2009.

[165] V. Bormuth, V. Varga, J. Howard, and E. Schäffer, "Protein friction limits diffusive and directed movements of kinesin motors on microtubules.," *Science (New York, N.Y.)*, vol. 325, 2009.

[166] J. M. Muretta, Y. Jun, S. P. Gross, J. Major, D. D. Thomas, and S. S. Rosenfeld, "The structural kinetics of switch-1 and the neck linker explain the functions of kinesin-1 and Eg5," *Proceedings of the National Academy of Sciences*, vol. 112, 2015.

[167] G. Y. Chen, K. J. Mickolajczyk, and W. O. Hancock, "The kinesin-5 chemomechanical cycle is dominated by a two-heads-bound state," *Journal of Biological Chemistry*, vol. 291, 2016.

[168] Y. Taniguchi, M. Nishiyama, Y. Ishii, and T. Yanagida, "Entropy rectifies the Brownian steps of kinesin," *Nature Chemical Biology*, vol. 1, 2005.

[169] S. M. Block, "Kinesin motor mechanics: binding, stepping, tracking, gating, and limping.," *Biophysical journal*, vol. 92, 2007.

[170] S. Shastry and W. O. Hancock, "Neck Linker Length Determines the Degree of Processivity in Kinesin-1 and Kinesin-2 Motors," *Current Biology*, vol. 20, 2010.

[171] S. Shastry and W. O. Hancock, "Interhead tension determines processivity across diverse N-terminal kinesins," *Proceedings of the National Academy of Sciences*, vol. 108, 2011.

[172] X. Pan, S. Acar, and J. M. Scholey, "Torque generation by one of the motor subunits of heterotrimeric kinesin-2," *Biochemical and Biophysical Research Communications*, vol. 401, 2010.

[173] V. Hariharan and W. O. Hancock, "Insights into the mechanical properties of the kinesin neck linker domain from sequence analysis and molecular dynamics simulations," *Cellular and Molecular Bioengineering*, vol. 2, 2009.

[174] J. E. Walker, M. Saraste, M. Runswick, and N. J. Gay, "Distantly related sequences in the alpha- and beta-subunits of ATP synthase, myosin, kinases and other ATP-requiring enzymes and a common nucleotide binding fold.," *The EMBO Journal*, vol. 1, 1982.

[175] Z. Bertalan, Z. Budrikis, C. A. M. La Porta, S. Zapperi, and W. X. Yang, "Navigation strategies of motor proteins on decorated tracks," *PLoS ONE*, vol. 10, 2015.

[176] Y. Shin, Y. Du, S. E. Collier, M. D. Ohi, M. J. Lang, and R. Ohi, "Biased Brownian motion as a mechanism to facilitate nanometer-scale exploration of the microtubule plus end by a kinesin-8," *Proceedings of the National Academy of Sciences*, vol. 112, 2015.

[177] H. Isojima, R. Iino, Y. Niitani, H. Noji, and M. Tomishige, "Direct observation of intermediate states during the stepping motion of kinesin-1," *Nature Chemical Biology*, vol. 12, 2016.

[178] M. Castoldi and A. V. Popov, "Purification of brain tubulin through two cycles of polymerization-depolymerization in a high-molarity buffer.," *Protein expression and purification*, vol. 32, 2003.

[179] T. Korten, S. Chaudhuri, E. Tavkin, M. Braun, and S. Diez, "Kinesin-1 Expressed in Insect Cells Improves Microtubule in Vitro Gliding Performance, Long-Term Stability and Guiding Efficiency in Nanostructures," *IEEE Transactions on Nanobioscience*, vol. 15, 2016.

[180] T. Korten, B. Nitzsche, C. Gell, F. Ruhnow, C. Leduc, and S. Diez, "Fluorescence imaging of single Kinesin motors on immobilized microtubules.," *Methods in molecular biology (Clifton, N.J.)*, vol. 783, 2011.

[181] B. Nitzsche, V. Bormuth, C. Bräuer, J. Howard, L. Ionov, J. Kerssemakers, T. Korten, C. Leduc, F. Ruhnow, and S. Diez, "Studying kinesin motors by optical 3D-nanometry in gliding motility assays.," *Methods in cell biology*, vol. 95, 2010.

[182] S. Gilles, M. Meier, M. Prömpers, A. van der Hart, C. Kügeler, A. Offenhäusser, and D. Mayer, "UV nanoimprint lithography with rigid polymer molds," *Microelectronic Engineering*, vol. 86, 2009.

[183] G. P. McCabe and D. S. Moore, "Introduction to the Practice of Statistics.," vol. 5, 2006.

[184] W. H. Press, S. a. Teukolsky, W. T. Vetterling, and B. P. Flannery, "Numerical recipes in C (2nd ed.): the art of scientific computing," vol. 29, 1992.

List of acronyms

1HB	one head-bound
1D	one dimensional
2HB	two head-bound
3D	three dimensional
aa	amino acid
ADP	adenosine-5'-diphosphate
AMP-PNP	adenosin-5'[β,γ-imido]-triphosphate
ATP	adenosine-5'-triphosphate
BRB	brinkley reassembly buffer
CCD	charge-coupled device
DDS	dimethyldichlorosilane
DNA	deoxyribonucleic acid
DTT	dithiothreitol
EDTA	ethylene diamine tetraacetic acid
eGFP	enhanced green fluorescent protein
EGTA	ethylene glycol tetraacetic acid
EMCCD	electron multiplying charge-coupled device
FIESTA	fluorescence imaging evaluation software for tracking and analysis
FLIC	fluorescence interference contrast
fps	frames per second
GDP	guanosine-5'-diphosphate
GFP	green fluorescent protein
GMP-CPP	guanosine-5'[α,β]-triphosphate
HCl	hydrochloric acid
HILO	highly inclined thin illumination
His	histadine

KCL	potassium chloride
KOH	potassium hydroxide
KPi	potassium phosphate
MAP	microtubule associated protein
mfGFP	multi-functional green fluorescent protein
$MgCl_2$	magnesium chloride
MT	microtubule
MTOC	microtubule organizing center
NaCl	sodium chloride
Ni-NTA	nickel immobilized in nitrilotriacetic acid
PBS	phosphate buffered saline
PCR	polymerase chain reaction
PFPE	perfluorpolyether
PGMEA	propylene glycol monomethyl ether acetate
P_i	inorganic phosphate
PMSF	phenylmethanesulfonyl fluoride
PSD	power spectral density
PSF	point spread function
QDot	quantum dot
RB	roadblock
SBP	streptavidin binding peptide
S.D.	standard deviation
SF+	Spoodoptera fugiperda
S-MT	speckled microtubule
SNR	signal to noise ratio
TIRF	total internal reflection fluorescence
UV-NIL	ultraviolet nanoimprint lithography
YFP	yellow fluorescent protein

Publications related to this work

Parts of this work were used in the following publications:

- Volker Bormuth, Bert Nitzsche, Felix Ruhnow, **Aniruddha Mitra**, Marko Storch, Burkhard Rammner, Jonathon Howard and Stefan Diez (2012). *≪The highly Processive kinesin-8, Kip3, switches microtubule protofilaments with a bias toward the left≫*. In: Biophysical Journal 103.

- **Aniruddha Mitra**, Felix Ruhnow, Bert Nitzsche and Stefan Diez (2015). *≪Impact-free measurement of microtubule rotations on kinesin and cytoplasmic-dynein coated surfaces≫*. In: PLoS One 10.

- **Aniruddha Mitra**, Felix Ruhnow, Salvatore Girardo and Stefan Diez (2017). *≪Directional sidestepping of Kip3/kinesin-8 is regulated by ATP waiting time and motor-microtubule interaction strength≫*. In preparation.

Acknowledgements

The duration of my life at the Diezlab has been made memorable by numerous people. It has been a rather long ride (longer than I care to admit) and this is my opportunity to thank the wonderful people who have made it a sublime experience.

First, I wholeheartedly thank *Stefan Diez* for granting me the opportunity to work in his lab. Coming in the lab with near-zero experimental research experience, Stefan has mentored me to develop into an enthuisiastic scientist. His analytical approach and innovative ideas for scientific problems has elevated my joy for science. His ethical approach towards doing science is something I would like to incorporate in my future scientific (or non-scientific) career. He is also an engaging person, teaming with good spirit that translates wonderfully to the other lab members, making the Diezlab an awesome place to be.

Second, I am grateful to the two people who supervised me over the years, *Felix Ruhnow and Bert Nitzsche*. Felix has been my true partner in crime. We have been involved in numerous projects, be it obsessing over Kip3, cricket vs baseball discussions, notorious photoshopping vendettas or drowning in obscure rivers in eastern Europe. His true genius as an image analyst has made this work possible. Bert supervised me during the intial years of my PhD. With immense patience and enthusiasm, he got me started with most of my projects.

Third, I am grateful to the numerous people who have assisted me with my work along the way. I thank *Michael Schlierf*, *Stefan Diez*, *Felix Ruhnow* and *Bert Nitzsche* for being part of my eTAC committee, which provided me clarity with my project. I thank *Felix Ruhnow*, *Salvatore Girardo*, *Friedrich Schwarz*, *Wilhelm Walter* and *Rene Schneider* for facilitating this project (see acknowledgement section at the end of every results chapter). I thank the protein purification facility of MPI-CBG (specifically *Regis Lemaitre*), *Marko Storch* and *Marcus Braun* for helping me create, express and purify proteins. I thank *Roman Renger* and *Nicole Osang* for believing in the projects I got them involved in for their master theses.

I thank *Rahul Grover aka Gloverpedia*, *Viekko Geyer*, *Jens Ehrig*, *Felix Ruhnow*, *Corina Bräuer* and *Akansha Jain* for commenting and proofreading the manuscript of the thesis. I extend a wholehearted thanks to *Barbara Lindemann* for taking care of the bureaucratic part of academia. Also I am eternally grateful to the nicest soul, *Corina Bräuer*, for making life in the lab easy-breezy.

Fourth, I thank the people (in no particular order) who provided the 'masala' in the lab. My Czech family, *Zdenek aka 'Mard'*, *Eva Maria* and *'Gunda' Tonda*, for providing me a feeling of home (partly because they briefly lived as refugees in my home). *Rahul Grover* for being my devoted follower. *Lara*, *Juliane* and *Samata* for accepting me as one of the girls. *Annemarie* for answering all the questions in my life. *Jens* for keeping the lab socially vibrant. *Felix* for being a constant. *Till* for all the geeky conversations. *Bert* for the joyous beer hour ruminations. *Roman* for conveniently replacing *'Ohmann'*. *Marcus* for being a philosophical recluse. *Corina* for always being there with a smile. And there are a few others as well... *Cordula*, *Rucola*, *Martina*, *Marta*, *Agatha*, *Victor*, *Jochen*, *Rene*, *Verena*...

Fifth, I thank all my friends outside of work for providing me some (in)sanity whenever necessary. Firstly, I thank all my friends from Rugby Cricket Dresden, specially the Saxon Warriors, for all the competitive cricket, drunken night outs, moments of frustrations and delirious moments of joy. I thank all my subcontinental friends (specifically *Rahul A* and *Uddi*) for taking care of me over the years. I also thank my crazy Latin friends, my relentless Greeks and all other friends for all the wonderful moments.

Finally, I thank my family, who have been following all my moves from far far away. I thank my sister *Arundhati Mitra* and brother-in-law *Akshay Lunkad* for being a constant source of support and confidence, my mother *Kaberi Mitra* for being my greatest well-wisher and friend, and my father *Abhijit Mitra* for always being an inspiration and taking great pride in even my smallest acheivements.